6-20-2022

Exploring Structure-Function Relationship in Small-Molecular Catalysts Using Computational and Experimental Methodologies

Avik Bhattacharjee
Portland State University

Exploring Structure-Function Relationship in Small-Molecular Catalysts Using Computational and Experimental Methodologies

by

Avik Bhattacharjee

A dissertation submitted in partial fulfillment of the
requirements for the degree of

Doctor of Philosophy
in
Chemistry

Dissertation Committee:
Theresa M. McCormick, Chair
Andrea M. Goforth
Jack Barbera
Raúl Bayoán Cal

Portland State University
2022

ABSTRACT

Molecular modeling is a useful tool in the field of catalyst design for various processes. The use of Density Functional Theory (DFT) is routine in almost every discipline of chemistry. This allows for a deeper understanding of a molecular system even in situations where implementation of an experimental technique is unfeasible. However, without the right choice of theory and insufficient description, the model becomes susceptible to produce ambiguous results. This often leads to poor correlation with experimental findings hence an incomplete understanding of the system under study. Hence, to acquire a thorough knowledge of the intricacies involved in a system, a judicious survey of the molecular model is necessary.

Explored herein are embodiments of four catalytic systems, combining computational and experimental techniques, to better understand the structure-function relationship. The systems of choice include twelve homoleptic, and two heteroleptic Ni(II) tris-pyridinethiolate water splitting catalysts, an organo-photocatalyst for aerobic oxidation of benzylic alcohols, and finally a series of eighteen diarylhalonium salts and diarylchalcogenides.

The first chapter describes a detailed study on homoleptic water splitting catalysis that demonstrates the impact of intramolecular hydrogen bonding (H-bonding) on the pK_a of octahedral tris-(pyridinethiolato)nickel (II), **[Ni(PyS)$_3$]$^-$**, commonly referred to as Ni(II) tris-pyridinethiolate. Protonation is a key step in catalytic proton reduction to produce hydrogen gas, and thus optimizing the catalyst's pK_a is critical for catalyst design. DFT

calculations on a **[Ni(PyS)$_3$]$^-$** catalyst, and eleven derivatives, demonstrate geometric isomer formation in the protonation step of the catalytic cycle. Through Quantum Theory of Atoms in Molecules (QTAIM), we show that the pK_a of each isomer is driven by intramolecular H-bonding of the proton on the pyridyl N to a S on a neighboring thiopyridyl (PyS$^-$) ligand. Experimental measurements used to determine the pK_a and reduction potential (E^0) of the catalysts support the formation of the geometric isomers upon protonation, although the isomers complicate understanding the experimental results. This work demonstrates that ligand modification *via* the placement of electron-donating (D) or electron-withdrawing (W) groups may have unexpected effects on the catalyst's pK_a due to intramolecular H bonding. This work suggests the possibility that modification of substituent placement on the ligands to manipulate H bonding in homogeneous metal catalysts could be explored as a tool to simultaneously target both desired pK_a and E^0 values in small molecular catalysts.

In the subsequent chapter a strategy to fine-tune the efficiency of a water splitting **[Ni(PyS)$_3$]$^-$** catalyst through heteroleptic ligand design was explored using a computational investigation of the complete catalytic mechanism. DFT calculations supported by topology analyses using QTAIM, show introduction of electron donating (D) -CH_3 and electron withdrawing (W) -CF_3 groups on the PyS$^-$ ligands of the same complex can tune the pK_a and E^0, simultaneously. Computational modeling of two heteroleptic nickel(II) tris-pyridinethiolate complexes with 2:1 and 1:2 ED and EW -CH_3 and -CF_3 group containing PyS$^-$ ligands, respectively, suggests that the ideal combination of EW to ED groups is 2:1. This work also outlines the possibility of formation of a large number of isomers after the

protonation of one of the pyridyl N atoms as observed in the homoleptic catalysis, and suggests that it is important to carefully account for all possible geometric isomers in order to obtain unambiguous computational results. This work provides a roadmap for synthetic chemists to achieve a better water splitting catalyst that could work in elevated pH media with lower overpotential.

The next chapter describes a novel reaction pathway to photochemically oxidize a benzylic alcohol using an organocatalyst, *N*-hydroxyphthalimide (NHPI), and allows for the simultaneous access to hydrogen peroxide (H_2O_2) as a value-added byproduct under metal-free conditions. Photocatalytic oxidation of alcohols using oxygen often proceeds through excitation of oxygen from its triplet ground state to the singlet excited state where, singlet oxygen ($^1O_2$) is produced by using a photosensitizer to excite oxygen. Through computational and experimental investigation of the process, we have evaluated that the process utilizes $^1O_2$ as the oxidant, that converts NHPI to the active radical intermediate phthalimide-*N*-oxyl (PINO). PINO initiates the oxidation on the organic motif by the abstraction of a H atom. Understanding the process in greater detail using computational methodologies will allow for the design of more efficient photocatalysts that are capable of carrying out more complicated aerobic oxidations using greener methods which is of immense interest for both laboratory and industrial scale reactions.

Finally, a series of diarylhalonium salts and isoelectronic diarylchalcogenides were studied. This chapter entails the deviation of the structural parameters of these compounds from the well-accepted three center-four electron (*3c-4e*) bonding model. The existing *3c-4e* model describes the bonding in λ^3-iodanes accurately, however, fails to account for any

structural deviation based on the periodic trends for hypervalent halogens and chalcogens. To provide a better understanding of the bonding and properties such as halogen bonding, and Lewis acidity, a major restructuring of the existing bonding theory was required. That was achieved by the inclusion of computed *s*- /*p*- orbital mixing on the molecular orbitals directed toward the incoming substituents, based on qualitative Bent's rule. The introduction of orbital mixing along with the electronegativity of the substituents in the revised bonding could account for both experimentally observed thermodynamic and kinetic reactivity of a series of halonium salts.

This work entails the exploration of different chemical systems that utilizes appropriate molecular model using computational methodologies. The calculated results were compared with the experimental investigations and a good correlation was observed. The molecular models described herein can be extrapolated to structurally allied systems to gain a better understanding of the underlying structure-function relationships.

DEDICATION

This work is dedicated to Dahlia and Idris.

ACKNOWLEDGEMENTS

First and foremost, I would like to express my gratitude to my advisor, and committee chair, Dr. Theresa McCormick. I could not have done this without her constant guidance, support, and encouragement. I would like to thank the members of my dissertation committee, Dr. Andrea Goforth, Dr. Jack Barbera, Dr. Raúl Bayoán Cal, and Dr. Shankar Rananavare for their feedback and insights throughout the development of this work. I would like to acknowledge my collaborators, Prof. Eric Rivard, Dr. Sanela Martic, Dr. Kodiah Beyeh, Dr. Shawn Burdette, and Dr. David Stuart for the opportunities to be able to learn from them. I also appreciate the support form Dr. Eric Sheagley, and Dr. Shuvashree Ray.

Thanks to Patrick for the brotherly love, guidance, and a home, and thanks to Julian for making it a family. I could not express how fortunate I am to have him as a friend.

I could not have moved forward without the love and warmth I have received from all the present and past members of the McCormick group. Special thanks to Day, and Ki (and Enzo) for always being there for me. Thanks to Dr. Virca for leaving a strong scientific foundation behind on which most of this work is built on, Dr. Lutkus, Dr. Rettig for all the constructive criticism and stimulating discussions. I have been really fortunate to work with the most amazing and motivated undergraduates and high school student during my time here. A lot of the credit for this goes to Oreana Galue, Trent Ethridge, and Serena Frazee.

Finally, I would like to thank my parents who, halfway across the world, have always found ways to show love and support during my journey through chemistry.

TABLE OF CONTENTS

LIST OF TABLES

LIST OF FIGURES

LIST OF ABBREVIATIONS & SYMBOLS

AO	Atomic orbitals
a.u.	Atomic unit
C	Chemical
c	Center
cal	Calories
D	Electron donating group
DFT	Density Functional Theory
ε	Molar absorptivity
E	Electrochemical
E	Chalcogens
E^0	Reduction potential at standard conditions
EDG	Electron donating group
EWG	Electron withdrawing group
F	Faraday's constant
G	Gibbs Energy or, Free Energy
g	grams
H	Hydrogen
H	Hamiltonian
h	Hybrid Orbital
Ha	Hartrees
IPCC	International Panel for Climate Change

K	Kelvin
k	Kilo
K_a	Acid dissociation constant
λ_{max}	Wavelength at which the maximum absorption of a compound occurs
L	Liters
LGO	Ligand group orbital
m	milli
Mes	Mesityl
MO	Molecular orbital
N	Nitrogen
n	Non-bonding Orbital
n	Number of moles
NBO	Natural Bond Orbital
NHPI	*N*-hydroxyphthalimide
Ni	Nickel
ρ	Electron density
PCET	Proton Coupled Electron Transfer
Ph	Phenyl
PINO	Phthalimide-*N*-Oxyl
PyS^-	Pyridinethiolate
QTAIM	Quantum Theory of Atoms in Molecules

R	Universal Gas Constant
σ	Bonding Orbital
σ*	Anti-bonding orbital
S	Sulfur
SCE	Saturated Calomel Electrode
sq. py.	Square pyramid
T	Temperature
t	Time
$t_b p$	Trigonal bipyramid
V	Volts
W	Electron Withdrawing group
X	Halogens

LIST OF SCHEMES

Chapter 1 Introduction

1.1 Structure Function Relationship

The structure-activity (function) relationship (SAR) is the interrelation between the chemical structure of a molecule and its chemical and physical property.[1–3] The term first was derived, in its original form, in a report published by Crum-Brown and Fraser in 1865.[4] However, the central idea of the one-to-one correspondence between the chemical structure and the reactivity of a molecular system was first proposed by A. F. A. Cros. In 1863 a report titled as "Action de l'alcool amylique sur l'organisme" was published by Cros which describes the interdependence of toxicity of primary aliphatic alcohols and their water solubility.[5]

This idea was popularized among the medical practitioners at the time and was accepted with the central axiom that *activity of molecules is reflected in their structure, hence similar molecules have similar activity*.[4] The premise of drug-discovery and drug-delivery research heavily relies on this principle, as the interactions of small molecular systems and large macromolecules can be quantitatively understood under the description of this simple principle. Even though, the principle was solely developed for, and by the activity of biologically important molecular motifs, this was adopted by molecular chemists in the mid-twentieth century. The similarities in chemical reactivity of structurally allied small-molecular systems opened the door for (Quantitative) Structure Activity Relationship (QSAR) in small molecules.[2]

Structure activity relationship was primarily investigated, exclusively, through the experimental methodologies. However, introduction of the concept of theoretical molecular modeling, along with the experimental techniques, to determine the interconnection between the structure and the chemical activity of a molecular system gained immediate success. The interdisciplinary research combining both experimental and theoretical techniques in the exploration of SAR divulged into a better understanding of the underlying chemical processes.[5] This can be attributed to the development of sophisticated mathematical models, and statistical correlations that relate the molecular structure at the quantum domain with its material properties, since Schrödinger's wave equation.[6] This work entails the exploration of four small-molecular/catalytic systems using experimental and computational methodologies to gain a detailed understanding of the structure-function relationship with two broad objectives: 1) design a more efficient catalyst; 2) develop a better theoretical model to describe the structural features that can better describe the experimentally observed thermodynamic properties.

1.2 Molecular Modeling and Computational Chemistry

The quantum mechanical and wave-mechanical description of electronic orbit (orbitals) pioneered by Bohr and Sommerfeld at the wake of twentieth century revealed the laws that govern the microscopic world.[7] These discoveries changed the perception of Dalton's atomic theory and helped draw a line between the classical and quantum domain. However, the *Correspondence Principle* helped bridge the two domains by the simplistic description of the material world as a *limit of large quantum numbers*. In an independent effort, Schrödinger developed a generalized mathematical model that further validates

Bohr's *Correspondence Principle* by simply expressing an atomic system using a set of mathematical functions of the coordinates of electronic positions. These functions are called *wavefunctions* and hold on to all the information about the system which can be extracted when treated with mathematical operators corresponding to the physical observables of interest. In short, it takes the form of an *eigen-value* equation given as:

$$\hat{H}\,\Psi = E\,\Psi \tag{1.1}$$

When the total energy operator, or atomic Hamiltonian (H) is applied to the atomic wavefunction (Ψ), the wavefunction is regenerated along with the total energy value (E) of the atom. This description simultaneously simplified and complicated the understanding of the atomic model. The definition of an atomic system was contingent upon the description of its Hamiltonian and the wavefunction, which significantly lowered the parametric dependence proposed in other theories. But solution of the interactive potential energy terms in the Hamiltonian is impossible due to the physical and mathematical limitations.

This introduced the importance of molecular modeling with the objective to describe: 1) a Hamiltonian (H_M) that closely resembles to the true atomic Hamiltonian (H_T) where the interaction terms can be analytically solved; 2) a wavefunction (Φ) that takes up the form of the true wavefunction (Ψ). However, the search for better H_M and Φ involves rigorous iterative methods in order to derive a structure that has the attributes of a true structure and cannot be done manually. To achieve that several models have been developed over the years, that can harness the power of computers to numerically solve the related wave equation for a molecular system. This method assumes that better the

description of the molecular model better is the structure hence associated molecular property. One of the most descriptive, and widely accepted techniques of computational molecular modeling is called the Density Functional Theory (DFT) developed by Walter Kohn, Pierre Hohenberg, Lu Jeu Sham, John Pople, and others in the mid-1960s. In this work, we have used DFT as a tool to describe the structures of the molecular systems studied to better understand the associated reactivity.[8] The DFT results were analyzed using the Quantum Theory of Atoms in Molecules (QTAIM) technique to investigate the short-range hydrogen bonding (H-bonding) interactions, and Natural Bond Orbital (NBO) method to better understand the contributions from the atomic orbital (AO) toward the bonding interactions as seen in different molecules and will be discussed in the subsequent sections.

1.2.1 Density Functional Theory (DFT).

Density Functional Theory is a quantum-mechanical atomistic simulation technique that belongs to the family of first principle (*ab initio*) methods to compute a wide variety of molecular properties.[8–10] This method is widely applied in organic, inorganic chemistry, condensed matter physics, and materials science research, to name a few. DFT has a strong predictive power and can handle essentially any element in the periodic table without the manual addition of experimentally obtained input parameters because it relies on the assumption that the properties of a molecular system can be expressed as a function of distribution of electron density. Furthermore, DFT calculations help the understanding of the behavior of different molecular systems under different conditions.

DFT relies on the computation of the total electron density of the molecular system and hence does not require the explicit calculation of the wavefunction.[11] It uses a pseudo-wavefunction to compute a part of the energy and the rest can be calculated from the electron density. Under the framework of DFT, the normalized wavefunction (Ψ) and the total electron density (ρ) are interrelated by the following equation, where *N* is the total number of electrons:

$$\rho = \frac{|\Psi^2|}{N} \tag{1.2}$$

The simplicity of the theory and very high accuracy in the predictive power of modern DFT methods, with low computational cost, has led the steady increase in its widespread use compared to the other electronic structure methods, such as Hartree-Fock (HF), Møller-Plesset perturbation theory (MP) and configuration interaction (CI) *etc.*

1.2.2 Quantum Theory of Atoms in Molecules (QTAIM).

Quantum Theory of Atoms in Molecules, or simply Atoms in Molecules (AIM) is a model of electronic systems that describes interactions (such as, bonding) solely based on the electronic densities of atoms in a molecule.[12] It was mainly developed by Richard Bader culminating the theoretical and experimentally measured electron densities in the crystal structure. Under this description, a single molecule is expressed as an isolated system consisting of atoms. The atoms can interact among each other by the electron density, while the molecular interactions are thought to be a transfer of momentum. The 'bonds' are replaced by the concept of so-called 'path', as the trajectory in which the

electron densities are shared between the atoms. In this model, a bonding interaction is characterized by the deposition of electron density while a non-bonding interaction is simply the depletion of the electron density on the topological space.

The remarkable success of this model in understanding experimentally observed short-range interactions in organic crystals has led to its wider application. Currently, this model is used to investigate the non-classical intermolecular and intramolecular interactions, namely hydrogen bonding, agostic interaction *etc.*

1.2.3 Natural Bond Orbital (NBO).

Natural Bond Orbital is described as a theoretical bonding orbital with the maximized electron density. This method is useful to calculate the distribution of electron density in atoms and within the bonding interactions in between atoms to form a molecule. This method quantitatively describes the *amount* of atomic orbital contribution while formation of a molecular orbital. This concept was first introduced by Löwdin in 1955 and refined by Weinhold and co-workers.[13–15]

This method is used to better describe the electron density distribution in compounds with high ionic character, usually containing a metal or a charged central atom. Theoretically, the bonding NBOs (σ_{AB}) ,and antibonding NBOs (σ_{AB}*) between two centers A and B can be generated by the linear combinations of the hybrid orbitals donated by A (h_A), and B (h_B) using the following equations, respectively:

$$\sigma_{AB} = c_A h_A + c_B h_B \tag{1.3}$$

$$\sigma_{AB}^{*} = c_A h_A - c_B h_B \quad (1.4)$$

The c_A and c_B are described as the *polarization coefficients* and satisfy the normalization condition, given by the following equation:

$$c_A^2 + c_B^2 = 1 \quad (1.5)$$

Natural Bond Orbital calculation's treatment of the molecular orbitals are found to generate satisfactory description of atomic orbital contribution to the bonding including and beyond Lewis's framework of covalent and ionic bonding. The modest computational cost of this electron density-based calculation makes it an impressive tool to better understand the structural features of molecules containing atoms with filled octet as well as, hypervalent atoms.

1.3 Improvement of Molecular Models and Exploration of SAR

The use of the powerful computational tools, described in the previous section, has shown great success in understanding the structure-activity relationship observed in the small molecular systems.[3] The geometry optimization using the analysis of the electron density, performed by the DFT technique allows for a better description of the molecular structure. The other molecular modeling tools, such as normal mode analysis, and QTAIM, and NBO analysis enables the understanding of the molecular properties based on the electron density distribution revealed by the DFT calculations.[6,8,16]

Solution of the statistical mechanical relations, generally based on the electron density distribution, by normal mode calculations qualifies the search for a stationary point,

which is otherwise known as the conformation representing the 'global minimum' on the potential energy surface. The search for the stationary points are important to ensure the description of an adequate molecular structure that will further reveal the molecular properties. The normal mode analysis also enables the attainment of thermochemical properties such as Gibbs energy or, free energy (G). The use of Gibbs energy to calculate the feasibility of a chemical process, using Hess's law is commonly used in the research of catalyst design. This is a powerful technique as it bridges the computationally modeled structure with properties that can be investigated using experimental methodologies and allows for modification in the computational model if necessary based on the correlation between the experimental and computational results.

In contrast to normal mode calculations, Quantum Theory of Atoms in Molecules, and Natural Bond Orbital calculations do not reveal any experimental properties that can be tested by designing an experiment directly. However, both the tools are based on the electron density distribution, which is a testable quantity. The use of QTAIM to gain insight on the short-range interactions such as hydrogen bonding reveals useful insight on the steric features and related properties of a molecular system. NBO analysis is a powerful technique that directly informs about the orbitals involvements in the bonding interaction. This is immensely popular in the field of small-molecular research as it allows us to investigate the location of electron rich and electron poor centers within a molecule, otherwise known as the 'reactive sites' for the understanding of the reactivity of a certain class of molecules such as Lewis acids, halogen bond donor-acceptors, *etc.*

This work entails the use of the aforementioned computational methodologies in conjunction with the experimental techniques to investigate the structure-function relationships of four classes of small-molecular systems: 1) proton reduction homoleptic Ni(II) catalysts, 2) heteroleptic Ni(II) catalyst for hydrogen production, 3) photocatalytic aerobic oxidation using an organocatalyst, 4) diarylhalonium salts.

The catalytic mechanism of proton reduction using Ni(II) catalysts were investigated using both experimental and computational methodologies. However, in the previous reports the computational model for the proton reduction using such catalysts overlooked the contribution of structural isomer formation based on a short-range hydrogen bonding interaction. In this report, the catalytic cycle was revisited and the model introduces the effect of H-bond driven isomerization. This improvement in the description of the molecular model provides a better correlation with the experimental observation related to these catalysts. It was observed that while modeling the small-molecular systems using computational techniques, the contribution from the short-range interactions are often disregarded. Our work on these catalysts addresses this issue and encourages the use of improved molecular models while performing computations on structurally allied systems. The research on the heteroleptic Ni(II) catalysts was guided by the observations from the homoleptic Ni(II) catalysts. Structural isomer formation and the effect of intramolecular H-bonding were considered while computationally modeling these catalysts. In addition to that, in this project the complete catalytic cycle of a structurally more complicated heteroleptic metal-ligand system was investigated with the objective of tuning the catalytic efficiency of such catalysts. This project provides useful insight to the

synthetic and experimental investigation of a new class of water splitting catalyst. The experimental observations made in the organocatalysis of H_2O_2 production and concomitant aerobic oxidation of a benzylic alcohol inspired the third project, where the catalytic mechanism was explored using the computational tools. The computational model of the catalysis is well-correlated with the experimental observation. The deeper understanding of the aerobic oxidation mechanism allows for the design of a better organo-photocatalyst that can carry-out similar type of reactions with a variety of organic substrates at mild reaction conditions, and as a result, produce a sustainable energy carrier, H_2O_2. The use of NBO studies on the DFT optimized stationary structures of the diarylhalonium salts and isoelectronic diarylchalcogenides allows for a better description of the structural model for these types of compounds. The improvements made on the existing bonding model provides a better understanding of the experimental results related to the reactivity of these molecules. To reiterate the overall theme of the work, the use of computational chemistry to investigate the SAR of small-molecular systems can provide useful insights. However, the success of these powerful techniques are contingent upon a better description of the model that can be finetuned based on the amount of correlation between the experimental and computational results.

1.4 Alternative Energy Research

Since the dawn of human civilization, we have irreversibly changed the character of our natural habitat, Earth. The Intergovernmental Panel on Climate Change (IPCC) has reported that the scientific evidence for man-made climate change is overwhelming and unequivocal.[17–19] The ongoing warming of the climate is of particular significance, more

than 95% of the recent changes in the global climate is a result of human activity since the mid-20th century. The first industrial revolution marked an unprecedented success in the rate of production, but also posed a challenge in an extreme increase in green-house gas emission. To slow the rate of green-house gas emission, we need to deviate from carbon-based fuels and search for better alternative energy sources, which will meet the global energy demand in a cleaner and more efficient way. However, developing inexpensive and efficient methods to tackle the continuous growth in the global energy demand is one of the pressing contemporary scientific challenges.[20–22]

One successful attainment of this challenge involves harnessing solar energy because of its inexhaustible supply and eco-friendly applications. Even though the sun is the largest source of energy, the intensity of radiation on earth's surface is low due to atmospheric scattering effects. Furthermore, the sunlight that penetrates the atmosphere mostly consists of visible and infrared radiation. One of the other practical challenges is the energy availability to utilization ratio. Hence, for the successful implementation of solar energy as a viable alternative to fossil-fuels, development of suitable storage method is imperative. Among various other methods, storing solar energy into a chemical bond has shown significant promise. The underlying principle behind this method is to carry-out a chemical process that utilizes solar energy to convert simple molecules into fuels. These fuels can generate energy when required, through the process of combustion or in a fuel-cell. Since this chemical process mimics the natural process of photosynthesis to bind solar energy into carbohydrates from water and carbon dioxide, it is referred to as Artificial Photosynthesis.[18,23]

There are several known chemical conversions that can ultimately bind the sun's energy into a chemical bond generating a *solar fuel*. In this report we will explore two of the most efficient solar fuels, molecular hydrogen (H_2) and hydrogen peroxide (H_2O_2) and their production pathways. H_2 is considered to be the most promising alternative to carbon-based fuels with various possibilities to attend the global energy demand. Although, H_2 is a non-condensable gas at ambient temperature-pressure condition with not so impressive *volume energy density*, it has the highest *specific energy of combustion* of all the chemical fuels and a *volume energy density* that exceeds all batteries. Furthermore, burning H_2 does not leave any carbon footprint. H_2 can be accessed from the reductive side of the *water splitting reactions* through the reduction of aqueous protons. On the other hand, H_2O_2 is a liquid, non-explosive fuel which can generate electricity when used in a fuel-cell producing water as the only waste product. H_2O_2 is an excellent and sustainable energy carrier and can be produced by the two-electron reduction of O_2. When compared to H_2, the use of H_2O_2 is more advantageous and practical because it is almost \$1.5/gge cheaper. The bottleneck of the widespread use of H_2O_2 as a fuel is its susceptibility toward decomposition and inefficient production pathways.[24–26]

1.5 Water Splitting for Hydrogen Production

As fascinating and simple it might sound, producing molecular H_2 and O_2 from water (H_2O) in an experimental set-up is extremely challenging due to the high *overpotential* associated with the inert reaction kinetics. It is for this reason involvement of a suitable catalyst is imperative to lower the *overpotential* of the water splitting reaction in ambient temperature-pressure conditions.[20] To use molecular H_2 as a viable chemical

fuel for long term use on a global scale, the water splitting reactions must be light-driven, and the overall process will require a photosensitizer (PS), an electron source, aqueous protons, and a catalyst to reduce the overpotential of the reaction. That being said, there are a number of ways to refine or optimize the process of the photogeneration of H_2 gas. Several attempts have been made in this field for over the last 45 years studying the reductive half of the water splitting reaction. However, in this report, we will be strictly focusing on a specific kind of proton reduction catalyst which has proven to be very efficient in sustainable production of H_2 from water.[20–22]

Due to lower overpotential for proton reduction, Pt and Pd complexes were most frequently studied as H_2 generation catalysts. But due to the low abundance and higher cost of these metals, the interest has been shifted to the research of noble-metal free catalyst design for water splitting. Several transition metal complexes with Fe, Co, Ni have been proven to be effective for water splitting. Especially, the nickel(II) tris-pyridinethiolate, **$[Ni(PyS)_3]^-$**, catalyst has shown high efficiency and stability in both photochemical and electrochemical systems.[27–29]

1.5.1 Computational modeling of homoleptic $[Ni(PyS)_3]^-$ catalysis.

The catalytic mechanism of hydrogen production from proton reduction was explored using both computational and experimental methodologies. A molecular model, supported by the experimental observations made by spectroscopic and electrochemical techniques, reveals that the catalytic cycle initiates by the protonation of one of the pyridyl N and dechelation from the metal center. This is followed by a one electron reduction step and

subsequent Proton Coupled Electron Transfer (PCET) to generate a Ni-hydride intermediate.[30] This step brings to H atoms close to each other that ultimately leaves as a dihydrogen molecule through the formation of a covalent bond, closing the catalytic cycle.

This model did a decent job of explaining the experimental observations, however, left room for improvements. Revisiting the literature on these types of molecules revealed that the complex prefers a particular ligand orientation around the transition metal center observed by X-ray crystallographic methods.[31] This ultimately gives rise to asymmetric chemical environments around the pyridyl N atoms; hence the proton affinity of the N atoms are unequal.

Computational modeling on the structure of the **$[Ni(PyS)_3]^-$** revealed that the energy of the *meridional* isomer is lower than the corresponding *facial* isomer as observed in the X-ray structure determination. The catalytic mechanism was reevaluated by separately protonating each of the pyridyl N atoms to test for the preferential protonation step. It was observed that the protonation generates four structural isomers of the intermediate. The initial computation assumes that protonation is dictated by the thermodynamic *trans effect*. However, the improved molecular model reveals that the protonated isomer formed as guided by *trans effect* contributes the least amount to the overall population. QTAIM based topology analyses report that the protonation is guided by the formation of an intramolecular H-bond rather than the thermodynamic *trans* effect. This modification in the molecular model provides a better correlation between the calculated and experimentally observed pK_a values. Furthermore, provides a logical explanation to the absence of a true isosbestic point in the UV-Vis titration varying pH of the solution. During

the reduction of the catalytic intermediates, the coordination geometry around the Ni center changes to a trigonal bipyramidal geometry from a square pyramidal geometry.

The observations made for the unsubstituted **[Ni(PyS)$_3$]$^-$** were tested for eleven substituted complexes with different electron donating and electron withdrawing groups on different carbon centers of the aromatic thiopyridyl ligands. Structural isomerization upon protonation was observed irrespective of the electronic and steric configuration of the donating ligand atoms.

The exploration of the catalytic mechanism of the water splitting by **[Ni(PyS)$_3$]$^-$** using better molecular model provides a better understanding of the structure-function relationship. The importance of considering short-range interactions in small-molecular catalysts opens up a new direction in the catalyst design research.

1.5.2 Heteroleptic nickel(II) catalyst design for water splitting.

This work capitalizes on the importance of protonation and subsequent reduction steps during the catalytic water splitting to produce H_2 gas by the Ni(II) catalysts. The efficiency of these catalysts can be tuned by the heteroleptic ligand modification, meaning installing different ligands around the metal center with the objective that one type of ligand will optimize the protonation step while the others will affect the reduction step.[32] Installation of electron donating group improves the pK_a while reduction potential (E^0) is affected by the introduction of an electron withdrawing group on the metal-ligand framework. Both the steps need to be optimized simultaneously for a better catalytic activity hence it is required to design a heteroleptic Ni complex.

This work constitutes the detailed study of two heteroleptic Ni(II) catalysts. The electron donating -CH_3 and electron withdrawing -CF_3 groups were introduced to the ligand framework in 2:1 and 1:2 ratio. The computationally designed heteroleptic catalysts were compared with the analogous homoleptic catalysts with same ligand environment around the Ni centers for the optimization of the design.

The structurally more complicated heteroleptic catalysts showed the possibility of generation of a large number of geometric isomers upon protonation, guided by intramolecular H-bonds, as seen in case of the homoleptic catalysts. The reduction step for the heteroleptic catalysts changes the coordination geometry around the metal center through the reorganization of the ligands. The pK_a of the pyridyl N atoms containing the electron donating -CH_3 group is higher than the electron withdrawing -CF_3 group containing ligands. While the more -CF_3 group containing complex had a more positive E^0 value indicating an easier reduction step.

When the results from the heteroleptic catalysts were compared with the structurally analogous homoleptic complexes it was observed that the thermodynamic parameters guiding the catalytic efficiency had intermediate values between the two extrema marked by the homoleptic catalysts. It was also observed that both the heteroleptic complexes has a similar thermodynamic feasibility for the penultimate PCET and final hydrogen evolution steps, further justifying catalyst modification targeting the first two steps. Furthermore, this study reveals that the ideal configuration for a Ni(II) complex that can catalyze the proton reduction requires one electron donating group in the ligand environment ensuring protonation of a specific pyridyl N atom and two electron

withdrawing groups for a more spontaneous reduction step.

The computational design on the heteroleptic Ni complexes provides a novel strategy for finetuning the catalytic efficacy of a well-known water splitting catalyst. This strategy can be extrapolated to the other transition metal-ligand complexes following similar mechanism by targeting the thermodynamic parameters responsible for the catalytic activities. The chemical properties responsible for a successful catalytic turnover can be modified by simple and selective structural modification around the ligand environment.

1.6 Aerobic Oxidation and H_2O_2 Production

Oxidation reactions are important for the production of many agro- and pharma-chemicals and often use stoichiometric metal-oxides that produce significant amounts of toxic waste.[33] The use of oxygen from the air as the terminal oxidant would eliminate this waste. However, aerobic oxidation reactions are challenging and often require transition-metal catalysts. Nevertheless, aerobic oxidation can be achieved using photocatalysis. Primary and secondary alcohols can be oxidized to corresponding higher-value aldehydes and ketones.[34–36] With that objective, we have designed a novel strategy to use aerobic oxygen as an oxidant to oxidize benzylic alcohols using a metal-free catalyst under photochemical conditions. This process produces hydrogen peroxide (H_2O_2) as a by-product. H_2O_2 is not only one of the most industrially relevant molecules, but also is a sustainable energy carrier that can be used as fuel to generate electricity. Oxidizing industrially relevant alcohols to high-value products using a metal-free photocatalyst is a novel approach to address aerobic oxidation reactions while the photochemical production

of H_2O_2 has potential industrial applications. The current method of H_2O_2 production utilizes the *Anthraquinone Process* (AP) that uses H_2 and O_2 and a Pd catalyst.[37,38] This process requires large chemical plants and major disadvantages include mass-transport limitations of hydrogenation and oxidation steps, and substantial investments for purification, storage, and distribution. Only a handful of chemical plants produce over 4.5 million tons of H_2O_2 that are used industrially every year, which is then shipped to the point-of-use. Our goal is to optimize a greener method of H_2O_2 production by investigating the mechanistic pathways, designing better catalysts, and potentially broadening the window of oxidizable materials for widespread application through synthetic and experimental strategies with computational methodologies.

The photocatalytic aerobic oxidation of benzylic alcohols to carbonyl compounds utilizes an organo-photocatalyst, *N*-Hydroxyphthalimide (NHPI). The use of NHPI as a catalyst (and cocatalyst along with metal complexes) is well-known for a variety of chemical transformations, such as sp^3 C-H bond activation, C-C bond activation, alkane oxidation *etc.*[34–36,39,40] However, these reactions are generally performed under thermal conditions. In some cases, NHPI is used in stoichiometric amount for successful application. But recent reports have shown a growing interest in the use of NHPI in catalyzing reactions under photochemical conditions. This can be attributed to the generation of phthalimide-*N*-oxyl (PINO) radical by a homolytic cleavage of the O-H bond in NHPI. PINO is thought to be the active radical that initiates a radical cascade mechanism by the abstraction of a H atom from the organic substrates. PINO radical decomposes at 85 - 90 ^{0}C. Hence using thermal condition is not beneficial.[35]

The NHPI catalyzed aerobic oxidation of alcohols and concomitant production of H_2O_2 was reported under thermal conditions, earlier. This method utilizes 10 mol% catalyst loading and shows 50% yield of H_2O_2.[40] The advantage of the novel photochemical method, explored herein, is the requirement of lower catalyst loading (5 mol%) and a high stability of the products under reaction conditions. No decomposition product was observed on the ^1H NMR spectra of the reaction condition after 18 days. Both of which can be attributed to the decomposition of PINO under elevated thermal conditions.

The reaction mechanism of this process was studied using computational methodologies. It was observed that the reaction utilizes singlet oxygen as the reactive oxygen species which was correlated by the experiments. In presence of light and singlet oxygen the O-H bond in NHPI cleaves and forms PINO. PINO abstracts the H atom from the alcohol to regenerate NHPI. The hydroxyl radical generated, thus reacts with singlet oxygen to, ultimately producing a carbonyl compound through a series of radical mechanism and release a H_2O_2 molecule.

The use of NHPI to perform aerobic oxidation reactions addresses different challenges in the field of aerobic oxidation catalysis. First and foremost, this method is a greener alternative to most common alcohol oxidation reactions. NHPI is a simple organic compound, this allows us to tune the efficiency through simple modifications. Photochemical oxidation can be performed at room temperature or lower without the decomposition of the reactive intermediates. Most importantly, this method generates H_2O_2 as a value-added product. Due to the absence of any metal-based strong oxidizing agent and harsh reaction conditions, the generated H_2O_2 will not be decomposed and can be

extracted from the mixture with simple liquid-liquid extraction.[40] The understanding of the mechanism of aerobic oxidation catalyzed by NHPI allows us to broaden the scope of reaction by sampling a variety of substrates, which is of immense interest at both laboratory and industrial scale.

1.7 Computational Modeling of Diarylhalonium Salts

Diarylhalonium compounds have emerged as catalysts and reagents in a wide variety of organic conversions. The mild reaction conditions have allowed these molecules to be suitable for sustainable chemical research.[41] Despite the attention and surge in the use of these reagents, the lack of understanding of the bonding, have limited the knowledge about the structure-activity relationship.

The widely accepted bonding theory for these types of molecules is termed the three center-four electron (*3c-4e*) model.[42,43] This model describes the bonding in hypervalent halonium salts by the involvement of an unhybridized *p*- orbital from the central halogen atom. Under the description of this model the hypervalent bonds in the halonium complexes form a symmetric linear triad with an internal bond angle of 180°. As a result of which the bond angle between the aromatic carbon atoms and the central halogen atom is 90°. However, the experimentally observed X-ray bond angles are quite deviated from the theoretically predicted bond angles. Furthermore, the experimental structural parameters show that the C-X-C bond angles are much wider when the central halogen is a smaller chlorine atom than a larger iodine atom. The chemical properties such as Lewis acidities of these type of compounds calculated based on the simplistic *3c-4e* model was erroneous

and showed very poor correlation with the experimental results. Evidently, a refinement of the existing bonding model was necessary.

In attempt to make improvements to the *3c-4e* model which can encompass most structural features of diarylhalonium salts and hence give insight to the experimental chemical reactivity, a series of known diarylhalonium compounds were studied using DFT calculations. It was observed from the NBO analysis of the electron density of these molecules, as opposed to the accepted bonding theory, the central halogen atoms use both *s*- and *p*- to accommodate the incoming ligands. When the concept of orbital mixing was introduced the calculated bond parameters showed excellent correlation with the experimentally observed structures. This model describes that the lighter halogen atoms uses more %*s*- character to the bonding than the heavier group congeners accounting for a higher C-X-C bond angle. Similar observations were made when the theory was applied to the isoelectronic diarylchalcogenides. The Lewis acidities of three newly synthesized and characterized unsymmetric phenyl(mesityl)halonium compounds were investigated using both computational and experimental methodologies. The calculated properties were in agreement with the experimental results and could accurately predict the periodic dependence in the reactivities of those compounds.

This updated generalized bonding model to describe the structural behavior in diarylhalonium and diarylchalcogenide compounds and their associate reactivities suggests the importance of considering the concept of orbital mixing while describing the bonding models. The excellent correlation between the experimental and theoretical results indicate

that this model can be used to describe interactions such as halogen- and chalcogen bonding shown by other main group elements.

1.8 Summary

This report underlines the importance of the choice of adequate molecular model to understand the structure-function relationship in a number of molecular systems. Since the development of computational methodologies extensive has increased the understanding of the molecular systems. However, an adequate and well-rounded molecular model is necessary for general success, measured by the correlation between experimental observations and calculated results. Otherwise, it will lead to an erroneous and incomplete understanding of the molecular system.

The DFT calculations and subsequent QTAIM based topology analyses to investigate the role of an intramolecular H-bonding interaction on the catalytic cycle of homoleptic Ni(II) catalysts is disclosed in Chapter 2. This work was published in Dalton Transactions in 2022. Chapter 3 details the computational study of the catalytic mechanism of heteroleptic Ni(II) water splitting catalysts. This work was submitted to Canadian Journal of Chemistry. The work on aerobic oxidation of benzylic alcohols and concomitant production of H_2O_2 is described in Chapter 4. A provisional patent document was filed based on this work. Chapter 5 moves on to describe the generalized bonding model for diarylhalonium and diarylchalcogenides and published in Chemical Science in 2022. Final conclusions are described in Chapter 6.

Chapter 2 Computational Investigation Into Intramolecular Hydrogen Bonding Controlling the Isomer Formation And pK_a of Octahedral Nickel (II) Proton Reduction Catalysts

Bhattacharjee, A.; Brown, D. S. V.; Virca, C. N.; Ethridge, T. E.; Mendez Galue, O.; Pham, U. T.; McCormick, T. M. Computational Investigation Into Intramolecular Hydrogen Bonding Controlling the Isomer Formation And pK_a of Octahedral Nickel (II) Proton Reduction. *Dalton Trans.* **2022**, *51*, 3676 – 3685.

2.1 Introduction

Electrochemical and photochemical proton reduction catalysts that generate hydrogen from water have potential applications in storing solar energy through artificial photosynthesis.[17,20] The pK_a of such compounds can play a critical role in their reactivity and the conditions in which they operate. Proton reduction catalysts are characterized by the pH required for protonation of the catalyst, as well as the electrochemical potential (E^0), required for hydrogen production.[44–48] Understanding the structural factors that contribute to pK_a and E^0 is critical to predict structure-function relationships.[49–52] Computational studies allow for the detailed investigation of these two thermodynamic properties of the catalyst.[53,54] The extensive use of DFT has allowed for notable success in the field of catalyst design, ligand modification, and enhancement of catalytic efficiency, in particular for homogeneous metal catalysts, and thus has proven to be an indispensable tool.[16,30,55–59] However, it is imperative to acquire a thorough knowledge of the intricacies involved in a

system through a judicious survey of the molecular model that can justify the mechanistic details of the catalytic cycle in order to obtain unambiguous results.

Homogeneous catalysts based on earth-abundant metals have been shown to be efficient in converting protons to hydrogen gas.[27,28,60–71] This work examines the computationally derived structures involved in the catalytic cycle for hydrogen production by tris-(pyridinethiolato)nickel (II), often reported as nickel (II) tris-(pyridinethiolate), **$[Ni(PyS)_3]^-$**, and its derivatives, originally developed by Eisenberg and co-workers.[28,70] The catalytic cycle has been proposed to proceed through a CECE (Chemical-Electrochemical-Chemical-Electrochemical) mechanism, starting with protonation of one of the pyridyl N atoms (**Figure 2-1**).[29] Both computational and X-ray studies have shown that the three pyridinethiolate (PyS^-) ligands are oriented in a pseudo-octahedral meridional geometry around the Ni(II) center.[29,32,70] The asymmetric chelation of bidentate PyS^- ligands results in each coordinated atom occupying a unique chemical environment. In this computational work, we show that protonation of each of the three pyridyl N atoms results in geometric isomers of the protonated intermediate with calculated pK_a values varying by up to ~3 pK_a units between the isomers for a single compound.

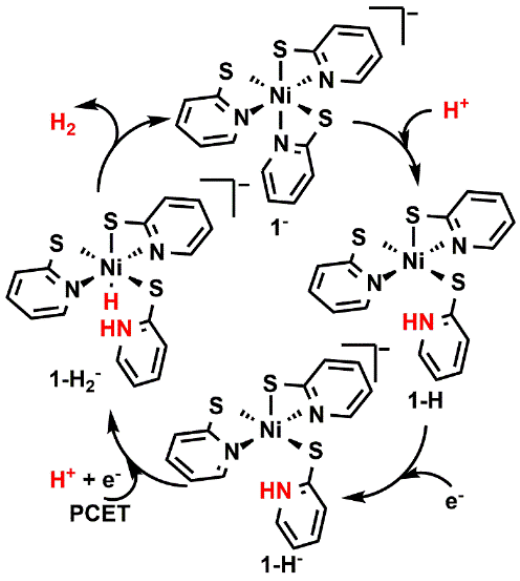

Figure 2-1. The proposed catalytic cycle of **[Ni(PyS)$_3$]$^-$** catalyst. Compound **1**$^-$ is protonated at a pyridyl N to form **1-H**. This is then reduced to **1-H**$^-$. Subsequent addition of another proton and electron makes the intermediate **1-H$_2$**$^-$ that can release H_2 to regenerate **1**$^-$.

The formation of geometric isomers during the catalytic cycle of H_2 production by **[Ni(PyS)$_3$]$^-$** has not been considered previously. By separately modeling all possible isomers formed by the protonation of the starting **[Ni(PyS)$_3$]$^-$** catalyst, we are able to identify structural elements that significantly impact the calculated thermodynamic parameters of each geometric isomer. Specifically, we have found that intramolecular H-bonding plays a key role in the pK_a values of the different protonated isomers of the catalyst. H-bonding has a pivotal role in explaining the structure-function relationship in large macro-molecular systems like proteins.[72–75] However, large changes in the pK_a of small inorganic complexes due to intramolecular H-bonding have been relatively unexplored. Reports by Kass *et al*, showed the importance of inter- and intra-molecular H-

bonding on the pK_a of organic acids and their reactivity.[76,77] The effect of H-bonding on the transition metal catalysis has also been reported in experimental and computational studies where they found H-bonding can facilitate the catalytic pathways by stabilizing intermediates. For example, hydrogen evolution $\mathbf{[Ni(P_2N_2)_2]^{2+}}$ type catalysts shows an intramolecular Ni…H-N bonding during catalysis.[78] Another Ni(0) catalyst operates in reversible alkenyl functional group swapping reaction by the formation of catalytic intermediates stabilized by H-bonding interactions.[79] Intramolecular H-bonding, however rare, plays a crucial role in small molecule catalysis. Through computations, we have found the calculated structure of protonated $\mathbf{[Ni(PyS)_3]^-}$ catalyst is complicated by both isomer formation and intramolecular H-bonding. We have found that the lowest energy isomer formed during the protonation step of the catalytic cycle is controlled through the H-bond stabilization energy which overcomes the thermodynamic *trans* effect.

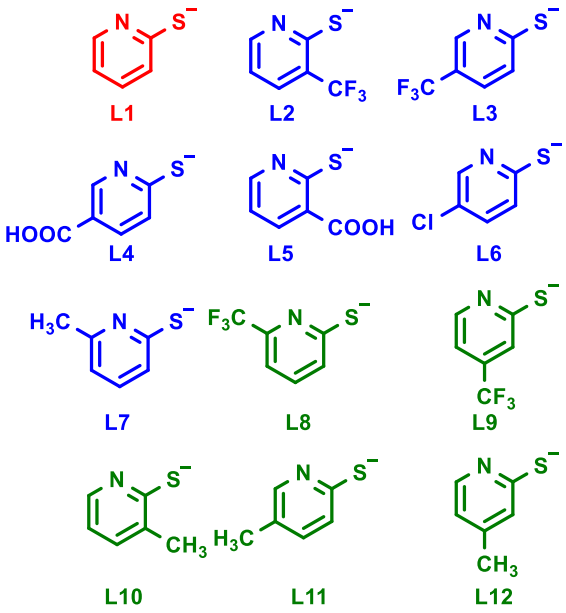

Scheme 2-1. Pyridinethiolate (PyS^-) ligands used to model the family of **[Ni(PyS)$_3$]$^-$** catalysts: The unsubstituted ligand (L1, red); The homoleptic complexes containing ligands L1–L7 (blue) has been investigated both experimentally and computationally; The complexes containing ligands L8–L12 (green) have been studied only computationally.

Ligand modification is often employed to improve catalytic turnover frequency and overpotential by tuning the pK_a and E^0.[28,32] We have found, through the modeling of several catalysts with ligand modification, that structural changes result in unique population distributions of the isomers for each catalyst, which do not directly correlate with the electronic effects of the substituents. This work explores the role of intramolecular H-bonding on the structure and stability of the catalytic intermediates of the proton reduction catalyst, **[Ni(L1)$_3$]$^-$** and six derivatives (**[Ni(L2)$_3$]$^-$** through **[Ni(L7)$_3$]$^-$**) using computational methodologies and compared to experimental results (**Scheme 2-1**). The knowledge gathered from those compounds were further employed to five other derivatives with ligands that are not commercially available (**[Ni(L8)$_3$]$^-$** through **[Ni(L12)$_3$]$^-$**) using

computational modeling (**Scheme 2-1**). The comparison to experimental data highlights the necessity of computationally considering the structural isomers to provide an explanation for unanticipated results. We have calculated pK_a, E^0 values, and the Boltzmann population distribution of the geometric isomers of each catalyst based on computed thermodynamic energies. Topological analyses further revealed that the varying stability of these isomers results from the strength of the intramolecular H-bond between the H attached to the pyridyl N and the S atom from an adjacent PyS^- ligand. The structure-reactivity relationship uncovered herein highlights the importance of carefully considering geometric isomers while conducting computational studies on octahedral complexes. This report aims to benefit chemists studying the catalytic mechanism of octahedral metal-ligand complexes to understand their system in greater detail.

2.2 Methods

2.2.1 Density Functional Theory (DFT) Studies.

The quantum chemistry package Gaussian 09 suite of programs was used to perform all of the calculations in this report.[80] The geometries of the starting catalyst, **1**$^-$ were optimized in both *singlet* and *triplet* spin states at three different DFT level of theories namely, B3LYP, B3P86, M11-L with 6-311+G(2df,2pd) basis sets in polarized continuum (PCM) water solvation model. The *triplet* configuration of the starting catalyst was chosen by comparing the single-point energies to the singlet states at all the DFT level of theories (**Appendix Table 1**).[29] The B3P86 functional was chosen for the subsequent calculations, as it best described the geometries of the starting catalysts with the most negative single-point energies for all of the catalysts reported herein. The isomers of protonated

intermediates, **1-H**, were modeled with B3P86/6-311+G(2df,2pd) at a *triplet* spin state employing both water and acetonitrile continuum solvation models, while the isomers of reduced intermediates, **1-H**$^{-}$, were modeled at *doublet* spin state utilizing the same method in both water and acetonitrile implicit solvent models. The frequency calculations were performed on the stationary points and resulted in no imaginary frequencies. The Gibbs energies (*G*) for each intermediate were obtained using the sum of thermal and electronic energies from the thermochemistry calculation using normal mode analyses. The free energy change (ΔG^0_{rxn}) for all the reactions were calculated using *Hess's law* of constant heat summation.

2.2.2 Calculated pK_a Values.

The complexes were protonated at the three different N atoms separately, creating the protonated isomers. The geometry of each isomer was optimized, and the pK_a of the individual protonated isomers were calculated (**eqn. 2.1**).

$$pK_a = -\frac{\Delta G^0}{RTln10} \tag{2.1}$$

Here, ΔG^0 is the free energy change for reaction described by **eqn. 2.2**, *R* is the universal gas constant and *T* is the absolute temperature of the system (*298.15 K)*. For the following acid-base reaction described by **eqn. 2.2**, the free energy change (ΔG^0_{rxn}) of reaction is calculated as follows (**eqn. 2.3**):

$$1^- + H^+ \rightarrow 1 - H \tag{2.2}$$

$$\Delta G^0_{rxn} = G_{1-H} - (G_{1^-} + G_{H^+}) \tag{2.3}$$

The free energy change for this acid-base reaction was calculated using the parametric value of *-264 kcal/mol the energy* for a water solvated proton (G_{H^+}) that includes translation entropy and solvation free energy.[30,81–83]

2.2.3 Calculated E^0 Values.

Reduction potential values (E^0) were calculated for the reduction steps for all the protonated isomers. The ΔG^0 for the *isodesmic* reaction (**eqn. 2.4**) was used to obtain the E^0 of the reduction reactions employing **eqn. 2.5**, where F is Faraday's constant and E^0_{ref} is the experimentally reported E^0 for the conversion of **[Ni(PyS)$_3$]H** to **[Ni(PyS)$_3$]H$^-$**, *-1.62 V vs.* SCE.[32]

$$[Ni(PyS)_3]H + 1 - H^- \rightarrow [Ni(PyS)_3]H^- + 1 - H \tag{2.4}$$

$$E^0 = -\frac{\Delta G^0}{F} + E^0_{ref} \tag{2.5}$$

Computational pK_a and E^0 values, are compared to previously reported experimental data.[32,29]

2.2.4 Thermodynamic Population Analysis.

The relative population (x) of each of the isomers for the complexes were calculated using the Boltzmann distribution formula at *298.15 K* and normalized to unity with respect to the most stable isomer, assuming the population was determined only by the thermodynamic stability (**eqn. 2.6**), where ΔG_i^0 is the difference in the free energy of the most stable isomer relative to another isomer, R is the universal gas constant, and T is the absolute temperature.[84] Based on the population analysis, the weight-averaged pK_a values

were calculated for the protonated isomers by taking a weighted sum of the pK_a values for the individual isomers and dividing it by 100.

$$x = \frac{\exp\left(-\Delta G_i^0 / RT\right)}{\sum_i \exp\left(-\Delta G_i^0 / RT\right)} \times 100 \tag{2.6}$$

2.2.5 Quantum Theory of Atoms in Molecules Analysis.

The intramolecular H-bonds that stabilize the isomers were investigated by the topological analysis of the electron density distribution using Bader's Quantum Theory of Atoms in Molecules (QTAIM).[85,86] Wavefunction files for the AIM analyses were prepared from the optimized structures of the complexes using Gaussian 09 package and further analyzed by Multiwfn 3.7 program.[80,87] The bond energies (*BE* in *kcal/mol*) of the intramolecular H-bonds were calculated using **eqn. 2.7**, where ρ(r) is the electron density at the bond critical point (BCP) corresponding to the H-bonding interaction.[88–90]

$$BE \approx -223.08 * \rho(r) + 0.7423 \tag{2.7}$$

2.3 Results and Discussion

2.3.1 Structure of catalysts.

The unsubstituted $[Ni(L1)_3]^-$, 1^-, adopts a pseudo-octahedral geometry, where the Ni (II) center is coordinated by three bidentate pyridinethiolate (PyS^-) ligands. Based on the orientation of the ligands around the metal center, the compound might have two geometrical isomers: facial (fac) or meridional (mer). X-ray crystallographic studies, supported by computational investigations, reveal 1^- is thermodynamically more stable in

the chiral mer geometry over the fac geometry.[28] Computational modelling of the mer isomer of $[Ni(L1)_3]^-$ was performed using three functionals, B3P86, B3LYP, and M11-L using 6-311+G(2df,2pd) basis sets, in both singlet and triplet spin states. The triplet spin state of the catalyst is calculated to be about 0.02 Hartrees more stable over the singlet spin state, irrespective of the choice of the functional (**Appendix Table 1**). This is supported by paramagnetic broadening observed in the NMR spectrum of the complex.[28] The lowest single point energy was obtained for the B3P86/6-311+G(2df,2pd) as a triplet state in the mer geometry which best described the structure of the catalyst. Since the three bidentate PyS^- ligands are oriented in mer configuration, the chelation is unsymmetrical resulting in the three chelating pyridyl N atoms, and the thiolate S atoms all being different from one another.

The same methods were followed while modelling the ligand modified **$[Ni(PyS)_3]^-$** catalysts. Ligand modification through substituting ED and EW groups on the pyridyl ring shows an interesting effect on the structure of the catalyst. When there is a substitution on the C-6 atom of the aromatic ring, the fac isomer becomes preferred, which is observed through structure determination using X-ray crystallography for **$[Ni(L7)_3]^-$** and via DFT optimized structures by comparing the single-point energies of both the fac and mer isomers of the same compound.[28] This is observed computationally when C-6 was substituted with an ED methyl group (CH_3) as well as EW trifluoromethyl group (CF_3), which led us to believe that this phenomenon is solely governed by steric effects and not electronic effects.[28] In the fac form of the catalyst, the three chelating N atoms are equivalent due to an identical chemical environment which they belong to (all are trans to

a chelating S). Hence, the chemical behavior of these atoms is identical and the pK_a values are the same. However, substitutions made on either C-3, C-4, or C-5 atom do not alter the mer arrangement of the ligands around the metal center seen for the unsubstituted catalyst. Hence, these ligand-modified catalysts also have asymmetrical pyridyl N atoms and will result in isomers upon protonation that will need to be considered while computationally modelling these compounds.

Compound 1^- has been shown to catalyze the conversion of H^+ to H_2 under both photochemical and electrochemical conditions (**Figure 2-1**).[28,29,32,70] We have previously reported that the catalytic mechanism is initiated by the protonation of one of the three

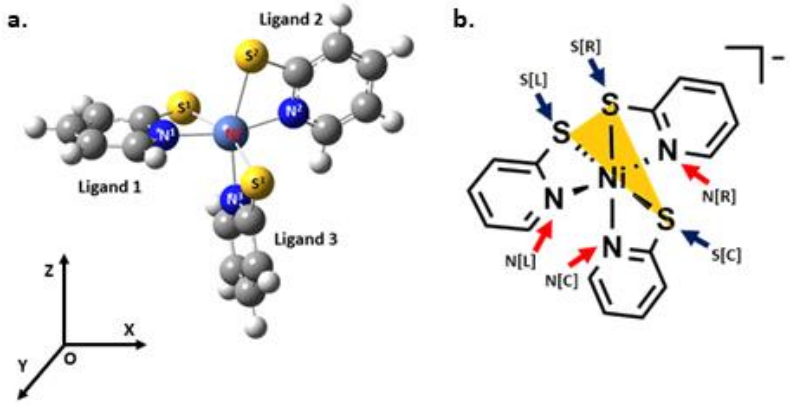

Figure 2-2. a. Ball and stick representation of the geometry around the Ni-center demonstrating the three different N and S environments, **b.** Nomenclature of the three different pyridyl N atoms. N[R] lies right of the plane of S atoms, N[C] lies in the plane, and N[L] lies to the left of the plane.

pyridyl N atoms, which forms a penta-coordinated **1-H** intermediate.[29] The next step of the catalytic mechanism is the reduction of **1-H** to **1-H**$^-$ intermediate. Computational modelling was performed on **1**$^-$, as well as **1-H** and **1-H**$^-$ in order to calculate the thermodynamic parameters (pK_a and E^0) responsible for the catalytic activity. The asymmetric environment around the Ni has not been previously considered, and the unique electronic and geometric

environment of each N, form three possible protonation sites for the first step of the catalytic cycle.

2.3.2 Protonation of ***Ni[(PyS)$_3$]$^-$*** *catalysts.*

The three possible protonation sites on different N atoms can be visualized when the molecule is oriented such that the two trans S atoms are placed on the equatorial plane of the octahedron, one pointing away and the other into the plane of the page. The third S atom is oriented to the apical position that is along the positive Z-axis, leaving the trans N atom to be on the apical position along the negative Z-axis (considering the Ni center to be the origin). Hence, the bottom apical N atom is connected to the S atom coming into the plane of the page. In this orientation, we can identify the different pyridyl N atoms as N^1, N^2, and N^3, and thiolate S atoms as S^1, S^2, and S^3, where S^1 and N^1 are on the same ligand. N^3 is trans to S^2, and while both N^1 and N^2 are trans to one another, S^1 is trans to S^3 while S^2 is trans to N^3 (**Figure 2-2a**). Due to the asymmetry of the three PyS^- ligands, the pyridyl N atoms are electronically and geometrically distinct from one another. The first step in the catalytic cycle is protonation of a pyridyl N.[29] Computationally, any one of the pyridyl N atoms can be protonated. Care must be taken when performing computational studies on such structures as appropriate choice of the correct isomer can alter computational results.

We have established a nomenclature to identify the isomers formed through protonation of each of the N in 1^-. Pyridyl N atoms can be distinguished by drawing an imaginary plane containing S^1, S^2, and S^3 atoms (yellow plane) (**Figure 2-2b**). If N^3 atom, which belongs to the plane, is oriented down, then N^1 and N^2 atoms will be on the left and right side of that imaginary plane, respectively. For clarity and simplicity, we have identified N^3 as the central (N**[C]**), N^1 as left (N**[L]**), and N^2 as right (N**[R]**) N atom. Thus, if N**[C]** is protonated, we call the generated isomer the **[C]** isomer of **1-H**; therefore, protonation of N**[L]** and N**[R]** results in the formation of **[L]** and **[R]** isomers of **1-H**, respectively (**Figure 2-3**).

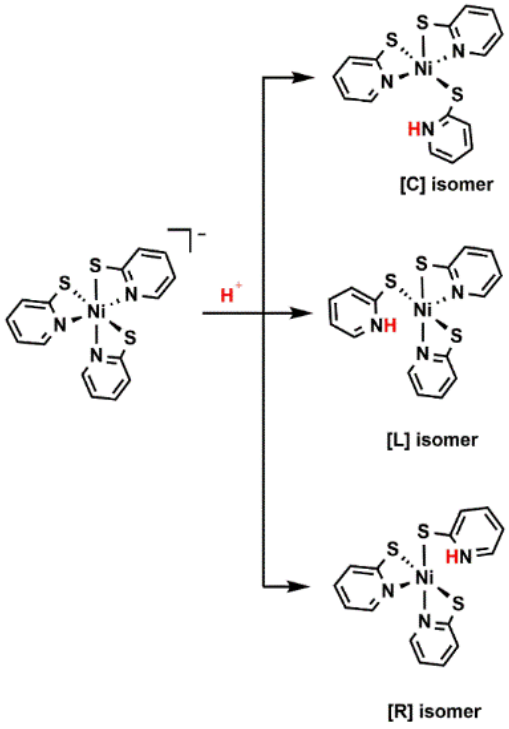

Figure 2-3. Formation of isomers upon protonation of the different pyridyl N atoms without considering the intramolecular hydrogen bonding between the introduced proton on the pyridyl N atom and adjacent thiolate S atoms.

The protonated intermediates, **1-H** were modeled by optimizing structures formed by separately dechelating each of the three pyridyl N atoms (N**[C]**, N**[L]**, and N**[R]**) and protonating them. This generated different geometric isomers of **1-H** that were studied using QTAIM-based topology analyses. This revealed that the proton that is attached to the pyridyl N atom can form an intramolecular H-bonding interaction with a S atom from either of the two adjacent PyS^- ligands. For example, after protonating N**[C]**, the newly introduced proton can participate in an intramolecular H-bonding with either S**[L]** or S**[R]** (N[C]-H…S[L] or N[C]-H…S[R]). Protonation of N**[L]** shows similar interaction with either S[C] or S[R] (N[L]-H…S[C] or N[L]-H…S[R]) and protonation of N**[R]** leads to the possibilities of two interactions, either with S[C] or S[L] (N[R]-H…S[C] or N[R]-H…S[L]). This leads to the possibility of formation of six protonated complexes: N[C]-H…S[L] or [C_L]; N[C]-H…S[R] or [C_R]; N[L]-H…S[C] or [L_C]; N[L]-H…S[R] or [L_R]; N[R]-H…S[C] or [R_C]; N[R]-H…S[L] or [R_L]. However, topology analyses assisted by DFT calculations reveal that [C_L] and [C_R], and [R_C] and [R_L] respectively, are the same compound with identical thermodynamic stabilities and properties, collectively referred to as the [C] isomer of 1-H, and the **[R]** isomer of **1-H**, but [L_C] and [L_R] optimize to distinct compounds which reduces the number of isomers formed due to the protonation of 1^-, to four: **[C]**, **[L_C]**, **[L_R]**, and **[R]** (**Figure 2-4**).

The isomers have different thermodynamic stabilities, and hence calculated pK_a values (**Table 2-1**). For example, considering the unsubstituted **[Ni(L1)$_3$]$^-$**, the calculated pK_a's of **[C]**, **[L_C]**, **[L_R]**, and **[R]** isomers are 11.4, 11.1, 12.2, and 12.4 respectively (**Table 2-1**). The [R] isomer is calculated to be 1.4 kcal/mol, 1.9 kcal/mol, and 0.4 kcal/mol more

stable than the **[C]**, **[L$_C$]**, and **[L$_R$]** isomers, respectively. To compare these values to the experimental pK_a value that is reported to be 12.1[70] we could choose the most stable isomer (pK_a 12.4), or attempt to consider all isomers. Calculation of the Boltzmann's distribution on the computationally modeled structures reveals that at room temperature isomer **[R]** would have a 60% contribution, **[C]** has 5%, **[L$_C$]**, and **[L$_R$]** have 2% and 32% contribution, respectively (**Table 2-1**). The weight-averaged calculated pK_a value of the individual isomers is 12.3. The choice of how to correlate computational data to experimental values will be system specific, however this highlights the importance of carefully considering all possible structures in the computational investigation.

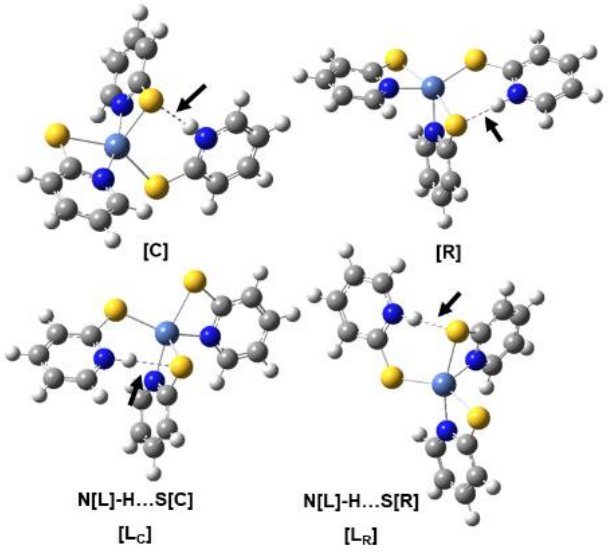

Figure 2-4. Topology maps represented by ball and stick models of **[C]**, **[L$_C$]**, **[L$_R$]**, and **[R]** isomers of **[Ni(L1)$_3$H]** where blue, grey, yellow, white, and indigo balls represent N, C, S, H and Ni atoms, respectively. Black arrows point toward the intramolecular N-H…S H-bonding interactions.

Table 2-1. The calculated pK_a in an implicit water solvation for each isomer is presented with the thermodynamic Boltzmann distribution of the isomers at room temperature and the experimental pKa value.

Group	Complex	Calculated pK_a (%Distribution)			Weight averaged pK_a	Experimental pK_a	
		[C]	[L_C]	[L_R]	[R]		
-	$[Ni(L1)_3H]$	11.4 (5.27)	11.1 (2.51)	12.2 31.93)	12.4 (60.30)	12.3	12.1
3-CF_3	$[Ni(L2)_3H]$	6.7 (1.52)	6.3 (0.58)	7.0 (3.19)	8.5 (94.70)	8.4	8.3
5-CF_3	$[Ni(L3)_3H]$	6.7 (1.12)	6.7 (1.12)	7.3 (5.38)	8.6 (92.37)	8.5	7.4
6-S-3-COOH	$[Ni(L4)_3H]$	12.1 (2.88)	11.8 (1.37)	12.7 (10.16)	13.6 (85.59)	13.5	10.3
2-S-3-COOH	$[Ni(L5)_3H]$	-4.6 (5.45)	-5.2 (1.23)	-3.9 (24.01)	-3.5 (69.30)	-3.7	8.6
5-Cl	$[Ni(L6)_3H]$	8.2 (4.59)	8.0 (3.00)	8.9 (20.23)	9.4 (72.18)	9.2	7.6
4-CF_3	$[Ni(L9)_3H]$	6.9 (1.36)	7.6 (8.25)	8.3 (40.42)	8.4 (49.97)	8.3	-
3-CH_3	$[Ni(L10)_3H]$	12.0 (9.15)	12.2 (13.99)	12.3 (21.37)	12.7 (55.48)	12.5	-
5-CH_3	$[Ni(L11)_3H]$	12.3 (4.08)	12.0 (1.94)	13.3 (42.03)	13.4 (51.95)	13.3	-
4-CH_3	$[Ni(L12)_3H]$	12.0 (4.52)	12.0 (2.79)	12.7 (13.69)	13.2 (79.00)	13.0	-

Isomers of the protonated intermediate also exist for the complexes with modified ligands. For example, when the PyS^- ligand is modified with EW $-CF_3$ group on C-3 of the pyridyl rings, it forms the **[Ni(L2)$_3$]$^-$** complex. The experimentally observed pK_a of this compound is 8.3, while the calculated weight-averaged pK_a value is 8.4 for all protonated isomers.[32] It has been observed through DFT calculations that the **[R]** isomer is 1.4 kcal/mol, 3.0 kcal/mol, and 2.0 kcal/mol more stable than **[C]**, **[L$_C$]**, and **[L$_R$]** isomers of the protonated intermediates of **[Ni(L2)$_3$]$^-$** complex, respectively. The thermodynamic population analyses of these protonated isomers show that the contribution from **[R]** isomer is 95% while **[C]**, **[L$_C$]**, and **[L$_R$]** forms contribute about 2%, 1%, and 3% towards the equilibrium isomer distribution. When comparing the experimentally observed pK_a value of 5-chloro substituted tris-(pyridinethiolate)nickel(II) complex; **[Ni(L6)]$_3^-$** (7.6) with the weight-averaged calculated pK_a value (9.2), the **[R]** isomer is again the most contributing (72%) followed by **[L$_R$]** (20%), **[C]** (5%), and **[L$_C$]** (3%).[32] The trend remains consistent among the catalysts substituted in the 3- or 5- position; the **[R]** isomer is thermodynamically most stable. As mentioned earlier, when the thiopyridine ring is modified with an ED methyl (CH_3) group or EW trifluoromethyl (CF_3) in the C-6 position, the Ni compounds, **[Ni(L7)$_3$]$^-$**, and **[Ni(L8)$_3$]$^-$**, prefer the fac geometry rather than the mer form as confirmed by both X-ray crystallography and DFT studies (**Appendix Table 2**).[28] This observation hints that structural effects from substitutions at the C-6 position of the ligand is purely guided by steric effects. In the corresponding fac isomer, all the pyridyl N atoms are identical so there is no isomer formation upon protonation, hence not included further in this study.

Most of the calculated pK_a's are within the range of the systematic computational error reported error using B3P86 level of theory of 2.6 pK_a units.[91] However, compounds **[Ni(L4)$_3$]$^-$** and **[Ni(L5)$_3$]$^-$** have computed values outside of this error range, when compared to the experimentally observed values. The calculated structures show close H-O (from the -COOH group) distances, and as we will discuss below, the protonated structures are stabilized by several H-bonds. The pK_a-lowering effect of the stabilizing interaction seen in the computational studies is not observed in the experimentally measured values possibly due to solvent interactions.

Electron donating groups are added to make the catalyst easier to protonate and thus able to operate under more basic conditions. The calculated pK_a values, either taking the weighted average, or considering the most stable isomer show the expected trend (excluding the -COOH derivatives). It also shows position of the substituent is not as important as the electron donating or withdrawing character.

2.3.3 Isomer stability.

To quantify the role of intramolecular H-bonding on isomer formation, we used topology analyses based on QTAIM. Originally, we hypothesized that the thiolate S atom would be a better trans-directing ligand than the pyridyl N atom, due to the higher π-acidic character, a weaker N-Ni bond would result for the N trans to the S, resulting in the highest pK_a for the **[C]** isomer. The calculated N-Ni bond lengths support this theory with the N**[C]**-Ni bond being consistently 0.02 Å longer than both the N**[L]**-Ni and N**[R]**-Ni bonds as observed in the crystal structure data (**Appendix Table 3** and **Appendix Table 4**). If this

were the main contributor to the thermodynamics of the protonated isomer, the protonation would always take place on the N**[C]** atom as it is the only N atom trans to a S atom. However, computations show that the **[C]** isomer is the least thermodynamically favored for all of the protonated derivatives (**Table 2-1**). Thus, we performed QTAIM based topology analysis to investigate additional factors controlling basicity of the different pyridyl N atoms.

The thermodynamic stability for each of the isomers of the **1-H** intermediates is different (**Table 2-1**). QTAIM reveals that, after protonation of $\mathbf{1}^-$, the newly introduced H^+ attached to the pyridyl N atom forms a H-bond with one of the chelating S atoms from the adjacent PyS^- ligands resulting in a distorted square pyramidal structure (**Figure 2-4**, **Appendix Figure 1-10**). We calculated the energy for these intramolecular H-bonding interactions (**Table 2-2**), and found the energy is directly related to the thermodynamic stability of the protonated intermediates, i.e., the higher the energy of the H-bond, the higher is the relative population of the isomer. Intramolecular H-bonding overcomes the thermodynamic trans effect in most cases. It is for this reason; we hypothesize that the formation of a stronger intramolecular H-bond is the key parameter for the protonation of a specific pyridyl N atom and not the trans effect imparted by the thiolate S atoms.

Table 2-2. Topology analysis of the H-bonds in the **1-H** structures for each isomer and the corresponding H-bond strength.

Complex	**Calculated H-bond energies [H (r_{bcp}) *kcal/mol*] in implicit water solvation**			
	[C]	**[L_C]**	**[L_R]**	**[R]**
[Ni(L1)$_3$H]	-6.32	-5.99	-7.36	-7.39
[Ni(L2)$_3$H]	-6.28	-5.94	-7.23	-7.19
[Ni(L3)$_3$H]	-6.47	-6.30	-7.34	-7.28
[Ni(L4)$_3$H]	-6.24	-6.27	-7.10	-7.06

[Ni(L5)$_3$H]	-6.42	-5.95	-7.12	-7.12
[Ni(L6)$_3$H]	-6.74	-6.63	-7.60	-7.62
[Ni(L9)$_3$H]	-6.40	-6.30	-7.33	-7.38
[Ni(L10)$_3$H]	-6.12	-6.09	-7.30	-7.23
[Ni(L11)$_3$H]	-6.40	-6.08	-7.42	-7.42
[Ni(L12)$_3$H]	-6.06	-6.06	-7.25	-7.29

The intramolecular H-bonds have energies ranging from -5.95 kcal/mol to -7.60 kcal/mol. The topology analysis further reveals a bonding interaction between the introduced electron-poor proton and the electron-rich chelating S atoms characterized by the presence of a (3,-1) critical point, or a so-called bond critical point (BCP). For example, in the case of **[Ni(L1)$_3$H]**, **[R]** is the most stable protonated isomer with the highest intramolecular H-bond stabilization energy of -7.39 kcal/mol, while the least stable **[L$_C$]** isomer has the lowest stabilization energy of -5.99 kcal/mol. The stabilization energy of these intramolecular H-bonds is thus correlated with the stability of the protonated intermediates and the stability of different isomers. But there are some outliers: in some cases, the **[L$_R$]** isomer is characterized by a higher H-bond energy than the **[R]** isomer (0.0 – 0.5 kcal/mol) even though the **[R]** isomers are consistently the highest contributor to the equilibrium geometry of the protonated intermediates, as revealed by the Boltzmann distribution analyses. These inconsistencies can be attributed to the electronic effects of the ligand substituents as well as their positions. These modifications lead to the alteration of the electron density on the chelating thiolate S atoms hence further effects on the strength of the said H-bonds. We speculate that the formation of additional H-bonds explains why we observe negative values for calculated pK_a's in the case of protonated **[Ni(L5)$_3$]$^-$**. Therefore, due to the strong intermolecular H-bonds in the starting structure of the catalyst,

it is thermodynamically unfavorable to protonate the **[Ni(L5)$_3$]$^-$** complex. However, under experimental conditions these H-bonds are likely disrupted by solvent interactions.

To further comment on the nature and origin of the intramolecular H-bonds in question, it is well-understood that these interactions are extremely dynamic, and we did not incorporate the effect from intermolecular H-bonding in our modeling of the isomer structures. The experimental verification of these H-bonds through NMR spectroscopic methods is restricted due to the paramagnetic *triplet* spin state of the transition metal and studying the evolution of the system using molecular dynamics simulation while employing an explicit solvent model is computationally expensive. However, this simplistic model describes the available experimentally observed results and provides logical consistency without further expensive and complicated computational treatment.

*2.3.4 Reduction of **[Ni(PyS)$_3$H]** catalysts.*

The next step in the catalytic cycle is a reduction of the protonated catalyst. We expected to obtain *four* different isomers of the reduced intermediates (**1-H$^-$**) when we computationally modelled the second step of the catalytic cycle (the reduction of **1-H**). The **[C] 1-H** isomer was expected to reduce to the **[C] 1-H$^-$** isomer, while the **[L$_C$] 1-H**, **[L$_R$] 1-H**, and **[R] 1-H** were expected to reduce to **[L$_C$] 1-H$^-$**, **[L$_C$] 1-H$^-$**, and **[R] 1-H$^-$** isomers, respectively. Thus, we optimized the structure of each protonated isomer with an extra electron at a *doublet* spin state to model the reduction step of the catalytic cycle employing an implicit solvent model for acetonitrile.

Table 2-3. Topology analysis of the H-bonds in the 1-H$^-$ structures for each isomer and the corresponding H-bond strength.

Complex	**Calculated H-bond energies [H (r_{bcp}) *kcal/mol*] in implicit acetonitrile solvation**

	[C]	[L_C]	[L_R]	[R]
[Ni(L1)$_3$H]$^-$	-6.06	-6.39	-6.49	-6.06
[Ni(L2)$_3$H]$^-$	-6.08	-6.25	-6.59	-5.90
[Ni(L3)$_3$H]$^-$	-6.23	-6.43	-6.71	-6.26
[Ni(L4)$_3$H]$^-$	-5.96	-6.23	-6.47	-5.96
[Ni(L5)$_3$H]$^-$	-5.80	-6.12	-6.54	-5.78
[Ni(L6)$_3$H]$^-$	-6.53	-6.86	-6.98	-6.53
[Ni(L9)$_3$H]$^-$	-6.27	-6.53	-6.75	-6.27
[Ni(L10)$_3$H]$^-$	-5.85	-6.25	-6.41	-5.85
[Ni(L11)$_3$H]$^-$	-6.06	-6.33	-6.43	-6.06
[Ni(L12)$_3$H]$^-$	-5.92	-6.30	-6.35	-5.92

Topological analysis was performed on all possible reduced isomers to examine the intramolecular H-bonds between the H^+ introduced in the first step of the catalytic cycle and the thiolate S atoms of the adjacent PyS^- ligands (**Table 2-3**) (**Appendix Figure 11-20**). We calculated the bond energies of these intramolecular H-bonds using QTAIM for the reduced intermediates, as before. In almost all cases, we unexpectedly observed that the most stable isomers form the least stable H-bonds. For example, the **[C]** and **[R]** isomers of reduced **[Ni(L1)$_3$H]$^-$** are shown to have the highest Boltzmann populations of about 44% each, while the **[L_C]**, and **[L_R]** isomers contribute only 8% and 4% towards the overall population distribution, respectively, based on calculated thermodynamic data. On the other hand, QTAIM results suggest that the intramolecular H-bond in the **[C]** and **[R]** isomer is about 0.33 *kcal/mol* and 0.43 *kcal/mol* less stable than the H-bonds in **[L_C]**, and **[L_R]** isomers. Thus, unlike the protonated intermediates, the stability of the reduced compound is not correlated with the H-bond formed from the protonated pyridyl N. These observations led us to examine the bond characteristics of the reduced isomers between the central metal ion and ligand framework. After considering the central bonds of the reduced complexes, we observed that in most cases the penta-coordinated reduced isomers form either square pyramidal (*sq. py.*) or trigonal bipyramidal (t_bp) complexes. More

importantly, *tbp* intermediates are always formed in pairs, in this case the **[C]** and **[R]** isomers of the reduced complexes, where one form is the enantiomer of the other with the same thermodynamic energy, stability, and thus same extent of intramolecular H-bonding between the H atom attached to the pyridyl N and thiolate S atom from the adjacent PyS^- ligand. Thus, after the reduction step the overall number of isomers decreases.

To classify the structures as *sq. py.* or *tbp*, we calculated the *structure index parameter*, tau (τ), for the DFT optimized penta-coordinated intermediates as introduced by Addison *et al.* using **eqn. 9** (**Figure 2-5**).[92,93] This structure index parameter allows for quantification of the extent of *sq. py.* or *tbp* geometry. The calculated τ values (**Table 2-4**) for the reduced isomers further validate the argument of the formation of two different types of structural isomers upon reduction.

$$\tau = \frac{\beta - \alpha}{60} \tag{2.8}$$

The formation of the two structural isomers also justifies the two contradictory observations obtained from Boltzmann distribution analyses and QTAIM. Since the crystal

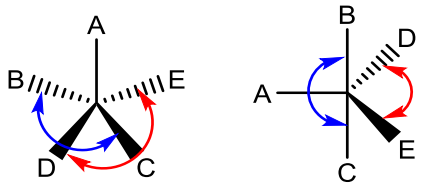

Figure 2-5. The key angles used to calculate the structure index parameter τ for sq. py. and tbp structures: β and α are the largest basal angles. For an ideal tbp, β = 180º, α = 120º, and thus τ = 1; ideal sq. py., $\beta = \alpha$ = 180º, so τ = 0.

field stabilization energy of a *tbp* is more than the *sq. py.* analogue, the Boltzmann population of the *tbp* is higher than the *sq. py.*. However, the degrees of freedom in a *sq. py.*

complex is more than that of its t_bp analogue due to its higher symmetry, which allows the former to create a more stable intramolecular H-bond; hence, the extent of stabilization through H-bonding does not correlate with the overall stability of the reduced compounds.

Table 2-4. Structure index parameter (τ) for the penta-coordinated reduced intermediates.

	τ [C]	τ [L_C]	τ [L_R]	τ [R]
[Ni(L1)$_3$H]$^-$	0.8	0.2	0.2	0.8
[Ni(L2)$_3$H]$^-$	0.8	0.3	0.4	0.7
[Ni(L3)$_3$H]$^-$	0.8	0.3	0.7	0.7
[Ni(L4)$_3$H]$^-$	0.8	0.2	0.4	0.8
[Ni(L5)$_3$H]$^-$	0.7	0.3	0.6	0.7
[Ni(L6)$_3$H]$^-$	0.8	0.2	0.4	0.8
[Ni(L9)$_3$H]$^-$	0.7	0.3	0.4	0.7
[Ni(L10)$_3$H]$^-$	0.8	0.2	0.3	0.8
[Ni(L11)$_3$H]$^-$	0.8	0.2	0.2	0.8
[Ni(L12)$_3$H]$^-$	0.9	0.2	0.1	0.9

For most of the reduced complexes, two different isomers have equal thermodynamic stabilities and thus the same Boltzmann population. In the case of **[Ni(L1)$_3$H]$^-$** the **[C]** and **[R]** isomers optimize to the same structure. This means that the reduction of the protonated isomers is not as straightforward as we predicted. For two protonated isomers to form the same reduced isomer, the Ni-N and Ni-S bonds must break and form; one of the ligands has to flip. This type of ligand rearrangement has been experimentally observed in labile complexes with donating S atoms.[94–97]

We calculated the E^0 values for each isomer of all the complexes using the concept of theoretical *isodesmic reactions* as given in **eqn. 2.5**. Using the experimental E^0 value for the unsubstituted **[Ni(L1)$_3$]$^-$** of -1.62 V vs SCE[28] as a reference, the computational E^0 values for each isomer of each catalyst was calculated. The reference reaction accounts for

solvent, electrode effects, and systematic computational errors. The reported accuracy of calculated E^0 values using an *isodesmic reaction* is *ca.* 0.1 V. We do not see a reasonable correlation between calculated and experimental E^0 values although the calculated trends match what we would expect for the substitutions. For example, the experimentally reported reduction potential for **[Ni(L2)$_3$H]$^-$** is -1.26 V vs SCE,[32] compared to the calculated values of -1.41 to -1.49 V vs SCE. We do not currently have a good explanation as to why computed and measured E^0 values are inconsistent. The use of *isodesmic reactions* heavily relies on intermolecular electron transfer between like species and does not account for the bond breaking and new bond formation. Structural changes upon reduction was observed in the optimization that suggests fluxional behavior of the catalyst may result in bond making and breaking which would account for the poor correlation.

Table 2-5. The calculated E^0 values for each isomer are presented with the thermodynamic Boltzmann distribution of the isomers at room temperature and the experimental E^0 values.

Group	**Complex**	**Calculated Reduction Potential (V vs. SCE) in acetonitrile solvent model (% Distribution)**			
		[C]	**[L_C]**	**[L_R]**	**[R]**
-	[Ni(L1)$_3$H]$^-$	(44.29)	(8.39)	(3.72)	(43.59)
3-CF$_3$	[Ni(L2)$_3$H]$^-$	-1.44 (49.02)	-1.44 (7.12)	-1.41 (5.77)	-1.49 (38.09)
5-CF$_3$	[Ni(L3)$_3$H]$^-$	-1.40 (23.57)	-1.41 (5.45)	-1.37 (5.22)	-1.41 (65.76)
6-S-3-COOH	[Ni(L4)$_3$H]$^-$	-1.38 (47.93)	-1.44 (0.99)	-1.37 (4.11)	-1.40 (46.97)
2-S-3-COOH	[Ni(L5)$_3$H]$^-$	-1.57 (8.53)	-1.59 (0.38)	-1.55 (1.82)	-1.51 (89.28)
5-Cl	[Ni(L6)$_3$H]$^-$	-1.48 (46.89)	-1.59 (0.18)	-1.47 (5.99)	-1.49 (46.94)
4-CF$_3$	[Ni(L9)$_3$H]$^-$	-1.70 (38.37)	-1.72 (11.07)	-1.65 (12.60)	-1.69 (37.97)
3-CH$_3$	[Ni(L10)$_3$H]$^-$	-1.70 (38.37)	-1.72 (11.07)	-1.65 (12.60)	-1.69 (37.97)
5-CH$_3$	[Ni(L11)$_3$H]$^-$	-1.65 (45.07)	-1.65 (8.54)	-1.68 (1.70)	-1.65 (44.69)
4-CH$_3$	[Ni(L12)$_3$H]$^-$	-1.67 (38.03)	-1.67 (15.78)	-1.66 (4.92)	-1.69 (41.27)

Furthermore, since the use of *isodesmic reactions* calculates E^0 by the relative difference in theoretically obtained Gibbs energy values for two similar systems, the choice of the isomers in the reaction will affect the results. Although we speculate that the measured E^0 values results from reduction of the most stable protonated isomer (**Table 2-3** and **Table 2-5**), we cannot be certain which reduced product is ultimately formed. The uncertainty regarding the structure of the final reduced compound is exacerbated by the possibility that isomerization to a thermodynamically more stable compound could occur either before or after the reduction step. However, the computational E^0 values track well with our original expectation of ED groups will make the E^0 values more negative while EW groups will make the E^0 values less negative when comparing with the experimental E^0 value of **[Ni(L1)$_3$H]/ [Ni(L1)$_3$H]$^-$** couple, -1.62 *V vs SCE*.

2.4 Conclusion

This work identifies the impact of electronic and geometric ligand features on the basicity of proton reduction catalysts through an exploration of structural isomers formed by protonation of **[Ni(PyS)$_3$]$^-$** type catalysts. The octahedral meridional geometry of the catalyst results in the formation of geometric isomers upon protonation. The formation of isomers depends on which pyridyl N atom is protonated and also the intramolecular H-bonding network between the proton and the S atom from one of the adjacent PyS$^-$ ligands. This results in differences in the computed pK_a values for each isomer by ~3 pK_a units. The basicity is largely dictated by intramolecular H-bonding with neighboring ligands, which is reminiscent of H-bonding effects observed in proteins and other supramolecular structures. In the first reduction step of the proposed catalytic cycle, the catalysts optimize

to either a *sq. py.* or t_bp geometry, often with two of the isomers optimizing to the same energy and structure. The t_bp geometry rather than the intramolecular H-bond strength was found to determine the most stable reduced isomer. Combining these findings with previously published investigations we have updated proposed catalytic cycle to reflect the most thermodynamically stable structures (**Figure 2-6**).[29]

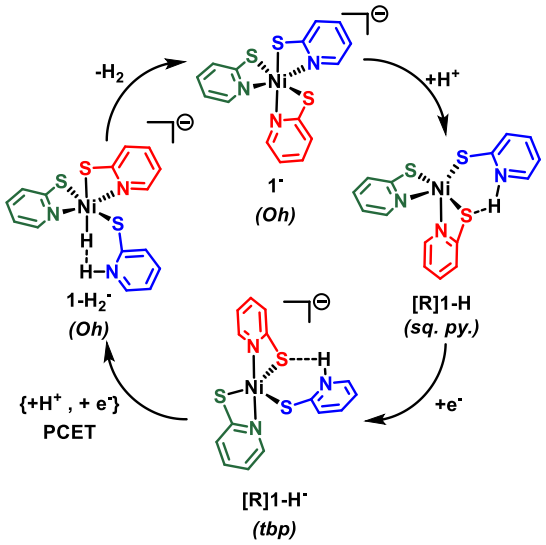

Figure 2-6. Updated catalytic cycle that depicts the most stable isomers for each step in the proposed mechanism.

This work demonstrates the importance of considering structural isomers when computationally modelling catalytic cycles. The unexpected H-bonding in these structures drastically influences the calculated and measured pK_a values of homogeneous metal catalysts by orders of magnitude which is under-estimated by the simple electronic substitutions. The use of intramolecular H-bonding strength as a descriptor of acidity or basicity (pK_a) is often neglected in small-molecular transition metal catalysis. This report also shows that the extent of H-bonding can possibly overcome the thermodynamic *trans*

effect, which is of great interest in the field of catalyst design and reactivity. This demonstrates the importance of carefully considering all electronic and structural modifications aimed at tuning the catalytic activity.

Chapter 3 Computational Investigation into Heteroleptic Nickel(II) Tris-Pyridinethiolate Catalysts for Proton Reduction

This work has been submitted to the *ACS Organic & Inorganic Au* through the contributions from Avik Bhattacharjee, Dayalis S. V. Brown, Trent E. Ethridge, Kristine Halvorsen, Alejandra A. Montano, and Dr. Theresa M. McCormick. Dr. McCormick, Avik, and Day designed this project. Trent, Kristine, and Alejandra assisted Avik with the computational studies.

3.1 Introduction

Molecular hydrogen (H_2) is considered to be the fuel of future to address the increasing global energy demand.[18,20] Although H_2 is a non-condensable gas at ambient temperature-pressure condition, with low volume energy density, it has the highest specific energy of combustion of all the chemical fuels. The volume energy density exceeds all batteries and burning H_2 does not lead to carbon-emissions. H_2 can be accessed from the reductive side of the water splitting reaction through the reduction of aqueous protons.[27] As fascinating and simple it might sound, producing molecular H_2 and O_2 from water in an experimental setup is extremely challenging due to the high overpotential associated with the reaction kinetics. It is for this reason, involvement of a suitable catalyst is imperative to lower the overpotential of water splitting in ambient temperature-pressure conditions.[44,45]

Due to lower overpotential for proton reduction, Pt and Pd complexes were most frequently studied as H_2 generation catalysts.[98] However, low abundance and higher cost

of these metals limit the practical implementation of these catalysts, and the interest has been shifted to the research of noble-metal-free catalyst design for water splitting. Transition metal complexes containing Fe, Co, Ni have been proven to be effective for water splitting.[28,46–48,60,61,66,69,78,99] The nickel(II) tris-pyridinethiolate, **[Ni(PyS)$_3$]$^-$**, catalyst has shown high efficiency in both photochemical and electrochemical systems.[28,70]

We have previously shown that H_2 production by **[Ni(PyS)$_3$]$^-$**, (**1$^-$**) follows a chemical-electrochemical-chemical-electrochemical (CECE) mechanism.[29] In the first step of the catalytic cycle one of the three pyridyl N atoms is protonated and dechelates from the Ni(II) ion, to form the protonated intermediate (**1-H**). The next step is an electron transfer to **1-H** to form the reduced intermediate (**1-H$^-$**), followed by a proton coupled electron transfer (PCET) step to form a Ni-hydride intermediate (**1-H$_2^-$**). And finally, two H atoms come close to one another and leaves the system as molecular H_2 gas closing the catalytic cycle (**Figure 3-1**).

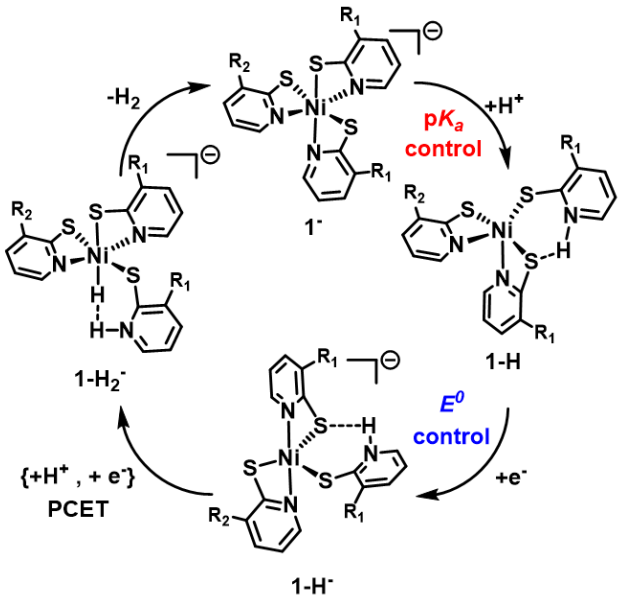

Figure 3-1. Catalytic cycle of H_2 production by heteroleptic Ni(II) tris-pyridinethiolate catalyst (**1**$^-$), where R_1 is either a -CH_3 or -CF_3 while R_2 is either a -CF_3 or -CH_3 group. The first step of the catalytic cycle (protonation of one of the three pyridyl N atoms and dechelation) is controlled by the pK_a and the second step (reduction) is controlled by E^0. Protonation step can be optimized by introducing electron donating substituents while reduction can be tuned by installing electron withdrawing groups on the PyS^- ligand environment.

In the previous chapter, we have shown that the protonation of homoleptic **1**$^-$ leads to the formation of four geometric isomers with different thermodynamic properties and stability due to the different basicities of three pyridyl N atoms owing to the difference in the relative position around the Ni center afforded by the meridional geometry.[100] A topology analysis based on QTAIM on twelve homoleptic Ni(II) tris-pyridinethiolate catalysts supports that an intramolecular hydrogen bonding (H-bonding) interaction between the H^+ on the pyridyl N atom and a S atom from one of the neighboring PyS^- ligands is responsible for the difference in the stabilities and properties of the isomers of protonated and reduced intermediates (**Figure 3-1**). We demonstrated that the H-bonding

strength overcomes the thermodynamic *trans*-effect during the protonation of the catalysts and that these isomers should be considered in computational investigations of these types of catalysts.

We can surmise that the catalytic efficiency of $\mathbf{1}^-$ is correlated with the ease of protonation and reduction. From a thermodynamic standpoint better catalytic activity can be achieved by tuning the pK_a and E^0 of the original catalyst.[32] This can be attained by ligand modification. The pK_a of the catalyst can be increased by incorporating electron donating group (EDG) on PyS^- ligands enhancing the ability of the pyridyl N atoms to be protonated even in higher pH. While, installing electron withdrawing groups (EWG) on the aromatic rings will allow the E^0 value to be less negative signifying the occurrence of a more spontaneous electrochemical step. Though it is necessary to modify the two thermodynamic parameters, pK_a and E^0, to optimize the catalytic activity of $\mathbf{1}^-$, but they cannot be tuned simultaneously in a homoleptic catalyst. In this work, we propose means to simultaneously optimize both pK_a and E^0 through heteroleptic ligand modification of $\mathbf{1}^-$, meaning, installing separate PyS^- ligands with either ED or EW groups on the same complex. We hypothesize that the ligands with EDG will tune the pK_a while that with EWG will optimize the E^0 of the catalysts. To investigate this hypothesis, we have computationally considered the catalytic mechanism of two heteroleptic Ni(II) tris-pyridinethiolate catalysts with 2:1 and 1:2 ratios of electron donating $-CH_3$ and electron withdrawing $-CF_3$ group containing PyS^- ligands and compared the results with the analogous homoleptic complexes (**Figure 3-2**).

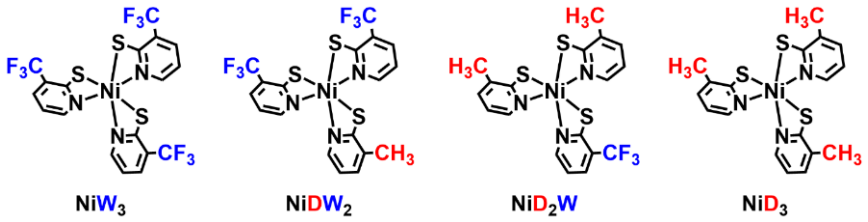

Figure 3-2. The heteroleptic catalysts studied in this work (**NiDW$_2$**, and **NiD$_2$W**) and the analogous homoleptic catalysts (**NiW$_3$**, and **NiD$_3$**) where D and W are the PyS$^-$ ligands containing electron donating -CH$_3$ and electron withdrawing -CF$_3$ groups at C-3 positions, respectively.

While modeling the heteroleptic starting catalysts (**NiDW$_2$**, and **NiD$_2$W**) the possibility of isomer formation was considered based on the location of the unique ligand (ligand with stoichiometric ratio of one), and protonation of the pyridyl N of the D (electron donating) ligands generated a large number of protonated isomers. However, modeling the reduction step was considered only for the most thermodynamically stable protonated isomers. The Ni-hydride intermediates formed after the proton-coupled electron transfer (PCET) step was modeled to gain insight on the relationship between the metal-hydride bond strength and electronic properties of the surrounding PyS$^-$ ligands. DFT calculations assisted by topology analyses using QTAIM reveals ideal configuration of the water-splitting heteroleptic **[Ni(PyS)$_3$]$^-$** is to have one D ligand controlling the protonation step while two W ligands lowering the overpotential for reduction. The systematic approach of fine-tuning the catalytic efficiency of a well-known proton reduction catalyst through heteroleptic ligand modification described herein, provides a novel strategy to optimize photocatalytic system components, and can also be extrapolated to other related catalytic systems. The results described here marks the importance of considering the formation of the isomers to support an explanation for unanticipated results while performing molecular

modeling on structurally similar molecules in order to understand the mechanism in a greater detail.

3.2 Computational Methods

The Density Functional Theory (DFT) calculations were performed using the quantum chemistry package Gaussian09 suite of programs.[80] The geometry optimization of the catalysts and catalytic intermediates were done using B3P86 functionals with 6-311+G(d,p) basis sets employing implicit water and acetonitrile solvation models. The frequency calculations were performed on the stationary points to extract the thermochemical energies. Gibbs energy for each intermediate were obtained using the sum of thermal and electronic energies resulted from the normal mode frequency analyses.

The pK_a values were calculated by **eqn. 3.1** using standard temperature and pressure conditions (298.15 K, 1 atm). The parametric value of the Gibbs energy of a water solvated proton (-264 kcal mol^{-1}) was used to calculate the free energy change of the protonation step as described by **eqn. 3.2**.[30,55,81–83]

$$pK_a = -\frac{\Delta G^0_{rxn}}{RT \ln 10} \tag{3.1}$$

$$\Delta G^0_{rxn} = G_{[R]1-H} - (G_{1-} - 264) \tag{3.2}$$

The reduction potential (E^0) values were calculated using the principle of isodesmic reaction. The experimental reduction potential of the parent **[Ni(PyS)$_3$]H**/**[Ni(PyS)$_3$]H$^-$** couple of -1.62 V *vs.* SCE was used as a reference ($E_{ref}{}^0$) in **eqn. 3.3**.[32]

$$E^0 = -\frac{\Delta G^0}{F} + E^0_{ref} \quad (3.3)$$

The relative population (x) of the protonated isomers were calculated employing the Boltzmann population distribution formula (**eqn. 3.4**) at 298.15 K and normalized to unity with respect to the most stable isomer, assuming the population was only determined by the thermodynamic stability.[101]

$$x = \frac{\exp(-{}^{\Delta G^o_i}/_{RT})}{\sum_i \exp(-{}^{\Delta G^0_i}/_{RT})} \quad (3.4)$$

The structural parameters such as bond lengths and bond angles of the optimized structures of the catalytic intermediates were determined using the GaussView 5.0 visualization software.[102]

The intramolecular H-bonds were investigated through the topological analysis of the electron density distribution using Quantum Theory of Atoms and Molecules (QTAIM).[85,86,103] Wavefunction files of the optimized structures generated by Gaussian09 were analyzed using Multiwfn 3.7 package.[87] The bond energies of the H-bonds (*BE* in kcal mol^{-1}) were calculated from the electron densities (ρ) at the bond critical points (BCP) employing **eqn. 3.5**.[89,90]

$$BE \approx -223.08 \times \rho + 0.7423 \quad (3.5)$$

3.3 Results and Discussion

3.3.1 Isomers of the heteroleptic starting catalysts.

The unsubstituted homoleptic Ni(II) tris-pyridinethiolate catalyst adopts a pseudo-octahedral geometry where the three bi-dentate PyS^- ligands are oriented in a meridional (mer) fashion around the Ni(II) center.[100] This geometry is supported by the X-ray crystallography.[70] The computational modeling of these compounds in both mer and fac configurations shows corresponding mer isomers are lower in energy. The mer geometry results in different chemical environments and thus different basicities of the three pyridyl N atoms owing to difference in their relative position. We have developed a scheme and naming convention to distinguish between the N atoms based on considering an imaginary meridional plane containing the three pyridinethiolate S atoms (**Figure 3-3**). The N atom contained by the plane of S atoms is **N[C]**, and the N atoms to the right and left side of the plane are **N[R]** and **N[L]**, respectively.

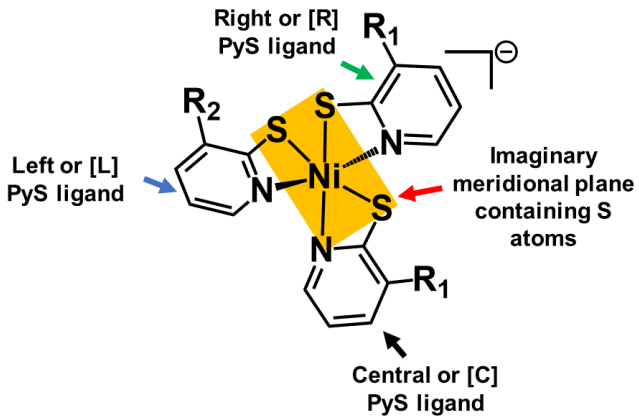

Figure 3-3. Identifying the different pyridyl N atoms based on their relative position with respect to the imaginary meridional plane containing the three S atoms (yellow plane), where R_1 is either a $-CH_3$ or $-CF_3$ group and R_2 is either a $-CF_3$ or $-CH_3$ group. The meridional plane contains **[C]** N atom, while **[L]** and **[R]** N atoms are to the

left and right side of the plane, respectively. The position of the unique ligand with respect to the meridional plane determines the identity of the isomer of the catalyst. The PyS^- ligand containing R_2 group is placed on the left side of the meridional plane making it an **[L]** isomer.

DFT calculations on the heteroleptic **NiDW₂** and **NiD₂W** has revealed that *mer* orientation of the ligands around the Ni(II) center is preferred thermodynamically over the *fac* isomers, similar to the homoleptic compounds. But unlike the homoleptic complexes, three isomers of the starting catalysts are possible for each heteroleptic compound based on the position of the unique ligand prior to protonation. This is because the unique ligand can be introduced to any of the three PyS^- ligands. For example, heteroleptic **NiDW₂** contains **W** (electron withdrawing) ligands with EW $-CF_3$ groups and D ligand with ED $-CH_3$ group in a ratio of 2:1. Hence, in case of **NiDW₂**, D ligand is the unique ligand and the position of D ligand relative to the meridional plane of S atoms outlined above, will dictate the name of the isomer. If the D ligand is in the center and contained within the plane of the S atoms, the isomer will be called **[C] NiDW₂**, and if the D ligand is placed on the right or left side of the imaginary plane of S atoms, it will be called **[R] NiDW₂** or **[L] NiDW₂**, respectively (**Figure 3-4a**). Similarly, in case of **NiD₂W**, the unique ligand is W (a PyS^- ligand containing EW $-CF_3$ group), hence the position of the W ligand with respect to the meridional plane containing three S atoms will dictate the names of the isomers, such as, **[C] NiD₂W**, **[L] NiD₂W**, and **[R] NiD₂W** when W ligand is placed on, to the left side, and to the right side of the plane, respectively (**Figure 3-4b**).

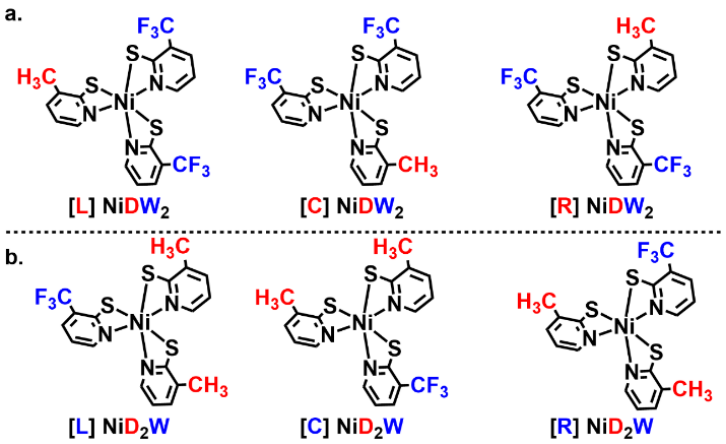

Figure 3-4. Possible isomers of the starting catalysts based on the relative position of the unique ligands in case of heteroleptic complexes.

Boltzmann population distribution of these isomers were calculated from the optimized geometries using the thermodynamic energies and as anticipated the contribution from each isomer is ~33% (**Table 3-1**). The uniform population distribution of these isomers suggest that the thermodynamic properties and stabilities of these complexes are very similar. Hence, when synthesized, it is reasonable to expect an equimolar mixture of the three isomers.

Table 3-1. Calculated Boltzmann population distribution (% x) of the isomers of the starting heteroleptic catalysts at room temperature.

Heteroleptic complex	Isomer of the starting catalyst	Boltzmann population (% *x*)
$NiDW_2$	[C]	33.9
	[L]	34.5
	[R]	31.6
NiD_2W	[C]	34.0
	[L]	33.7
	[R]	32.3

3.3.2 Effect of ligand modification on the pK_a.

To investigate the role of ligand modification on the protonation of the catalysts, we have modeled all possible protonated isomers of the heteroleptic **NiDW$_2$**, and **NiD$_2$W** by protonating the pyridyl N atoms of the D ligands, separately. We hypothesize that ED -CH_3 group containing D ligands will be preferentially protonated over EW -CF_3 group containing W thiopyridyl ligands. This was supported by calculating and comparing the Boltzmann populations of D and W protonated ligands. The relative population of the complexes were negligible when protonation of W ligands was considered compared to the most stable isomers generated through the protonation of D ligands (**Appendix Table 5** and **Appendix Table 6**). In the previous chapter, we have shown that the protonation of the pyridyl N atoms are guided by the formation of an intramolecular H-bonding with one of the adjacent thiopyridyl S atoms and not on the thermodynamic trans effect.[100] The stability of the protonated isomers are directly proportional to the H-bond strength. The existence of the similar intramolecular H-bonding interactions was also observed in case of protonated heteroleptic complexes. Hence to justify the difference and population of the protonated heteroleptic isomers the H-bond strengths were calculated from the topology analyses of the electron densities using Bader's QTAIM.

Protonation of **NiDW$_2$** complex. The heteroleptic **NiDW$_2$** catalyst have only one protonation site; at D, the unique ligand. Hence, D ligands of all the three isomers of the starting catalysts: **[C] NiDW$_2$**, **[L] NiDW$_2$**, and **[R] NiDW$_2$** were separately protonated. As mentioned earlier, protonated intermediates involve in an intramolecular H-bonding interaction where the protonated N atom is the H-bond donor and one of the adjacent

thiopyridyl S atom is the H-bond acceptor. That leads to the formation of six possible protonated isomers (**Figure 3-5**). We have named these such that the first letter denotes the location of the unique ligand, the second letter denotes the location of the protonated N, and the third letter denotes the ligand H-bonding to the proton. For example, protonation of **[C] NiDW$_2$** forms: **[CCL] NiDHW$_2$** where, protonated **[C]** pyridyl N atom is the H-bond donor and adjacent **[L]** thiopyridyl S atom is the H-bond acceptor; and **[CCR] NiDHW$_2$** where, protonated **[C]** pyridyl N atom is the H-bond donor and adjacent **[R]** thiopyridyl S atom is the H-bond acceptor. While protonation of **[L] NiDW$_2$** leads to **[LLC] NiDHW$_2$**, and **[LLR] NiDHW$_2$** where, **[L]** pyridyl N atom is the H-bond donor in both cases but **[C]** thiopyridyl S, and **[R]** thiopyridyl S atoms act as H-bond acceptors, respectively. Similarly, in case of protonated isomers **[RRC] NiDHW$_2$**, and **[RRL] NiDHW$_2$** protonated **[R]** pyridyl N is the H-bond donor and **[C]**, and **[L]** thiopyridyl S are H-bond acceptors, respectively.

DFT calculations on these six protonated isomers followed by topology analyses has revealed that, **[CCL]**, and **[CCR]** are the same molecules with the same thermodynamic energies and intramolecular H-bond strength, collectively referred to as, **[C] NiDHW$_2$**. Similarly, protonation of **[R] NiDW$_2$** leads to only one protonated intermediate, as **[RRC]**, and **[RRL]** have the same thermodynamic energies. Conversely, protonation of **[L]** pyridyl N atom of **[L] NiDW$_2$** forms two isomers: **[LLC]**, and **[LLR]** based on the identity of the H-bond acceptor thiopyridyl S atoms. This reduces the total number of the protonated isomers of **NiDHW$_2$** catalyst to four (**Figure 3-6**). Of these four isomers **[R] NiDW$_2$** is the most thermodynamically stable. Based on the thermodynamic

stabilities we calculated the expected population distribution under standard conditions (**Table 3-2**). To investigate the origin of the unequal relative population distribution of the isomers of the protonated **NiDW$_2$** heteroleptic complexes, we used topology analyses. The electron density distribution of the H-bonded network in these isomers using QTAIM enabled us to correlate the strength of these bonds with the relative thermodynamic stabilities (**Table 2-1**). As anticipated, thermodynamically most stable **[R]** isomer of **NiDHW$_2$** (65.2%) forms the strongest intramolecular H-bonded network (-6.51 kcal mol^{-1}), and the least stable **[C]** isomer (3.8%) forms the weakest intramolecular H-bond (-5.14 kcal mol^{-1}) with the neighboring thiopyridyl S atom (**Appendix Figure 21**).

Table 3-2. Comparison of the intramolecular H-bond stabilization energy (kcal mol^{-1}) with the Boltzmann distribution (% x) of the isomers of protonated intermediates for **NiDW$_2$**.

Protonated heteroleptic complex	Isomers	Boltzmann Population (% x)	N - H…S BE (kcal mol-1)
NiDHW2	[C]	3.76	-5.14
	[LLC]	4.73	-5.33
	[LLR]	26.32	-6.44
	[R]	65.19	-6.51

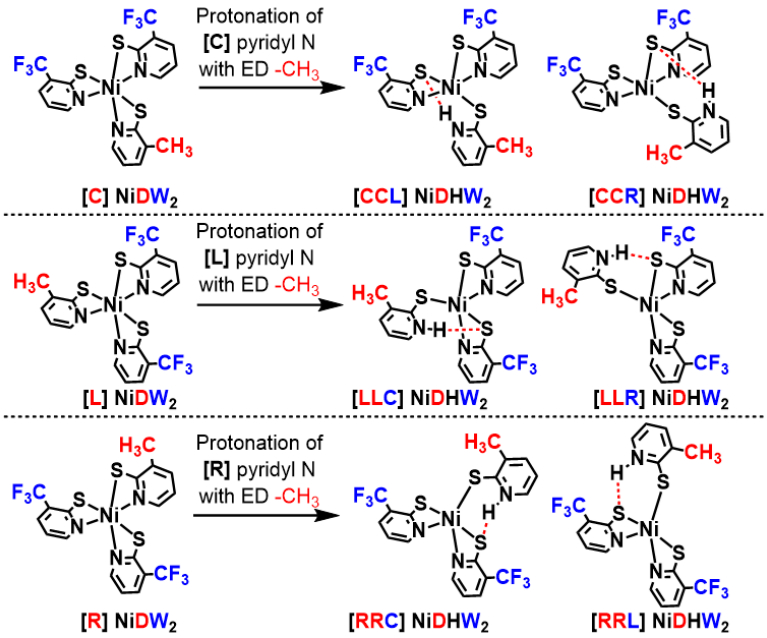

Figure 3-5. Protonation of the unique D ligands of three isomers of **NiDW2** starting catalysts to generate six possible protonated isomers. The intramolecular H-bonding interactions between pyridyl N-H and one of the adjacent thiopyridyl S atoms are shown using red dashed bonds.

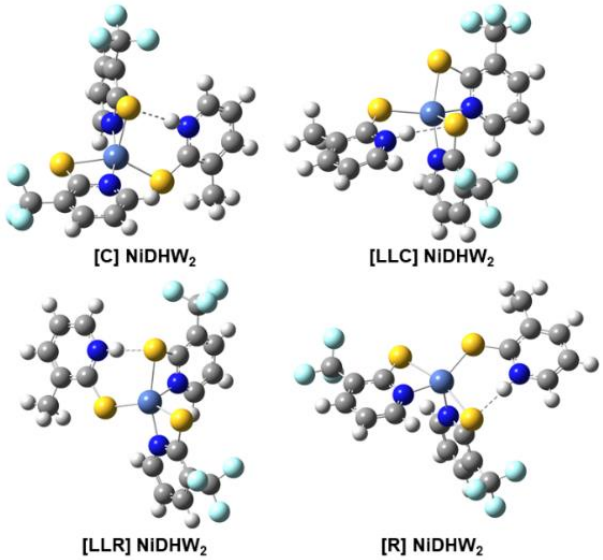

Figure 3-6. Ball and stick structures of the optimized protonated isomers of **NiDHW2** where blue, grey, yellow, white, indigo, and cyan balls represent N, C, S, H, Ni, and F atoms, respectively. The intramolecular H-bonding interactions (N – H…S) are shown using dashed bonds.

3.3.3 Protonation of **NiD_2W** complexes.

The protonation of heteroleptic **NiD_2W** complex is more complicated as it contains more than one ED -CH_3 group containing **D** ligands. We hypothesize that the protonation of **NiD_2W** complex could lead to the formation of up to twelve isomers based on the identity of the protonated **D** ligand and the identity of the H-bonded S atom from one of the adjacent PyS^- ligands (**Scheme 3-2**). All the twelve complexes were modeled using DFT by separately protonating each of the **D** ligands. As observed in case of protonated isomers of **$NiDW_2$**, the isomers of **NiD_2HW** were of different thermodynamic stabilities. The intramolecular H-bonded structures were studied using QTAIM based topology analyses to correlate the strength of H-bonds with the relative population of the isomers (**Figure 3-7**, **Appendix Figure 22**).

Heteroleptic complex	Unique W ligand	Protonated D ligand	S atom of adjacent PyS^- ligand	Protonated isomer
NiD_2HW	[C]	[L]	[C]	[CLC]
			[R]	[CLR]
		[R]	[C]	[CRC]
			[L]	[CRL]
	[L]	[C]	[L]	[LCL]
			[R]	[LCR]
		[R]	[C]	[LRC]
			[L]	[LRL]
	[R]	[C]	[L]	[RCL]
			[R]	[RCR]
		[L]	[C]	[RLC]
			[R]	[RLR]

Scheme 3-1. Nomenclature of the protonated isomers generated from the NiD_2W heteroleptic complexes considering the intramolecular H-bonding network where pyridyl N atom from one of the D ligands acts as a H-bond donor and a S atom from one of the adjacent PyS^- ligands behave as the H-bond acceptor.

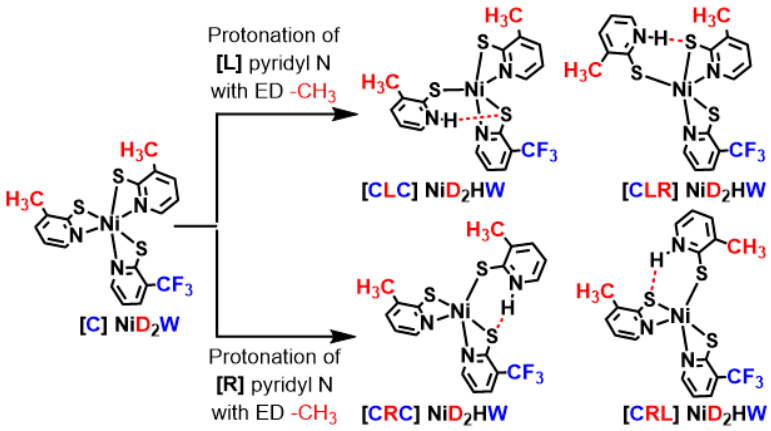

Figure 3-7. Four isomers of **[C] NiD₂HW** complexes considering protonation of both [L] and [R] ligands and intramolecular H-bonded networks with the adjacent PyS^- ligands through the S atoms, separately. The intramolecular H-bonding interactions are shown using red dashed bonds.

The DFT studies supported by QTAIM based topology analyses reveals that protonation of the **D** ligands of three isomers of starting catalysts form eight different isomers instead of originally predicted twelve (**Scheme 3-2**, **Appendix Figure 23**). Isomers are formed as pairs with exactly same thermodynamic stabilities and H-bond strength e.g. **[CRC]** and **[LRL]** are the same molecules; similarly **[CRL]** and **[LRC]**; **[RCL]** and **[LCR]**; and finally, **[RCR]** and **[LCL]** are identical molecules with same thermodynamic energies. However, **[CLC]**, **[CLR]**, **[RLC]**, and **[RLR]** isomers of **NiD₂HW** are unique isomers with no structural conjugates. In summary, protonation of **[L]** isomer of the starting **NiD₂W** catalyst leads to four isomers which are structurally identical to four other isomers formed through protonation of either **[C]** or **[R]**. Hence further on, the only eight isomers formed by protonation of **[C]** and **[R]** isomers of **NiD₂WH** will be discussed and will be referred to as: **[CLC]**, **[CLR]**, **[CRC]**, **[CRL]**, **[RCL]**, **[RCR]**, **[RLC]**, and **[RLR]**. These isomers vary in terms of their relative population. The Boltzmann populations were compared with the intramolecular N-H…S H-bond strengths

(**Table 3-3**). These results deviated somewhat from the original hypothesis that the unequal population distribution can be explained solely based on the strength of these intramolecular H-bonds. For example, the most stable **[CRL]** protonated isomer (49.4%) has lower H-bond stabilization (-6.97 kcal mol^{-1}) when compared to the **[CRC]** isomer (-7.48 kcal mol^{-1}) which has a lower Boltzmann population (20.4%). However, when these H-bonds strengths were plotted against the quantum mechanically derived single point energies an overall linear correlation was observed (**Appendix Figure 24**).

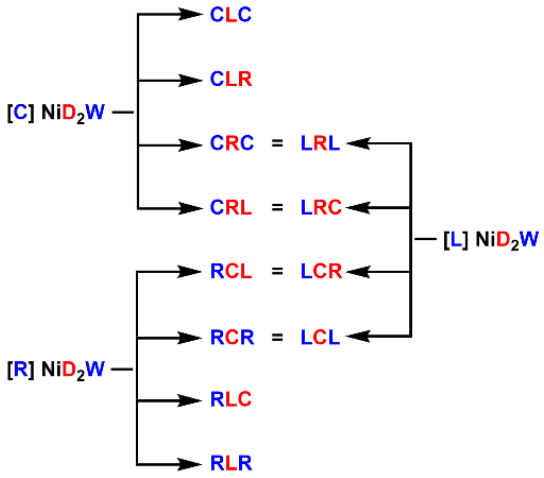

Scheme 3-2. Protonation of three starting isomers of **NiD_2W** catalysts produces eight isomers instead of originally proposed twelve isomers.

Table 3-3. Comparison of the intramolecular H-bond stabilization energy (kcal mol^{-1}) with the Boltzmann distribution (% x) of the isomers of protonated intermediates for **NiD_2W**.

Protonated heteroleptic complex	Isomers	Boltzmann Population (% x)	N - H…S BE (kcal mol^{-1})
NiD_2HW	[CLC]	2.51	-5.19
	[CLR]	7.94	-7.02
	[CRC]	20.36	-7.48
	[CRL]	49.42	-6.97
	[RCL]	8.27	-5.81
	[RCR]	0.72	-5.82
	[RLC]	2.51	-5.66

	[RLR]	8.27	-6.60

In order to further refine the hypothesis to justify the unequal Boltzmann distribution of the protonated intermediates a closer inspection of the metal-ligand framework was performed. The penta-coordinated square pyramidal protonated isomers can be broadly classified into two categories: (a) S atom capped square pyramids, and (b) N atom capped square pyramids. N-capped square pyramids were consistently thermodynamically more stable when compared with the S-capped square pyramids (**Figure 3-8**). This can possibly be attributed to a lower steric interaction between the bulky S atoms in the N-capped square pyramidal configuration. Thus, the stability trends with the structural differences in these complexes, which will dictate the calculated pK_a values.

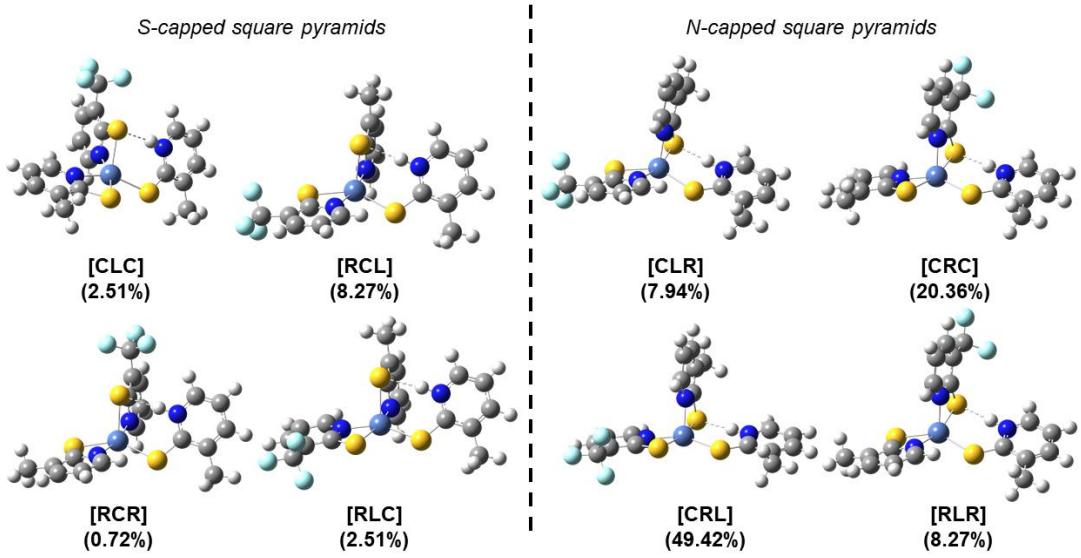

Figure 3-8. Ball and stick structures of the optimized protonated isomers of **NiD$_2$HW** including relative Boltzmann populations, classified in two groups: S-capped and N-capped square pyramidal complexes. The blue, grey, yellow, white, indigo, and cyan balls represent N, C, S, H, Ni, F atoms, respectively. The intramolecular H-bonding interactions (N-H…S) are shown using dashed bonds.

3.3.4 pK_a values of the complexes.

The pK_a values of all possible isomers of the protonated complexes were calculated (**Appendix Table 7**). It has been observed that for a single compound the distribution in the pK_a values is 1.3 and 4 pK_a unit for **NiDW₂** and **NiD₂W** complexes, respectively. The calculated pK_a values of the most stable protonated isomers of **NiDHW₂** (**[R]**), and **NiD₂HW** (**[CRL]**) were compared to the homoleptic analogues **NiW₃**, and **NiD₃** catalysts (**Table 3-4**). An increase in the pK_a of the catalysts is observed with increasing the number of electron donating **D** ligands. It is possible to achieve better control over the basicity of the pyridyl N atoms through the incorporation of ED substituents in the ligand framework as hypothesized earlier. The tunability ranges from 8.5 to 12.7 pK_a units with zero to three **D** ligands, respectively and as anticipated the pK_a values of the heteroleptic complexes are intermediate between their homoleptic analogues.

Table 3-4. The calculated pK_a of thermodynamically most stable protonated isomers in implicit water solvation and the calculated E^0 values in an implicit acetonitrile solvation of the reduced isomers of the heteroleptic complexes and comparison with that for the homoleptic analogues at room temperature.

Catalysts	Most stable protonated isomer	Calculated pK_a values	Calculated E^0 V vs SCE
NiW₃	-	8.5	-1.44
NiDW₂	[R]	9.5	-1.40
NiD₂W	[CRL]	11.1	-1.53
NiD₃	-	12.7	-1.69

3.3.5 Effect of ligand modification on E^0.

The reduction step of the most stable protonated isomers was modeled by adding an extra electron to the system in an implicit acetonitrile solvation model. The reduction of **NiDHW₂** leads to the formation of **NiDHW₂⁻**, while reduction of **NiD₂HW** generates

NiD_2HW^- (**Figure 3-9**). The reduction step changes the oxidation state of the central metal ion from +2 to +1. The ligand coordination around the Ni center also changes from a square pyramid to a trigonal bipyramid. The structural changes were investigated by calculating the structure index parameter (τ) value of the metal-ligand framework as introduced by Addison *et al.*, where for an ideal trigonal bipyramid, τ is 1, and an ideal square pyramid τ is 0 (**Appendix Figure 25**).[92,93] In case of the reduced complexes, τ ranges from 0.7 to 0.8 (**Appendix Table 8**) indicating a more trigonal bipyramid structure. The reduction potential values (E^0) were calculated from the Gibbs energy change of these one-electron reduction events using the concept of isodesmic reactions (**Table 3-4**). A balanced reaction is created assuming an internal electron transfer from a reference reduction reaction with a known reduction potential. The reduction potential of unsubstituted (**$[Ni(PyS)_3H]^-$ /$[Ni(PyS)_3H]$**) couple, -1.62 V vs. SCE, was used as the reference value (E^0_{ref}).[32,100]

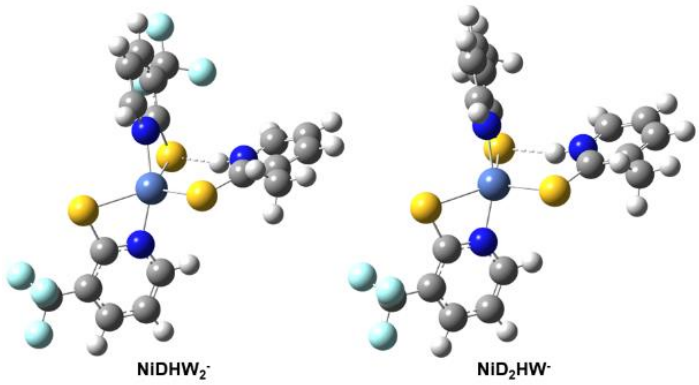

Figure 3-9. Ball and stick structures of the optimized reduced intermediates: **$NiDHW_2^-$**, and **NiD_2HW^-**. The modified PyS^- ligands are oriented in a trigonal bipyramidal fashion around the Ni(I) metal cation. The blue, grey, yellow, white, indigo, and cyan balls represent N, C, S, H, Ni, and F atoms, respectively.

In general, more electron withdrawing ligands results in less negative reduction potentials. When compared with the homoleptic analogue **NiD_3**, the E^0 values of the

heteroleptic catalysts increases to the more positive values with the increase in the EW **W** ligands accounting for a more spontaneous reduction process. However, when **NiW_3** is compared with **$NiDW_2$** the latter is slightly easier to reduce even though the former has more **W** ligands. This can be attributed to the difference in the extent of stabilities of the protonated intermediates of **NiW_3H** and **$NiDHW_2$**. Since the method of calculation of E^0 values using isodesmic reactions utilizes the free energies of both protonated and reduced intermediates and further compares it with the reference reaction of the unsubstituted nickel tris-pyridinethiolate catalysts, the comparison of the free energy change of the reaction is more appropriate than comparing the absolute value of E^0 calculated by the employment of this method.

3.3.6 Effect of ligand modification on the hydride intermediates.

The final step of the catalytic cycle of water splitting using nickel(II) tris-pyridinethiolates is a proton coupled electron transfer (PCET) resulting in a Ni(0)-hydride intermediate.[29] This is modeled by adding a proton and electron to the reduced complex. Consequently, the nickel center regains an octahedral coordination. The hydride attached to Ni(0) and proton on the pyridyl N atom are near each other to allow for a hydrogen molecule to be released forming the original catalyst. The PCET intermediates of the heteroleptic catalysts **$NiDH_2W_2^-$**, and **$NiD_2H_2W^-$** were modeled in acetonitrile implicit solvation (**Figure 3-10**). The structural parameters corresponding to H…H interactions were measured along with the Gibbs energy change for the hydrogen release reactions for the heteroleptic complexes along with their homoleptic analogues (**Table 3-5**).

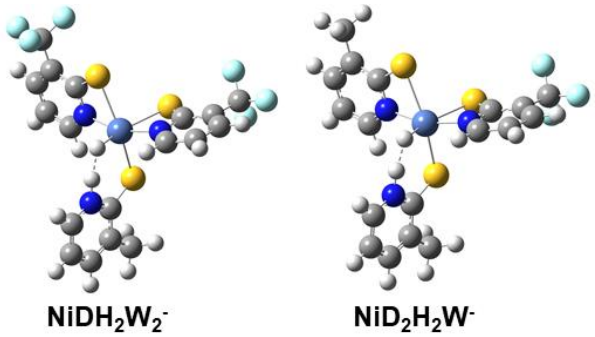

Figure 3-10. Ball and stick structures of the optimized metal-hydride intermediates in acetonitrile implicit solvation: **$NiDH_2W_2^-$**, and **$NiD_2H_2W^-$**. The blue, grey, yellow, white, indigo, and cyan balls represent N, C, S, H, Ni, and F atoms, respectively. The interaction between the two H atoms (H…H) trapped between the Ni and a pyridyl N atom are shown using dashed bonds.

Table 3-5. Structural parameters of the PCET intermediates of the heteroleptic and homoleptic catalysts and the free energy change of the hydrogen release step to regain the original configuration at room temperature.

PCET intermediate	N-H bond length (ang.)	Ni-H bond length (ang.)	H…H bond length (ang.)	Gibbs energy change for H_2 release (kcal mol^{-1})
$NiW_3H_2^-$	1.09	1.64	1.35	-28.7
$NiDH_2W_2^-$	1.07	1.64	1.41	-26.3
$NiD_2H_2W^-$	1.07	1.64	1.40	-25.8
$NiD_3H_2^-$	1.07	1.64	1.40	-26.5

The similarities in the structural parameters of the Ni(0)-hydride intermediates of the homoleptic and heteroleptic complexes indicate that ligand modification has little to no effect on the final two steps of the catalytic cycle of hydrogen production using Ni(II) tris-pyridinethiolates. The free energy change of hydrogen evolution reaction are very similar for all four compounds. This observation indicates that tuning the catalytic efficiency of the proton reduction Ni(II) tris-pyridinethiolate catalysts are appropriately modeled targeting the first two steps of the catalytic cycle. The energetics of the full catalytic cycle was compared for the heteroleptic complexes in acetonitrile solvation model (**Figure 3-11**).

The parametric values of acetonitrile solvated proton (-260.2 kcal mol^{-1}) and electron (-31.9 kcal mol^{-1}) were used to calculate the free energy change of the catalytic steps.[104–107] Protonation of more EDG containing **NiD_2W** is 3.8 kcal mol^{-1} more favorable, while reduction of more EWG containing **$NiDW_2$** is more favorable by 2.9 kcal mol^{-1} in continuum acetonitrile solvation at room temperature. From the calculated thermodynamic energies, it is observed that the Ni(0)-hydride intermediates have similar energies (within 0.3 kcal mol^{-1}). However, since the reduced intermediate of **$NiDW_2$** is more stable than **NiD_2W**, the PCET step of **$NiDW_2$** is less energy demanding than **NiD_2W**. Finally, the hydrogen evolution step requires similar energy for both heteroleptic complexes. Based on these calculations of the thermodynamic parameters, it can be concluded that the ideal combination for the heteroleptic catalyst for proton reduction by Ni(II) tris-pyridinethiolate would be to have one ligand containing electron donating group (**D**) that will tune the pK_a value of the complex and two electron withdrawing ligands (**W**) to tune the E^0 value of the complex toward more positive value leading to a more spontaneous reduction process.

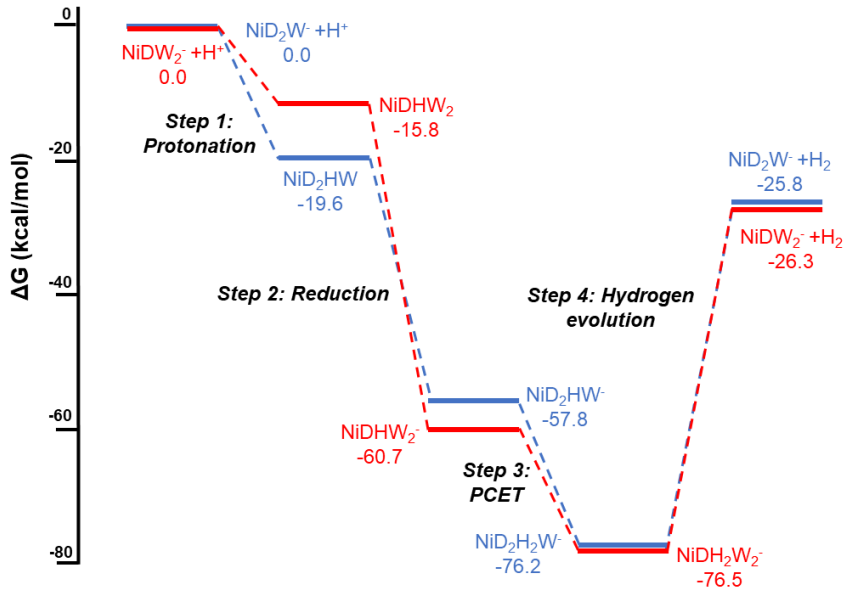

Figure 3-11. Energy profile diagram for the catalytic steps of proton reduction using **NiDW$_2$**, and **NiD$_2$W** heteroleptic complexes. The free energy changes are reported in kcal mol^{-1}. Presence of more **D** ligands accounts for an easier protonation while more **W** ligands makes the reduction step more spontaneous characterized by higher a free energy change. The final two steps (PCET, and H_2 evolution) are characterized by similar free energy changes for both the complexes suggesting that ligand modification does not affect these two steps of the catalytic cycle.

3.4 Conclusion

This work provides computational insight into tuning the catalytic efficiency of proton reduction Ni(II) tris-pyridinethiolate catalysts through heteroleptic ligand design. The previously reported catalytic cycle outlines the role of pK_a, and E^0 that need to be simultaneously optimized in order to tune the catalytic efficiency. Introduction of ED groups accounts for a higher pK_a, however, a less negative E^0 requires EW groups. Since these two properties require two opposing ligand modifications a heteroleptic catalyst containing both ED and EW groups in a single complex can modulate both the thermodynamic properties. To test the hypothesis two heteroleptic complexes **NiDW$_2$**, and

NiD_2W were studied, and the calculated thermodynamic parameters were compared with the corresponding homoleptic analogues (**NiW_3**, and **NiD_3**). DFT calculations along with QTAIM results indicate that the ideal configuration for the heteroleptic catalyst design for water splitting reactions is **$NiDW_2$**, where one ED **D** ligand tunes the pK_a to a higher value and two EW **W** ligands accounting for a more favorable reduction process.

It was observed previously that catalytic mechanism of the homoleptic **$[Ni(PyS)_3]^-$** proceeds through the protonation of one of the pyridyl N atoms. Due to the asymmetric ligand environment around the Ni center, protonation leads to the formation of geometric isomers. The stability of these isomers is related to the strength of an intramolecular H-bonding interaction between the pyridyl N-H and one of the adjacent thiopyridyl S atoms. In case of heteroleptic complexes isomer formation through protonation was also observed and due to higher structural complexity in the heteroleptic complexes, the number of isomers is much higher than its homoleptic analogues. This work demonstrates the importance of carefully accounting for contributions from all the isomers while computationally modelling structurally intricate systems in order to achieve unambiguous and meaningful results. This report also shows that introduction of ED -CH_3 group in the ligand environment of the heteroleptic complexes, systematically increases the pK_a, and increase in EW -CF_3 group make the E^0 approach less negative values when compared with their homoleptic analogues. To summarize, heteroleptic Ni(II) tris-pyridinethiolates are capable of hydrogen production at higher pH with lower overpotential when compared with the homoleptic congeners.

Chapter 4 Photocatalytic Aerobic Oxidation of Benzylic Alcohols And Concomitant Hydrogen Peroxide Production

A provisional patent application has been filed to the United States Patent and Trademark Office based on this work (Application No. 63/336,065). The project was designed by Avik Bhattacharjee and Dr. Theresa M. McCormick. Serena M. Frazee assisted Avik with the synthetic and experimental procedure. Avik conducted the computational studies.

4.1 Introduction

Aerobic oxidation using transition metal compounds is widely used method for transformation of small organic molecules in both laboratory and industrial scale.[26,33,108] However, the major drawbacks of this processes include the production of large amount of toxic waste, the use of heavy metal cocatalysts, and harsh reaction conditions. Photocatalytic and metal-free aerobic oxidation of organic moieties is an emerging field in the area of sustainable chemical research. The use of small organic molecules to activate molecular oxygen has well-known applications in C-H and C-C bond activation reactions.[109–113] These organo-catalysts are desirable due to their high reactivity and tunability and most importantly the access to a greener alternatives. Herein, we report a simple strategy to achieve aerobic oxidation of benzylic alcohols (benzhydrol, and benzyl alcohol) in metal-free and photocatalytic conditions. This process has an added benefit as it allows us to access hydrogen peroxide as the value-added byproduct.

H_2O_2 has widespread use in several laboratory and industrial processes.[3,9,10] It is one of the most important oxidants and has many household uses. Recent reports reveal that H_2O_2 can also act as a sustainable, carbon-neutral fuel in an electrochemical fuel cell, producing only water as the waste material. This has a potential to become the "fuel of the future". Considering only current uses of H_2O_2, reports show that market size is expected to reach USD $6.41 billion by 2028 due to an increase in the global demand of this chemical. In the United States, only a handful of production plants produce the over 4.5 million tons of H_2O_2 that are used every year, which is then shipped to the point of use. The current method of H_2O_2 production utilizes the Anthraquinone Process (AP) that uses H_2 and O_2 and an expensive Pd-catalyst.[38,115] This process requires large chemical production plants and major disadvantages include energy intensive mass-transport limitations of hydrogenation and oxidation steps, and substantial investments for purification, storage, and distribution. Furthermore, the required H_2 gas is produced by steam reforming fossil fuels, producing carbon emissions.[109]

Direct synthesis of H_2O_2 that use H_2 and O_2 have an ideal atom-economy.[116,117] However, mixtures of H_2 and O_2 are explosive at most concentrations, and the majority of catalysts that activate H_2 also activate decomposition of H_2O_2. Dilution of the gas mixture and judicious choice of catalyst have shown some success. However, most systems rely on rare earth metal catalysts such as Ir, Pt or Pd. Thus, it is important to develop catalysts that will allow O_2, preferably from air, to act as the stoichiometric oxidant for the two-electron oxidation of water.[116–120] Traditionally, efforts in developing aerobic oxidation catalysts have used homogeneous transition-metal catalysts. Since our goal is to develop an

oxidation catalyst that can simultaneously oxidize a substrate and produce H_2O_2, reactions must avoid any metals to prevent decomposition.[18,19]

Use of *N*-hydroxyphthalimide (NHPI) as an organic oxidation catalyst has been reported in literature for a variety of substrates, usually under thermal condition, with metal activators.[34–36] The oxidation of benzylic alcohols to corresponding carbonyl compounds have been shown to occur without the over-oxidation that is observed for other alcoholic substrates.[121] Oxidation reactions using NHPI follow a radical mechanism. First, homolytic cleavage of the NO-H bond generates phthalimide-*N*-oxyl (PINO) radical. PINO reacts with the substrates to generate carbon centered radicals that eventually react with O_2 to form a metastable hydroxy (perhydroxy) intermediate. Finally, hydroperoxyl leaves as H_2O_2 generating a carbonyl compound as the final product. However, cobalt and/or manganese co-catalysts are often used to initiate H-atom abstraction for NHPI to produce the active radical species, PINO. Thus, any H_2O_2 produced in these systems decompose under these reaction-conditions and attempts to isolate it have not been reported.[40] Furthermore, thermal reactions require elevated temperatures (70-90 °C) where PINO is prone to decomposition.[122–124] Hence, we are interested in utilizing low-temperature photochemical reactions with no metal co-catalysts such that highly efficient reactions can be developed that will allow both oxidized product and H_2O_2 to be isolated. Photocatalytic oxidation of the α-C of unsaturated hydrocarbons has been reported with NHPI as a radical organocatalyst. In this work, CdS acts as a photo-redox catalyst to generate PINO and to reduce oxygen to superoxide.[125] Similarly, a report by Li *et al*. demonstrated the excited-state of graphitic-carbon-nitride (g-C_3N_4) can activate O_2 to superoxide, which promotes

hydrogen abstraction from NHPI, generating PINO to oxidize toluene.[126] This differs from our proposed reaction mechanism where $^1O_2$ is the reactive-oxygen-species. In a recent paper by Chen *et al.*, Rose Bengal was used as a photosensitizer for the synthesis of β-oxy alcohols.[127] This work indicates that PINO is generated by the sensitized $^1O_2$, however this reaction is not catalytic since PINO is consumed during the reaction.

Production of H_2O_2 from water oxidation and O_2 reduction is desirable because it eliminates the need for explosive gas mixtures, and both water and O_2 are readily available. Coupled to a photochemical reaction, this is a green method for H_2O_2 production. Reports of Ru and Ir photocatalysts show H_2O_2 can be produced from O_2 and water, but these reactions require additives to stabilize the superoxide intermediate or sacrificial electron donors.[25,128,129] Reports by Hirai *et al.* show g-C_3N_4 containing electron-deficient aromatic diimide can convert water to H_2O_2 using O_2, and light.[116,117] By using an alcohol as the electron-sink, H_2O_2 is produced while simultaneously synthesizing a desired product. Our preliminary results indicate that H_2O_2 is produced in the photo-oxidization of alcohols from water and O_2 without metal catalysts. Herein we propose a novel green photocatalytic aerobic oxidation of benzylic alcohols to produce carbonyl compounds which can simultaneously access H_2O_2 as a value-added product (**Scheme 4-1**).

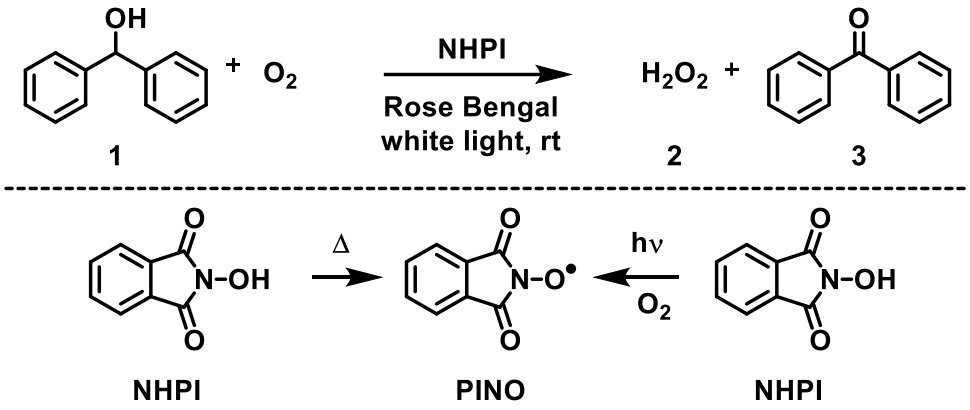

Scheme 4-1. Reaction scheme of diphenylmethanol oxidation (top) and thermal and photochemical production of PINO (bottom).

4.2 Synthetic Methods: Benzylic Alcohol Oxidation

In a previously published report on aerobic oxidation of alcohols to produce H_2O_2, Ishii *et al.* used thermochemical conditions (75 ^{0}C) to afford in-situ generation of the PINO radical to carry out the conversion (**Scheme 4-1**).[40] Herein we report a novel strategy of using visible light to access the oxidation products in comparable yield to the thermal conditions (**Figure 4-1**). 5 mmol Diphenylmethanol (**1**) was reacted with molecular O_2 in presence of NHPI (5 mol%) photocatalyst and a photosensitizer Rose Bengal (RB) in 5 mL acetonitrile (ACN) under white light irradiation at room temperature for 72 hours to afford benzophenone (**3**) and H_2O_2 (**2**) as identified by ^{1}H NMR (**Figure 4-2**). The yield of the photochemical reaction was calculated by ^{1}H NMR by the use of an internal standard (ethylene carbonate). The observed primary yields of benzophenone (**3**) was 70% and that for hydrogen peroxide (**2**) was 50%.

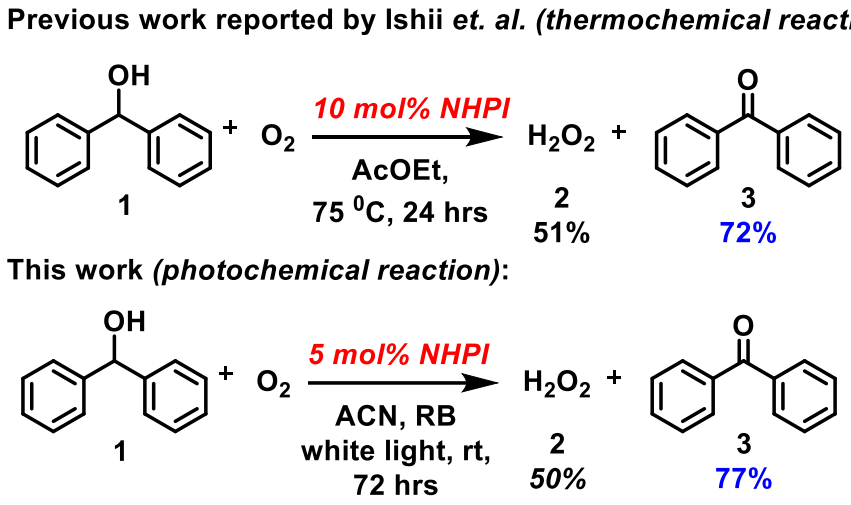

Figure 4-1. Aerobic oxidation of diphenylmethanol (**1**) to hydrogen peroxide (**2**), and benzophenone (**3**) using NHPI organocatalyst in thermal (top) and photochemical (bottom) conditions.

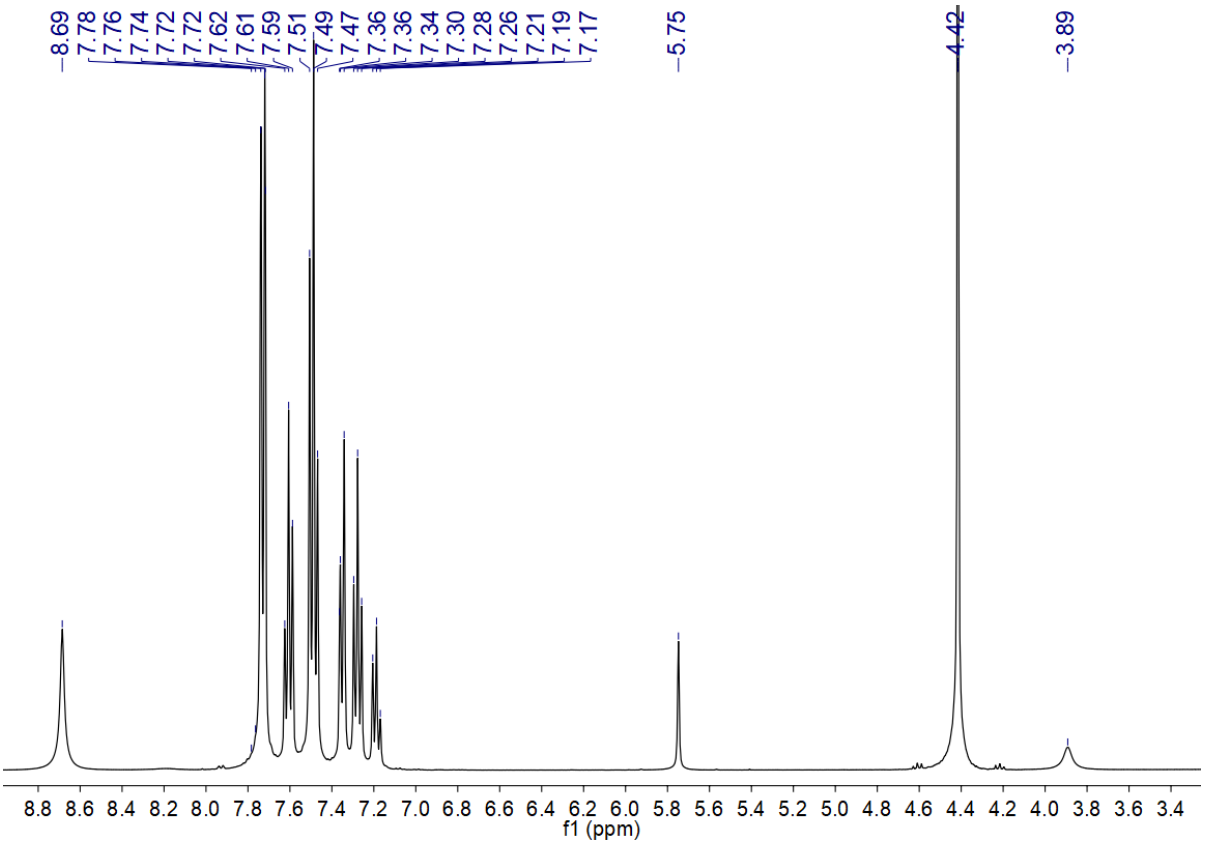

Figure 4-2. ^{1}H NMR spectrum of the reaction mixture taken in CD_3CN at 298 K (400 MHz). Diphenylmethanol: δ = 3.89 (s), 5.75 (s), 7.17-7.21 (t), 7.26-7.30 (t), 7.34-7.36 (d); benzophenone: δ = 7.47-7.51 (t), 7.59-7.62 (t), 7.72-7.78 (d); H_2O_2: δ = 8.69 (s); ethylene carbonate (internal standard): δ = 4.42 (s).

When a primary alcohol, phenylmethanol, was oxidized employing the same reaction conditions a mixture of oxidized products were observed along with H_2O_2 (17%). Phenylmethanol was primarily oxidized to benzaldehyde (23%); however, a trace amount of over-oxidized product, benzoic acid (4%) was also observed (**Figure 4-3**). The overall yield of the oxidation products was lower in case of primary alcohol, which can be attributed to the lesser stability of the benzylic radical due to the lower number of phenyl rings, when compared to the secondary benzylic alcohol, diphenylmethanol.

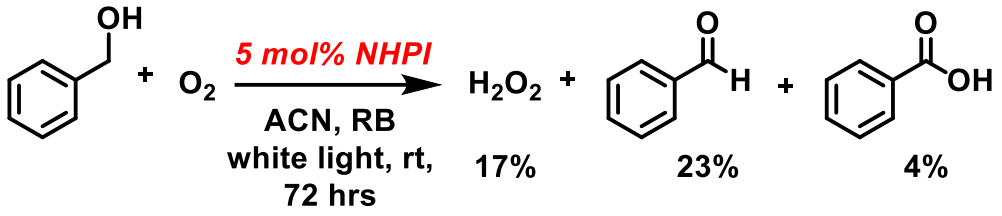

Figure 4-3. Aerobic oxidation of phenylmethanol to hydrogen peroxide, benzaldehyde, and benzoic acid.

To evaluate the effect of each of the components of the reaction we ran a series of control experiments and screened them for the production of H_2O_2 using peroxide test-strips (**Table 4-1**). The positive control reaction (Entry 1) was run using 5 mmol **1**, and 10 mol% NHPI in 5 mL of 10^{-4} M Rose Bengal solution in acetonitrile. The reaction flask was sealed with a balloon filled with oxygen gas. The reaction was stirred vigorously (1500 rpm) for 48 hours while being irradiated under white light. Hydrogen peroxide was separated from the organic layer to the aqueous layer by liquid-liquid extraction with 5 mL toluene and 5 mL of water. A dark blue coloration of the peroxide test-strip indicated the presence of H_2O_2 in the aqueous work-up of the reaction. To rule out the presence of any other types of peroxides or reactive oxygen species (ROS) that might interfere with the peroxide test-strips, we further performed absorption studies with a selective titanium(IV)-porphyrin dye, oxo[5,10,15,20-tetra(4-pyridyl)porphyrinato]titanium (IV), $[TiO(TPyPH_4)]^{4+}$, and compared it with a known concentration of commercial sample of H_2O_2. In presence of H_2O_2 the characteristic absorption peak at 432 nm corresponding to the dye was shifted to 445 nm confirming the presence of $[TiO_2(TPyPH_4)]^{4+}$ complex which is selective to only H_2O_2 and not any other source of peroxide or ROS (**Figure 4-4** and **Figure 4-5**).[130] This indicated the production of hydrogen peroxide in these oxidation

reactions. Thus, a color change on the test strip was used to indicate a positive control for the reactions, and if no hydrogen peroxide was detected we assumed there was no reaction.

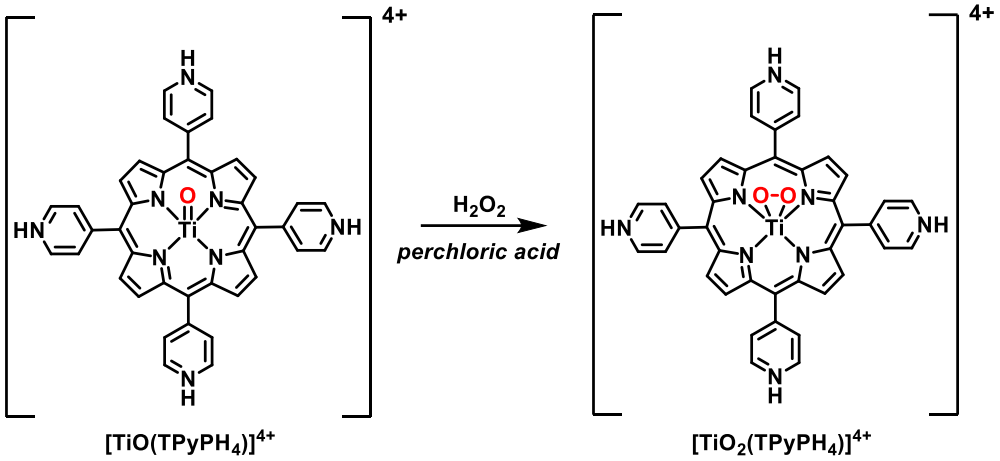

Figure 4-4. Quantitative conversion of $[TiO(TPyPH_4)]^{4+}$ to $[TiO_2(TPyPH_4)]^{4+}$ in presence of hydrogen peroxide and perchloric acid.

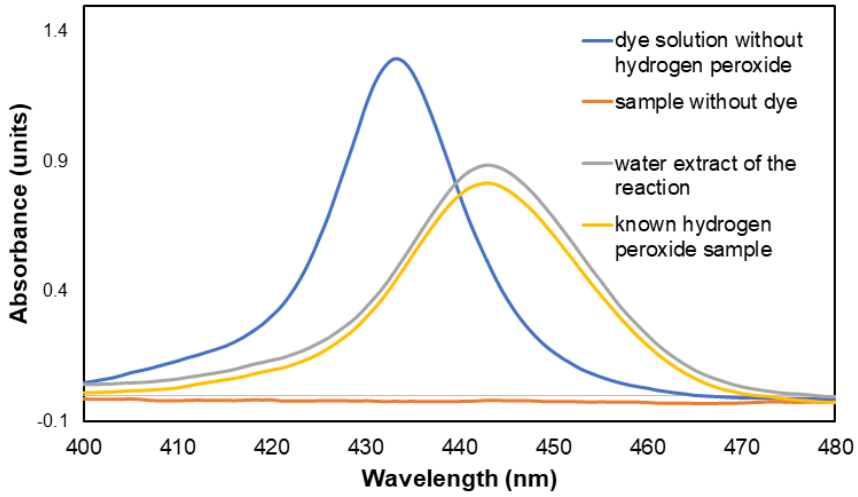

Figure 4-5. The UV-Vis spectrum of the Ti-porphyrin dye (blue) shows a characteristic absorption band at 432 nm. The characteristic peak is missing in absence of the dye (orange). The water extract of the reaction mixture (grey), and a hydrogen peroxide solution of known concentration (yellow) shows a shift in the absorption peak to 445 nm.

In absence of NHPI (Entries 3, 4, and 5), and light (Entries 5, 8, and 9) no H_2O_2 was detected. To investigate the role of temperature two reactions were ran at in the 0 ^{0}C in presence, and absence of light. The reaction tested positive for H_2O_2 production at 0 ^{0}C in presence of light (Entry 10), however no H_2O_2 was observed under the dark reaction conditions (Entry 11). To evaluate the role of the photosensitizer (Rose Bengal), the reaction was run without Rose Bengal (Entry 2). The blue coloration on the test-strip confirmed the presence of peroxide, however, when the reaction mixture was subjected to ^{1}H NMR only trace amounts of oxidation product (**3**) and no peroxide was observed. Production of trace amounts of oxidation products (**2**, and **3**) in absence of a photosensitizer could be caused by the direct excitation of NHPI under white light. In acetonitrile, NHPI shows absorption bands at 218 nm (ε = 39711 M^{-1} cm^{-1}) and 293 nm (ε = 1762 M^{-1} cm^{-1}) with a tail out to 360 nm that could be directly excited by the white light (**Figure 4-6**).[131] Since the dissociation energy of the O-H bond is 88.1 kcal mol^{-1}, excitation into the low-energy absorption band of NHPI would be energetic enough to break this bond and directly form the PINO radical.[34,35]

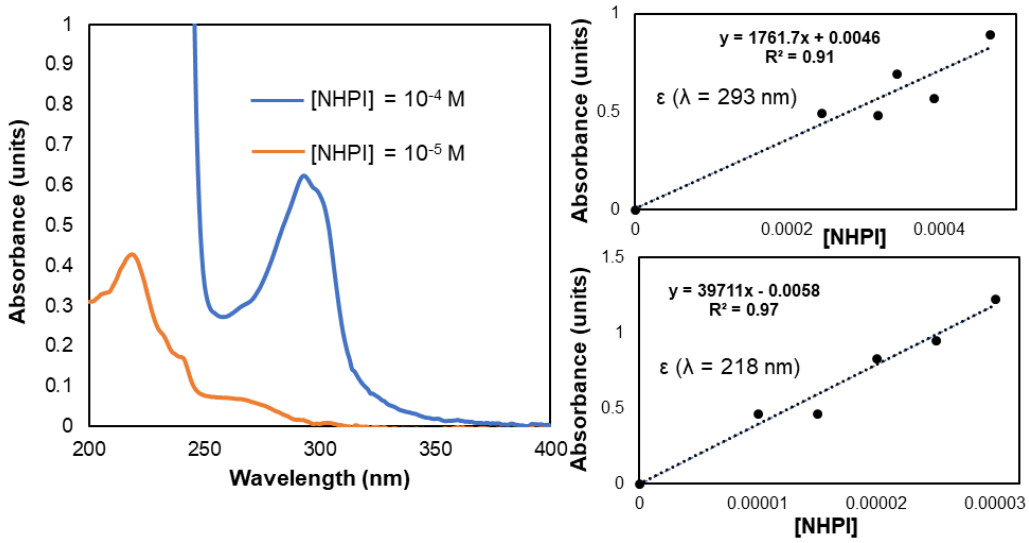

Figure 4-6. UV-Vis absorption spectra of NHPI, at two different concentrations (10^{-4} M, and 10^{-5} M) in acetonitrile (left) and the molar extinction coefficients (ε) at wavelengths, λ = 293 nm (top right), and λ = 218 nm (bottom right).

Table 4-1. Control experiments by varying the reaction conditions. The '+' sign denotes the presence and the '-' sign denotes the absence of the photosensitizer rose bengal. The blue coloration on the test strips indicate the production of H_2O_2 denoted by a '+' sign, whereas a '-' sign denotes no color change on the test strip indicating no H_2O_2 production.

Entry	[1] mmol	[NHPI] mol%	O_2	Light	Temperature (^{0}C)	Rose Bengal	H_2O_2 test
1	5	10	+	white	25	+	+
2	5	10	+	white	25	-	+
3	5	-	+	white	25	+	-
4	5	-	+	white	25	-	-
5	5	-	+	-	25	-	-
6	-	10	+	white	25	+	-
7	5	10	-	white	25	+	-
8	5	10	+	-	25	-	-
9	5	10	+	-	25	+	-
10	5	10	+	white	0	+	+
11	5	10	+	-	0	+	-

4.3 Stability of the Reaction

The stability of the oxidation products (**2** and **3**) under the reaction conditions were monitored using ^{1}H NMR over a period of 18 days (**Figure 4-7**). The yield of the oxidation

product (**3**) was calculated by taking the ratio of the integration of aromatic protons corresponding to the products and the sum of the integrations of aromatic protons of the product (**3**) and the starting material (**1**). Similarly, yield of H_2O_2 was measured by the ratio of the integration of protons of H_2O_2 and the sum of integrations of aromatic protons of the product and the aromatic protons of the starting material (**1**). Both the oxidation products were stable under the reaction conditions throughout the experimental window of 18 days as no decomposition products were observed in the NMR spectrum. The reaction terminates at ~80% of **3** and ~55% of **2** around 12 days of irradiation time. These yields persist without decomposition with continued an additional 6 days of irradiation.

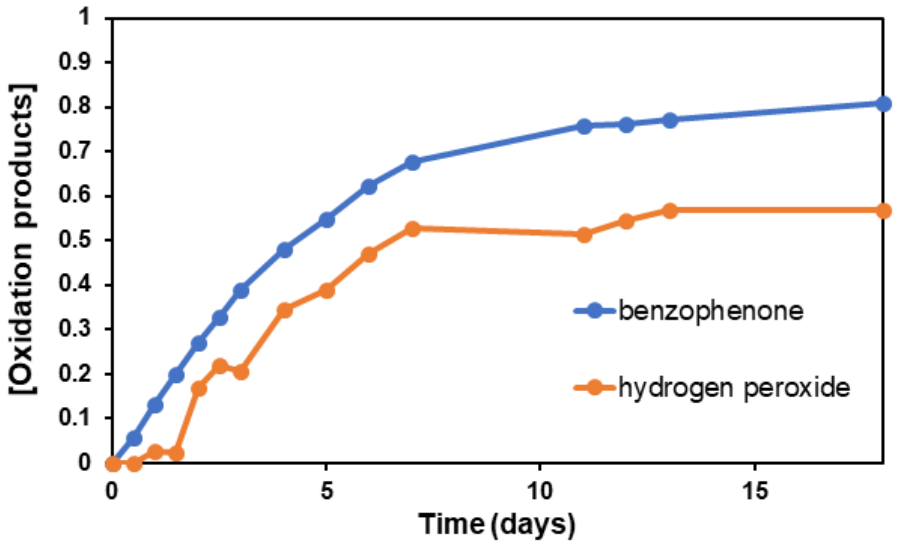

Figure 4-7. Stability of the oxidation products (benzophenone, and hydrogen peroxide) measured over a period of 18 days using ^{1}H NMR spectroscopy of the reaction mixture.

4.4 Reaction Optimization

The reaction condition was optimized by running a three variable full factorial design of experiments (**Table 4-2**). The variables considered in this study were concentration of the catalyst (NHPI in mol%), concentration of the photosensitizer (Rose Bengal in M), and the irradiation time (in days). Using a full factorial design of experiment allows for reaction optimizations with few experiments, and accounts for interacting variables. The % yield was calculated using ^{1}H NMR with respect to an internal standard, ethylene carbonate. After calculating the main and interaction effects of the variables it was observed the yield was maximized at lower levels of catalyst loading (5 mol%) and photosensitizer concentration (1×10^{-4} M) but longer irradiation time (3 days). In the previous work by Ishii *et al.* in thermal condition 10 mol% catalyst loading yielded maximum turnover.[40] In our photochemical conditions the better performance with a lower catalyst-loading can be attributed to the decomposition of radical intermediates at elevated temperatures. Longer irradiation time increasing the product concentration agrees with the ^{1}H NMR stability experiments and validates the slower aerobic oxidation kinetics.

Table 4-2. Three variable full factorial optimization design for the photocatalytic aerobic oxidation of diphenylmethanol. The effect of catalyst concentration, photosensitizer concentration, and irradiation time were investigated for the optimization experiments.

Reaction	[NHPI] mol%	[Rose Bengal] $\times10^{-4}$ M	Time (days)	%yield	
				3	2
1	10	4	2	10	6
2	5	1	1	4	-
3	15	1	1	3	1
4	5	7	1	5	1
5	15	7	1	5	1
6	5	1	3	77	50

7	15	1	3	21	14
8	5	7	3	26	6
9	15	7	3	22	15

4.5 Quenching Experiments

To gain insight on the mechanism of the photocatalytic aerobic oxidation of benzhydrol to benzophenone using NHPI in presence of a photosensitizer, quenching experiments were run by the addition of different scavengers (Q) for intermediates (**Table 4-3**).[125] Addition of sodium azide as a singlet oxygen ($^1O_2$) scavenger entirely quenched the reaction. No oxidation products were observed after three days of irradiation. Addition of benzoquinone as a superoxide (O_2^-) scavenger lowered the yield. These two experiments together suggest the primary reactive oxygen species responsible for the reaction is $^1O_2$ but that superoxide may be present and contributing to the reaction yield. Similarly, the suppression of the yield of the oxidation products upon the addition of ammonium oxalate and *tert*-butyl alcohol suggests that the reaction is dependent on the hole and radical intermediates, respectively. This observation further validates the lower yield of oxidation products for the primary alcohol. The benzylic radical intermediate has a lower stabilization for the primary alcohol when compared to the corresponding radical intermediate generated from the secondary alcohol, lowering the overall yield of the reaction.

Table 4-3. Quenching experiments to investigate the nature of the reactive oxygen species (ROS) and the reaction intermediates.

Entry	Q	Q type	Yield (%)
1	-	-	70
2	NaN_3	$^1O_2$	0
3	Benzoquinone	O_2^-	12

4	$(NH_4)_2C_2O_4$	hole	4
5	^{t}BuOH	radicals	19

The investigations on the role of each of the components and the determination of the identities of the reaction intermediates by the quenching experiments provides valuable information regarding aerobic oxidation mechanism of activated benzylic alcohols using a photocatalyst, NHPI. Experimental results suggest that, white light irradiation converts NHPI to PINO radical by the homolytic cleavage of the O-H bond. PINO initiates oxidation mechanism by abstraction of a benzylic H atom which further reacts with a $^1O_2$. The hydroxy (perhydroxy) radical intermediate, thus formed, undergoes a series of reactions that ultimately leads to the formation of a carbonyl product along with the release of a H_2O_2 molecule. The reaction mechanism proposed herein, was explored using Density Functional Theory (DFT) calculations.

4.6 Computational Studies

The energetics of this reaction was investigated using DFT calculations to further support the proposed mechanism. The geometry of the intermediates were optimized using B3LYP/6-311+G(d,p) method implementing an implicit polarized continuum solvation model for acetonitrile in Gaussian09 software package.[55,80] Three probable reaction combinations were modeled using $^1O_2$ and $^3O_2$, and $^2O_2^-$ to calculate free energy change associated with the generation of PINO radical from NHPI (ΔG_{rxn}), which is the most crucial step in NHPI catalyzed aerobic oxidation (**Table 4-4**). PINO acts as the active catalyst that initiates the radical chain reaction by abstracting the methylene H atom of the secondary alcohol (**1**).

Table 4-4. Different reaction combinations and calculated free energy changes (ΔG_{rxn}) for the formation of PINO.

Entry	Reaction Combinations	ΔG_{rxn} in PCM acetonitrile (kcal mol^{-1})
1	^{1}NHPI + $^3O_2$ → ^{2}PINO + ^{2}HOȮ	23.25
2	^{1}NHPI + $^1O_2$ → ^{2}PINO + ^{2}HOȮ	-15.43
3	^{1}NHPI + $^2O_2^-$ → ^{2}PINO + ^{2}HOȮ	12.07

Unsurprisingly, reactions involving the more energetic $^1O_2$ is thermodynamically most favorable characterized by the highest negative free energy change value (Entry 2). However, the less positive Gibbs energy change corresponds to a reaction that follows a direct excitation of the catalyst using superoxide (Entry 3). These results suggest that $^1O_2$ can react with NHPI to generate PINO. Direct reaction with ground state $^3O_2$ was energetically most unfavorable as seen in DFT calculations (Entry 1).

The catalytic mechanism for the aerobic oxidation of **1** to **3** were modeled using the following steps (**Scheme 4-2**). The H atom abstraction by PINO from **1** to form the radical intermediate (Int 1) has a free energy of -2.03 kcal mol^{-1}. The second step of the catalytic cycle of formation of the hydroxy (perhydroxy) intermediate (Int 2) was modeled using both $^1O_2$ and $^3O_2$ as oxidants. DFT calculations reveal that formation of Int 2 is thermodynamically more favorable in presence of $^1O_2$ (ΔG_{rxn} = -40.25 kcal mol^{-1}) than $^3O_2$ (-1.56 kcal mol^{-1}). This observation supports the results from the quenching experiments as it was established that excited state $^1O_2$ is the key reactive oxygen species in these transformations. The metastable hydroxy (hydroperoxy) intermediate (Int 3) formation followed by the release of H_2O_2 (**2**) to form organic oxidation product **3**, have thermodynamic free energies of -5.11 kcal mol^{-1}, and -15.53 kcal mol^{-1}, respectively.

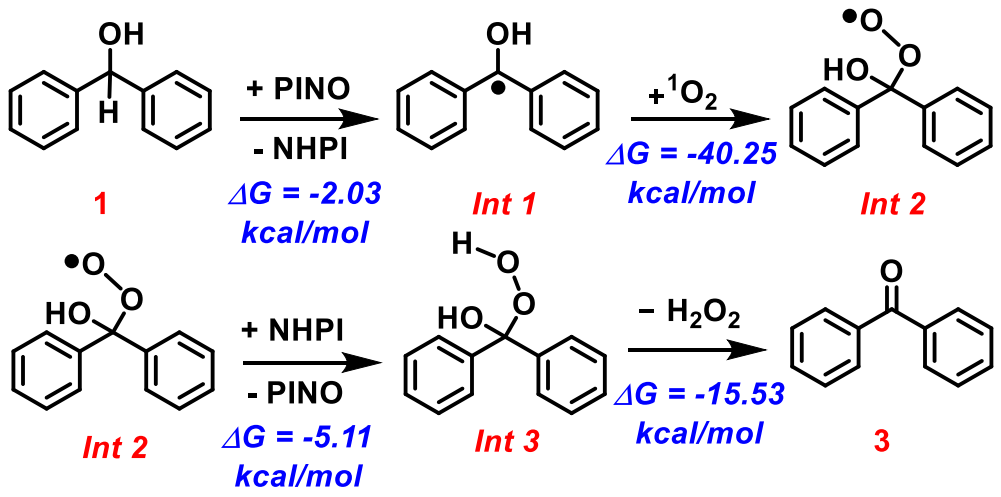

Scheme 4-2. Computationally investigated (B3LYP/6-311+G(d,p) in polarized acetonitrile solvation model) catalytic mechanism of aerobic oxidation of diphenylmethanol including the free energies of the intermediate steps (shown in blue).

4.7 Conclusions

In summary, the use of NHPI to perform aerobic oxidation reactions addresses different challenges in the field of aerobic oxidation catalysis. First and foremost, this method is a greener alternative to most common alcohol oxidation reactions. NHPI is a simple organic compound, this allows us to tune the efficiency through simple modifications. Photochemical oxidation can be performed at room temperature or lower. Most importantly, this method generates H_2O_2 as a value-added product. Due to the absence of any metal-containing strong oxidizing agent and mild reaction conditions, the generated H_2O_2 will not be decomposed and can be extracted from the mixture with simple liquid-liquid extraction procedures. The understanding of the catalytic mechanism of aerobic oxidation catalyzed by NHPI through quenching experiments supported by DFT calculations will allow us to broaden the scope of reaction by sampling a variety of

substrates. These results show the potential of using an organocatalyst that is capable of oxidizing alcohols to H_2O_2 under photochemical conditions, which is of immense interest at both laboratory and industrial scale.

Karandikar, S. S.; Bhattacharjee, A.; Metze, B. E.; Javaly, N.; Valente, E. J.; McCormick, T. M.; Stuart, D. R. Orbital analysis of bonding in diarylhalonium salts and relevance to periodic trends in structure and reactivity. *Chem. Sci.* **2022**, 13, 6532-6540.

5.1 Introduction

Diarylhalonium compounds ($Ar_2X^+Y^-$, X = Cl, Br, I; Y^- = anion) have gained attention among synthetic organic chemists over the past few years (**Figure 5-1**).[42,132–136] These compounds are known to be used as catalysts and reagents in a wide variety of conversion devoid of harsh conditions and metal containing reagents, proving to be suitable candidates for practicing environment-friendly, sustainable chemical research in the fields of natural products synthesis, drug precursor design, and generation of several important organic scaffolds.[137] Among the other group congeners, iodonium compounds are of particular interest due to the reactivity owing to the properties of the central atom.[41,138–140] Atypical, metal like behavior of iodine atom, due to the presence diffused core electrons, make these reagents extremely useful in carrying-out reaction at the organic-inorganic material interface.[137]

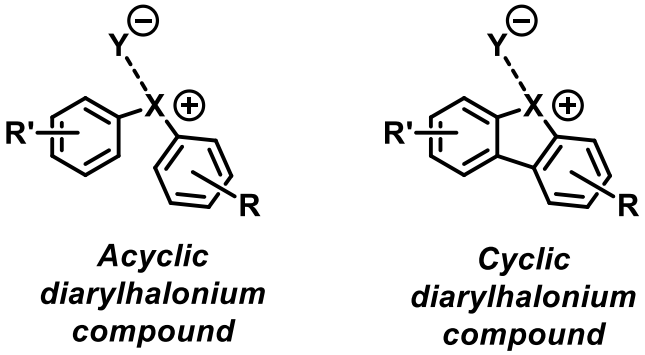

Figure 5-1. Acyclic and cyclic halonium compounds. X = F, Cl, Br, I; Y = anions; R, and R' are other aliphatic or aromatic groups.

Understanding the structure-reactivity relationship is central to the idea of novel catalyst design. Over the past few decades several attempts have been made to decipher the unusual reactivity of these compounds in order to gain insight to the mechanism of reactions performed by diarylhalonium complexes. Among those, the three center-four electron (*3c-4e*) model has been widely accepted to describe the structure.[141–143] This model can successfully shed light on the bonding of central atoms that can expand its valence shell beyond the octet. This phenomenon is termed as *hypervalency*.[144] It is widely accepted that the central halogen atoms in diarylhalonium salts adopt hypervalency to accommodate the surrounding ligands (L). The model compound $PhIL_2$ can be used to understand the hypervalent bond L-I-L under *3c-4e* framework. This model utilizes an unhybridized vacant *p*- orbital on the central I atom that is directed toward two ligand group orbitals (LGO), ϕ_1 and ϕ_2, formed through the linear combination of the valence atomic orbitals of two ligands (L^-).[145] This interaction leads to the formation of three molecular orbitals: bonding (σ), non-bonding (n), and anti-bonding (σ*), constituting a linear hypervalent L-I-L triad (**Scheme 5-1**).

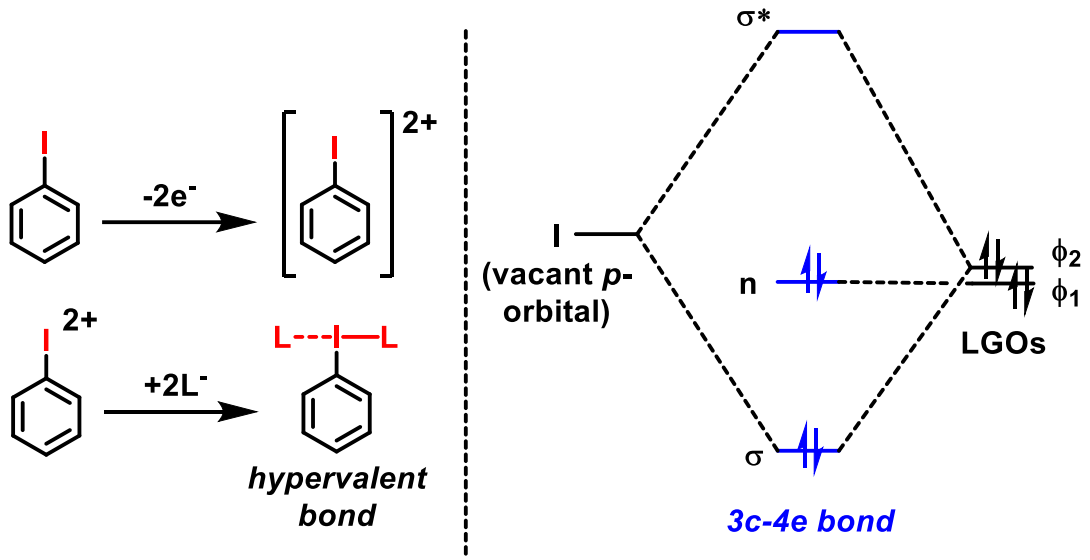

Scheme 5-1. Three center-four electron (*3c-4e*) bonding model for a hypervalent $PhIL_2$ compound: generation of a hypervalent (L-I-L) bond starting from I with filled octet (left), and the corresponding molecular orbital diagram for a *3c-4e* bonding interaction (right).

The *3c-4e* model was further modified through symmetry adapted valence bond treatment and further refined by the theory of recoupled-pair bonding model, where the overall bonding is presented as a linear combination of terms that describe the interactions between two centers (couples) at a time considering both ionic and covalent arrangements.[141] Based on these theoretical models the C(Ph)-X-L bond angles will be 90^0, and L-X-L angles will be 180^0, due to the involvement of only *p*-orbital from the central halogen atoms, which has an orthogonal symmetry.[141] These models can broadly capture the features of a hypervalent bonds observed in diaryliodonium ($Ar_2I^+Y^-$) complexes with some structural deviations. However, when the bonding theories are extrapolated to lighter halogen atoms, it fails to emulate the structural parameters observed in solid state structures

through X-ray crystallography.[135] For example, the experimental C(Ph)-X-C(Ph) bond angles for molecules **1** (97.4^0), and **2** (97.0^0) are close to the theoretical bond angle of 90^0, however, the C-Cl-C bond angle in molecule **3** shows a $+14^0$ deviation from the theoretically predicted bond angle (**Figure 5-2**).[43,146–150]

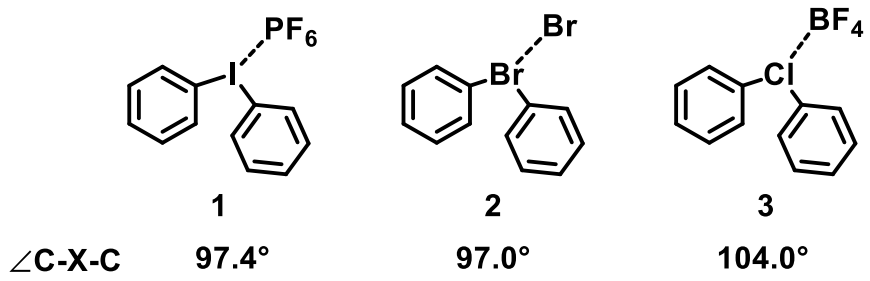

Figure 5-2. Comparison of the X-ray derived C(Ph)-X-C(Ph) bond angles for diphenylhalonium (Ph_2XY) complexes molecules: **1** (X = I), **2** (X = Br), and **3** (X = Cl).

Additionally, the observed C(Ph)-I-C(Ph) bond angles vary among the diphenyliodonium (Ph_2IY) complexes based on the identity of the anion (**Figure 5-3**). These structural aspects are absent in the original *3c-4e* description of the hypervalent halogen containing salts. The simplistic and widely accepted bonding model for these compounds suffer from major flaws owing to the exclusive involvement of *p*- orbital of the halogen atoms.

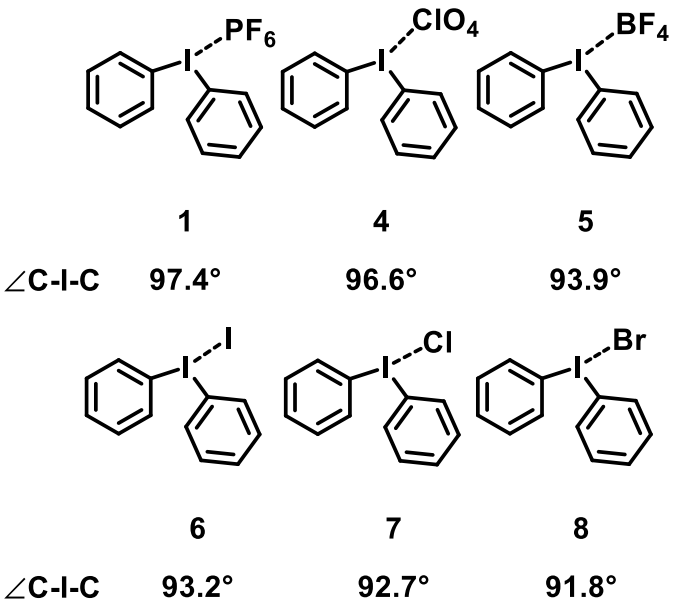

Figure 5-3. Comparison of the X-ray derived C(Ph)-I-C(Ph) bond angles for diphenyliodonium (Ph_2IY) complexes: **1** (Y = PF_6), **4** (Y = ClO_4), **5** (Y = BF_4), **6** (Y = I), **7** (Y = Cl), and **8** (Y = Br).

Furthermore, since the structure of a molecule is associated with its reactivity, the existing theoretical model fails to explain the periodic Lewis acidic properties of the halogen atom in these complexes. To accommodate these observed variations in structure and the reactivity of the diarylhalonium cations, it is necessary to redefine the bonding model. We report herein a detailed computational investigation of a series of diarylhalonium complexes and diarylchalcogenides (**Scheme 5-2**). The archetypal compound for *3c-4e* bonding model, $PhICl_2$ (**9**) was chosen to test the validity of the said bonding theory, the widely studied diphenylhalonium (**1** – **8**), and isoelectronic diarylchalcogenides (**13** – **18**) were used to standardize our novel bonding model and was applied to three newly synthesized and characterized phenyl(mesityl)halonium

tetrafluoroborate (**10** – **12**) to further validate our approach. This was achieved by comparing the computationally derived bond parameters with the X-ray diffraction data.

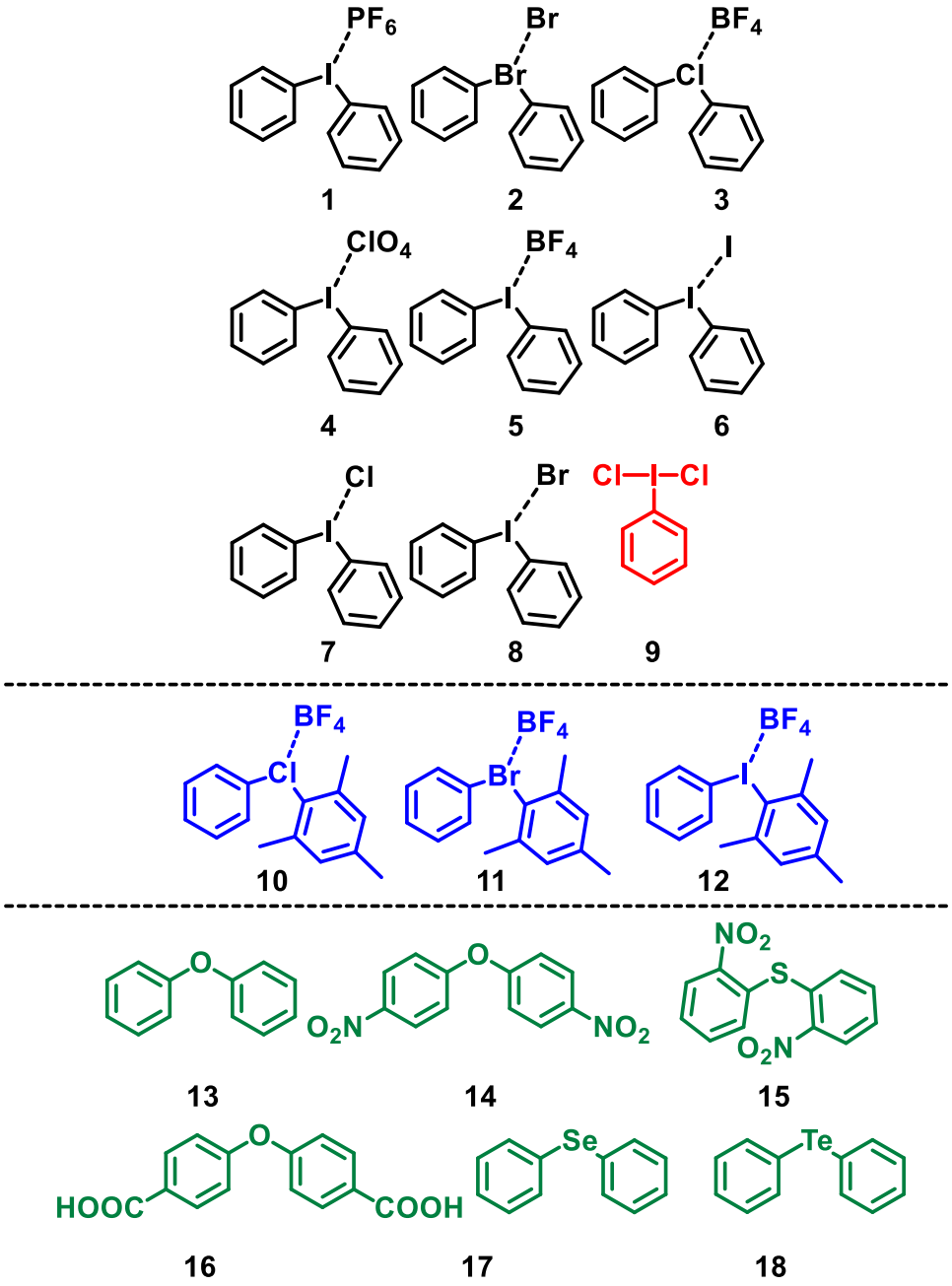

Scheme 5-2. Molecules studied in this work: diphenylhalonium complexes (**1 – 8**, shown in black), prototypical compound for *3c-4e* bonding model, PhI_2Cl (**9**, shown in red), phenyl(mesityl)halonium tetrafluoroborate complexes (**10 – 12**, shown in blue), and isoelectronic diarylchalcogenides (**13 – 18**, shown in green).

We report, herein, a novel and generalized approach to describe the bonding of compounds within the Lewis' octet framework as well as, so-called hypervalent complexes.[151,152] This generalized bonding model is based on qualitative Bent's rule and was achieved by the inclusion of *s*-orbital contribution of the central atom in conjunction with the *p*-orbitals, which was absent in the previously adopted bonding theories.[153] The prominent correlation of the computationally derived results with the experimental data validates this approach and further justifies the use of this method to discuss structure of similar compounds in order to derive a better structure-function relationship.

5.2 Computational Methods

All Density Functional Theory (DFT) calculations were performed using Gaussian09 quantum chemistry package.[80] To optimize the computational method, geometry optimization calculation was performed with the crystal structure of diphenyliodonium iodide, Ph_2II (**6**, CCDC id: DIRZOT01) using two density functionals, namely: B3LYP, and M06-2X; and a combination of a variety of basis functions in gas phase.[154,155] The optimized structures were subjected to single point energy calculation. The combination that produced the lowest energy structure along with the best correlation with the experimental parameters was: B3LYP/Def2QZVPP (for I atoms), and cc-PVTZ (for lighter C,H atoms). Subsequently, geometry optimization of all molecules were performed using B3LYP functional along with a split basis set combination of Def2QZVPP (for I, and Te) and cc-PVTZ (for lighter atoms such as C, H, B, N, O, F, P, Cl, Br, S, and Se). The optimized structures were subjected to frequency calculation using normal mode analysis to ensure the achievement of stationary points with zero imaginary frequencies.

Natural Bond Orbital (NBO) analyses at B3LYP/LanL2DZ (for all atoms) were performed on the geometry optimized structures using NBO 3.1 module as implemented in Gaussian09 to extract the atomic *s*- and *p*- orbital contributions to the bonds with central halogen and chalcogens.[14,15] Finally, Hirshfeld charge analyses were performed using Multiwfn 3.7 wavefunction analyzer to correlate Lewis acidity with the atomic charges of the central atoms.[87]

5.3 Results and Discussions

5.3.1 Bent's rule.

The theory of hybridization provides a semi-quantitative description of the formation of covalent bonds.[141,151,152] This involves a depiction of mixing of atomic orbitals (such as *s*, *p*, *d etc.*) of the central atom in different proportions to create hybrid orbitals of different nature (such as, sp, sp^2, sp^3 *etc.*). These hybrid orbitals obey Pauli's exclusion principle while filling up with electrons to accommodate ligands in order to form a molecule. The model successfully describes bonding and structures of several molecules containing 2^{nd} period elements as the central atom , for example, CH_4, C_2H_2, NH_3 *etc.* However, it fails to account for structural deviations observed in molecules containing heavier central atoms. Furthermore, the description of orbital mixing is restricted to only central atoms and does not account for different structural aspects based on the identity of the incoming ligands. Henry A. Bent formalized a new bonding model where he combined the mixing of atomic orbitals of central atom and the electronegativity of the approaching ligand to account for the anomalies observed under the hybridization framework. In this model, Bent introduced the concept of orbital contribution such as, %*s*- character, and %*p*-

character, form the central atom that is being directed to the ligands during the formation of a covalent interaction. He showed that depending on the nature (electronegativity) of the approaching ligands the same central atom might direct different hybrid orbitals with unequal *s*- and *p*-characters. The statement of Bent's rule is as follows: *atomic s-character concentrates in orbitals directed toward electropositive substituents*.[153] Conversely, for electronegative substituents, hybrid orbitals directed by central atom will have higher *p*-orbital contribution.

The inclusion of unequal orbital contribution toward substituents with different electronegativities changed the existing bonding model for covalent interactions. This could successfully explain the structural deviations observed not explained by hybridization and Valence Shell Electron Pair Repulsion (VSEPR) theories. This model provides a more generalized approach to understand bonding and incorporate periodic trends for molecules formed by group congeners. We report herein a detailed investigation of the bonding in acyclic diarylhalogen cations and isoelectronic diarylchalcogen compounds through the lens of Bent's rule using computational calculations of s and p character of bonding orbitals.

5.3.2 Hypervalency and orbital contribution.

To investigate the applicability of Bent's rule on the molecules containing hypervalent central atom, phenyliodonium dichloride, $PhICl_2$, (**9**) was chosen. It is supported by the X-ray crystallography that this molecule contains two symmetric I-Cl bonds (**Figure 5-4**). This means, if two Cl atoms are designated as Cl(a) and Cl(b), then Cl(a)-I-C(Ph) and Cl(b)-I-C(Ph) are both 89.9^0. The Cl(a)-I-Cl(b) angle is 179.9^0. This

bond parameters are very similar to the ones predicted by the theory of *3c-4e* bond model where Cl-I-Cl should be 180^0, and Cl-I-C is 90^0.

NBO analysis of the I-C(Ph) bonds reveal that the %*p*- character directed by the atomic orbitals of I toward C(Ph) is 99.95% as predicted by the *3c-4e* model. This further validates the involvement of an unhybridized atomic *p*- orbital of I in the C(Ph)-I bond. In summary, the inclusion of orbital contributions into well-known hypervalent compound is acceptable and provides excellent correlation with the experimentally obtained bond parameters.

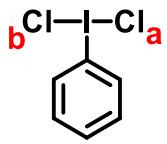

∠Cl(a) - I - Cl(b) = 179.9°
∠Cl(a) - I - C(Ph) = ∠Cl(b) - I - C(Ph) = 89.9°

Figure 5-4. Different bond angles involving the hypervalent I atom in $PhICl_2$ molecule obtained from X-ray diffraction studies.

5.3.3 Correlation of orbital contribution and structure.

Excellent correlation ($R^2 = 0.98$) was achieved when the X-ray derived bond angles of the known diphenylhalonium compounds, $Ph_2X^+Y^-$, (**1** - **8**) and diarylchalcogenides, Ar_2E, (**13** - **18**) were compared against DFT calculated bond angles (**Figure 5-5**). This further validates the computational method chosen for investigating a variety of compounds. The strong correlation ($R^2 = 0.99$) between the %*p*- orbital contribution to the hybrid orbitals directed by halogen (X) and chalcogen (E) central atoms toward the

substituents suggests that *3c-4e* model is inapplicable in the case of understanding the bonding in such compounds (**Figure 5-6**).

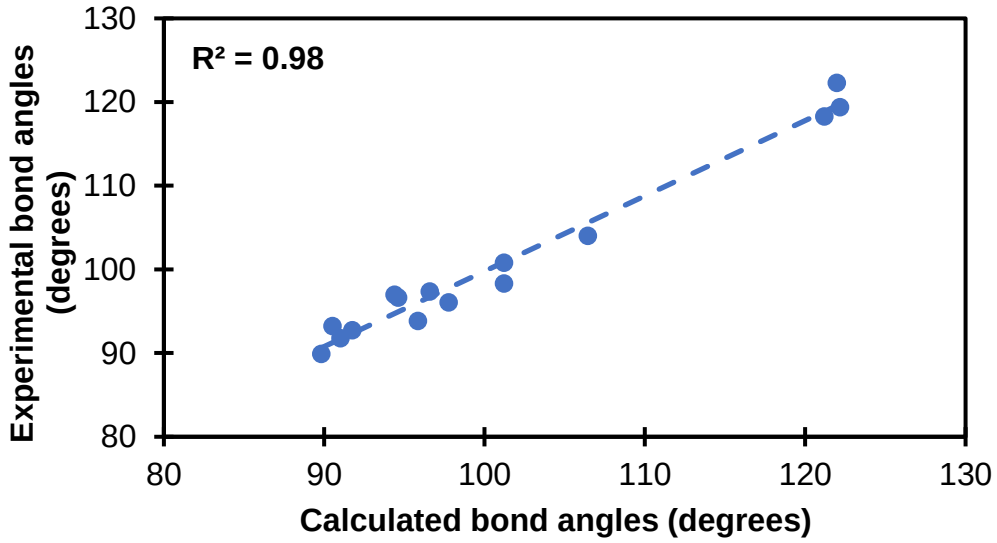

Figure 5-5. Correlation of experimental and calculated bond angles for diphenylhalonium (**1** – **8**) complexes and diarylchalcogenides (**13** – **18**).

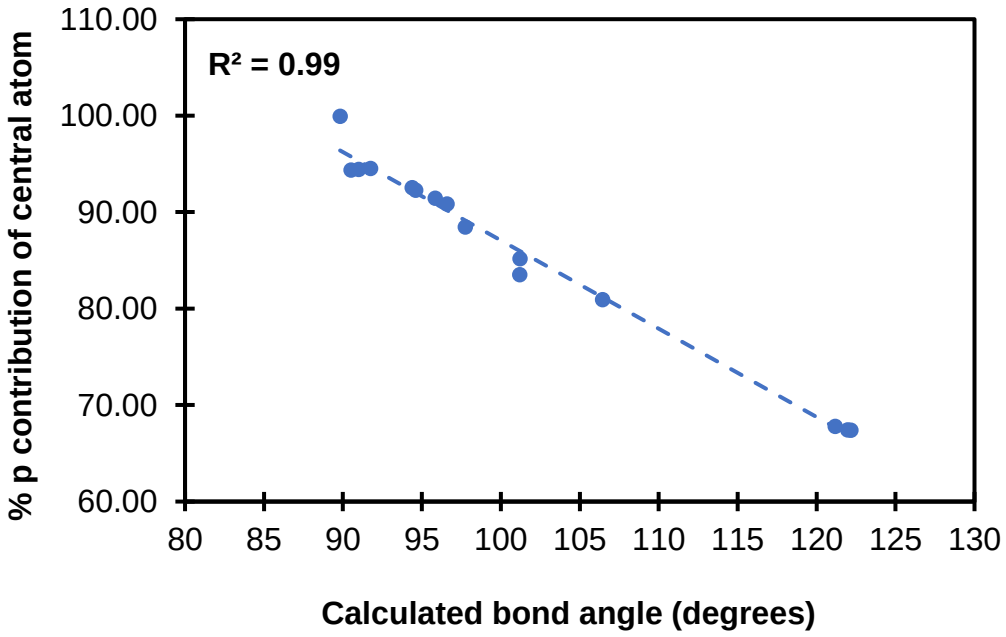

Figure 5-6. Correlation between the %p contribution from the central atom and the DFT calculated bond angles for the diphenylhalonium (**1** – **8**) complexes, phenyliodonium dichloride (**9**) and diarylchalcogenides (**13** – **18**).

The generalized bonding theory inspired by Bent's rule, proposed herein, is capable of accounting for the periodic trend observed in the structure of diphenylhalonium and diarylchalcogen compounds, irrespective of the identity of the central atom. For example, when compared for the chalcogenides (E = O, S, Se, Te) the C(Ar)-E-C(Ar) angle decreases as going down the group (**Table 5-1**). The atoms with higher atomic mass and lower electronegativities concentrate more *p*- character to the bond toward the aryl group attaining an orthogonal symmetry, meaning bond angle closer to 90^0 as predicted from the *3c-4e* bonding model. However, central atoms with higher electronegativities uses more *s*-type orbital indicating a spherical symmetry resulting in higher bond angles, which is not understood by the original *3c-4e* description.

Table 5-1. Correlation between periodicity and the structure of the molecules 13 - 18.

Molecule	E	X-ray bond angle (^{0})	DFT calculated bond angle (^{0})	%*s*-character	%*p*-character
13	O	118.3	121.2	32.2	67.8
14	O	119.4	122.2	32.6	67.4
15	S	100.8	101.2	16.5	83.5
16	O	122.3	122.0	32.6	67.4
17	Se	98.3	101.2	14.8	85.2
18	Te	96.1	97.8	11.6	88.4

The similar observations were made with the diphenylhalonium (Ph_2XY) complexes (**Table 5-2**). The C(Ph)-X-C(Ph) bond angle becomes less obtuse going down group 17. Less electronegative I atom utilizes more *p*- character in the hybrid orbital directed toward the C atom of the phenyl group than more electronegative Cl atom (**1** – **3**). The quantitative involvement of *p*- orbital from central I atom also change depending on the identity of the anionic substituents, Y (**1**, and **4** – **8**).

Table 5-2. Correlation between periodicity and the structure of the molecules **1** - **8**.

Molecule	X	Y	X-ray bond angle (^{0})	DFT calculated bond angle (^{0})	%*s*-character	%*p*-character
1	I	PF_6	97.4	96.6	9.2	90.8
2	Br	Br	97.0	94.4	7.4	92.6
3	Cl	BF_4	104.0	106.4	19.1	80.9
4	I	ClO_4	96.6	94.6	7.7	92.3
5	I	BF_4	94.0	95.9	8.6	91.5
6	I	I	93.2	90.5	5.6	94.4
7	I	Cl	92.7	91.7	5.5	94.5
8	I	Br	91.8	91.0	5.6	94.4

5.3.4 Bonding in unsymmetrical phenyl(mes)halonium compounds.

The generalized bonding model described in the previous section was tested for a series of unsymmetric phenyl(mes)halonium tetrafluoroborates, $Ph(Mes)XBF_4$, where mes = 2,4,6-trimethylphenyl group, (**10** - **12**). These molecules were synthesized and

characterized through X-ray crystallography (Thanks to Shubhendu Karandikar, and Edward J. Valente) to obtain the structural parameters (bond angle, and bond length) and compared with the DFT calculated structures (**Scheme 5-3**). Unsurprisingly, the halogen atoms direct hybrid orbitals with different %*p*- characters toward the different aryl substituents (phenyl, and mesityl). The C-X bond lengths are also different for a halonium compound depending on the identity the aryl substituents (**Table 5-3**).

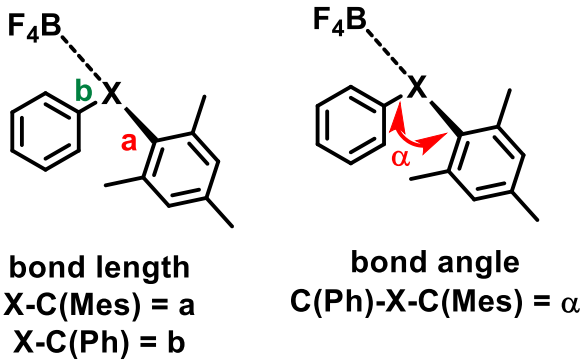

Scheme 5-3. Structural parameters (bond angles and length) for unsymmetrical diarylhalonium molecules **10** – **12** as described in Table 3.

Table 5-3. Structural parameters and %p- character directed toward two different aryl groups in the series of phenyl(mes)halonium tetrafluroroborate molecules **10** - **12** as defined in Scheme 5-3.

Molecule	X	a (Å)	b (Å)	α (^{0})	%*p*- character of X toward Mes group	%*p*- character of X toward Ph group
10	Cl	1.79	1.82	107.1	80.4	82.0
11	Br	1.94	1.96	102.6	86.3	86.1
12	I	2.13	2.14	96.7	90.7	88.1

For example, the C(Ph)-X-C(Mes) bond angle (α) decreases going from chloranium to bromonium to iodonium complex with a subsequent increase in the %*p*- character of the orbitals directed towards the aryl (phenyl, and mesityl) groups. This observation is consistent with the current hypothesis based on Bent's rule. However, it was observed that

the bonding of the halogen atoms with two different aryl groups are different in nature. For example, the C (Mes)-X bond length (a) is smaller than the corresponding C(Ph)-X bond length (b). This can also be attributed to the involvement of more *p*- character containing hybrid orbitals toward the bonding between the halogen atom and more electron-rich mesityl ring. These observations from the DFT calculations were supported by X-ray diffraction studies as experimental C(Ph)-X-C(Mes) bond angle decreases from 107.8^0, to 104.6^0, followed by 102.3^0 when moving down the group from Cl, to Br, to I, respectively.

Finally, in attempt to correlate Lewis acidity of these molecules with the nature of bonding orbitals, Hirshfeld charge analysis was performed. This was achieved by mapping the atomic charges on the electrostatic potential surface of the molecules (**Figure 5-7**).[156] It was observed that the anionic tetrafluoroborate (BF_4^-) ligands prefer to occupy the site *trans* to the mesityl ring and creates an electropositive site *trans* to the phenyl ring, usually referred to as the *sigma hole*. Any Lewis acidity shown by these types of compounds is related to the size and magnitude of the electropositive site on the halogen atoms. It was observed on the charge density map that the area of the electropositive *sigma hole* and the magnitude of electropositivity increases going from Cl to Br, to I, which can be correlated to the atomic electronegativity order of the halogen atoms.

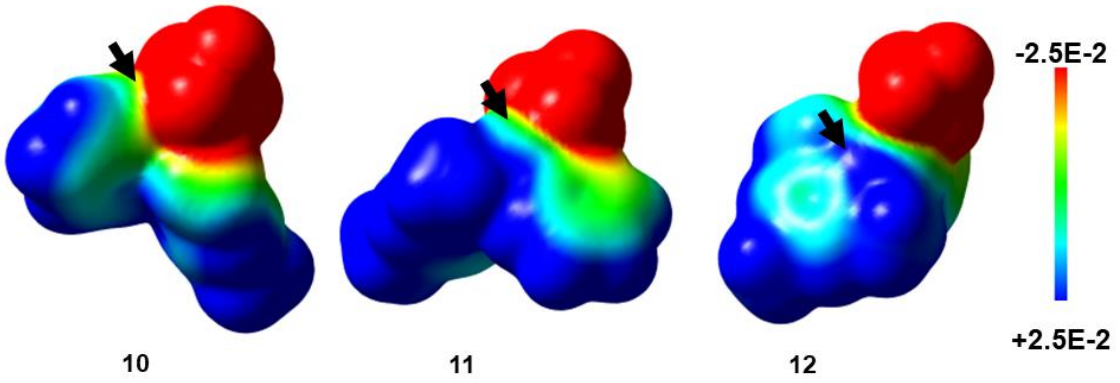

Figure 5-7. Charge density map of the diarylhalonium molecules. The increase in positive charge density on the halogen atoms from Cl to Br to I is shown using black arrows. The scale for atomic charge density is presented in atomic units.

5.4 Conclusion

The *3c-4e* bonding model is an excellent tool to predict the structure and reactivity of some hypervalent molecules. However, it fails to account for any role imparted by the individual central atom toward different substituents with different electronic properties beyond the Lewis octet framework. We report a more generalized bonding model by including both %*s*- and %*p*- characters of the hybrid orbitals donated by the central halogen atoms to a wide variety of substituents. As proposed by Bent, bonding interaction varies depending on the electronegativity of the central atoms as well as the approaching ligands, we observe similar behavior in the diarylhalonium complexes and diarylchalcogenides.

The halogen and chalcogen atoms with higher atomic mass and lower electronegativity utilizes orbitals with more *p*- character when compared with the atoms with lower atomic mass and higher electronegativity. This novel bonding model for these classes of molecules can explain the orthogonal symmetry of the molecules containing I or Te atoms, as predicted by the *3c-4e* model along with the spherical symmetry shown by

the molecules containing O or Cl, where *3c-4e* model breaks down, through the use of varying *s*- and *p*- orbital contributions. This work highlights the importance of considering *s*/*p*- mixing as a parameter to describe the structure-function relationship of diarylhalonium salts and may be applied to other types of non-covalent interactions shown by the main-group elements.

Chapter 6 Conclusions

Computational chemistry has proven to be an indispensable tool for molecular modeling in the field of catalyst design since the discovery of Kohn-Sham DFT over seventy years ago.[9,10,16,157] Since then, a number of sophisticated methods have been developed to study chemical systems in greater detail.[6,8,158] Molecular models can be useful, or even indispensable tools to investigate the structure-function relationship and provide a better understanding of the underlying quantum mechanics of small molecular systems. Computational chemistry has proved to be useful where the testing of hypotheses using experimental techniques are unfeasible.[159]

However, the use of molecular models developed by computational methods, are only useful if they provide a better understanding of a system through experimental evidence or if they can provide suitable objectives for experimental design. It is for this reason; molecular modeling has to be adequate and the parameters used to develop the models need to be defined with maximum precision and accuracy. Otherwise, the model is considered insufficient and inefficacious.

This work entails the study of four chemical systems with the objective of development of better computational means to understand the experimental observations related to the structure-function relationship and furthermore, to develop a strategy for experimental catalyst design through the assistance of computational tools. This was achieved by 1) the study of a family of Ni(II) tris-pyridinethiolates, well-known water reduction catalysts that work under both photochemical and electrochemical conditions, 2)

developing a novel strategy to produce H_2O_2 by the photochemical reduction of aerobic oxygen and simultaneous oxidation of benzylic alcohols, and 3) developing a generalized bonding model for the class of hypervalent halonium salts by the inclusion of *%s*-orbital contribution into the existing *3c-4e* bonding theory.

6.1 Effect of Intramolecular H-Bonding on the Catalytic Cycle of Water Splitting Using a Ni(II) Catalyst

Photochemical and electrochemical conversion of protons (from water or acids) to H_2 gas utilizing Ni(II) tris-pyridinethiolate catalysts has been studied for almost a decade. These catalysts can efficiently convert H^+ to H_2 with a high turnover rate through a chemical-electrochemical-chemical-electrochemical (CECE) process. In the previously reported literature, the catalytic mechanism of these complexes were explored through computational techniques. However, due to non-exhaustive configuration scan on the potential energy surface of the catalytic mechanism, the effect of localized intramolecular H bonding interactions were not explored.

In this work, we redefine the molecular model to study the catalysis in order to identify the impact of electronic and structural effects on the catalytic cycle of the family of $[Ni(PyS)_3]^-$ catalysts. The most useful outcomes of this projects are: 1) The first protonation step of the catalytic cycle generates structural isomers of varying thermodynamic properties and stabilities, 2) The unequal stability of these isomers can be attributed to the strength of an intramolecular H bond between the proton on the pyridyl N atom and one of the adjacent thiopyridyl S atoms, where the stronger H-bonding interaction

results in a more stable isomer. This greatly affects the basicities of the pyridyl N atoms. Furthermore, the protonation is guided by the intramolecular H-bond formation instead of originally proposed thermodynamic *trans effect*. Intramolecular H-bonding is well-observed and characterized in biologically relevant macro-molecular systems, such as proteins, and nucleic acids, however, it is not explored in small molecules. (3) During first reduction step of the catalyst, the overall coordination geometry around the Ni-center gets altered due to the reorganization of the chelating ligands. The structure optimizes either to a square pyramidal (*sq. py.*) intermediate or a trigonal bi-pyramidal (t_bp) intermediate. The t_bp intermediates are more stable although, the *sq. py.* intermediates can form better H bonding interactions. These observations demonstrate the importance of considering structural isomers while performing computations on these complexes and other compounds with allied structural features in order to gain unambiguous insight into the mechanism and better correlation with the experimental results.

6.2 Heteroleptic catalyst design for proton reduction

This work provides computational insight on finetuning the efficiency of water splitting by Ni complexes through heteroleptic catalyst design. As mentioned earlier, the mechanism of proton reduction by $[Ni(PyS)_3]^-$ is initiated by protonation of a pyridyl N atom followed by the reduction of N(II) center to a Ni(I). The two main thermodynamic parameters responsible for the catalysis are pK_a and E^0. The pK_a of the catalyst can be modified by the introduction of an electron donating group (D) while tuning the E^0 requires an electron withdrawing group (W) in the ligand framework for a better catalytic activity in basic media. Since these two thermodynamic properties need to be optimized

contemporaneously, simultaneous inclusion of both D and W groups are necessary. This can be achieved by heteroleptic catalyst design.

For this work, we have explored the catalytic cycle of two heteroleptic complexes, NiD_2W and $NiDW_2$, and the thermodynamic properties were compared with the homoleptic analogues, NiD_3 and NiW_3. In this work we have included the contribution from all possible isomers generated from the protonation of the ligands and explored the role of intramolecular H bonding in the catalytic cycle.

The DFT calculations in conjunction with the topology analyses using QTAIM on these catalysts indicates better performance of a heteroleptic catalyst than the homoleptic analogue for water splitting reactions. The ideal configuration for a suitable heteroleptic catalyst for water splitting is $NiDW_2$, where one D group dictates the protonation of a specific pyridyl N atom while two W ligands optimize the reduction reaction. This work provides a comprehensive objective for the synthetic chemists to achieve a better proton reduction catalyst that performs well in elevated pH conditions with low overpotential.

6.3 Metal-free photocatalytic aerobic oxidation and H_2O_2 production

This work describes a novel strategy of oxidation of benzylic alcohols (diphenylmethanol, and phenylmethanol) to the corresponding carbonyl products (benzophenone, and benzaldehyde, respectively) using aerobic oxygen, light, an organic photocatalyst (NHPI), and a photosensitizer (Rose Bengal) and the concomitant production of H_2O_2. The use of NHPI as a photocatalyst is reported along with the use of metal and non-metal co-catalysts for aerobic oxidation reactions. However, the photochemical

oxidation of organic small molecules exclusively in presence of NHPI has not been previously reported. In addition to the use of a milder oxidant (air), and non-toxic organic photocatalyst, this method allows us to access H_2O_2 as a value-added by-product which is an industrially relevant molecule including the potential to be an alternative carbon-neutral fuel.

The computational investigation of the oxidation process supported by experimental results reveals that NHPI, in presence of light and O_2 forms a radical intermediate, phthalimide-*N*-oxyl (PINO). PINO initiates the oxidation reaction by the abstraction of a H atom from the alcohol. The photosensitizer converts the ground state $^3O_2$ to an excited state $^1O_2$ which attaches on the radical organic intermediate. Through several intermediate steps the alcohol is oxidized to the corresponding carbonyl compound and a molecule of H_2O_2 is released. In the process NHPI is regenerated. The catalytic system is stable for over two weeks as no decomposition products were observed by the ^{1}H NMR spectroscopy of the reaction mixture over time. The generated H_2O_2 can be isolated from the reaction mixture by a simple liquid-liquid extraction.

This process addresses different challenges in the field of aerobic oxidation catalysis. Most importantly, this method provides a greener alternative to the most common alcohol oxidation methods and generates H_2O_2 as a by-product. This process has a potential to be able to replace the current industrial production method of H_2O_2, namely the *Anthraquinone Process*. Understanding of the catalytic mechanism in greater detail will allow us to design similar photocatalysts that are capable of performing similar reactions

on a variety of substrates, which is of immense interest in both laboratory and industrial scale.

6.4 Generalized Bonding Model for Hypervalent Compounds

This work outlines the importance of structure-function relationship of a series of hypervalent central atom containing diarylhalonium compounds and the underlying importance of a better representation of structural theories that is capable of illustrating the reactivity of such compounds. The most common model that describes the bonding utilizing a hypervalent atom is the three center-four electron (*3c-4e*) model. This theory accurately describes the bonding in symmetric λ^3-iodanes, such as phenyliodonium dichloride however fails to account for the structural features in asymmetric halonium series. Furthermore, the model does not account for the identity of the central atom or the nature of the incoming ligands. Due to poor description of the bonding in such compounds, the understanding of the reactivity and non-covalent interactions such as, halogen bonding, and Lewis acidity of these compounds are not well-understood.

In our work, we have modified the existing bonding model so that the updated theory is capable of describing bonding in all hypervalent halonium salts and isoelectronic chalocogenides, not solely based on the atomic orbital contribution to the molecular orbitals directed toward the substituents, but also the electronegativity of the incoming ligands. This work is based on the qualitative description of molecular bonding put-forth by Henry Bent. The simplistic *3c-4e* model fails to account for the bonding in such species owing to involvement of only an unhybridized *p*-orbital from the halogen atom to bonding.

In our updated model, we have included orbital mixing, where both atomic *s*- and *p*-orbitals of the central halogen and chalcogen atoms are considered for bond formation.

This model successfully describes the bonding in a wide variety of compounds with excellent correlation to the experimental structure parameters, such as bond length and bond angles. Under the description of *s*- and *p*- mixing, it was revealed that elements with lower atomic numbers involve more *s*-character while higher atomic number elements utilizes more *p*-character while forming hypervalent interactions. This highlights the importance of structure-function relationship in these classes of compounds and can be further extrapolated to other types of compounds formed by the main-group elements.

While this work describes four unique projects, they are all entangled by one common theme: that the use of an appropriate molecular model are necessary for the accurate understanding of the experimental observations. As mentioned earlier, in order to harness the power and promise of computations in chemical systems an exhaustive and suitable treatment is imperative. It would be appropriate to remind ourselves with the aphorism originally proposed by statistician George Box in a 1976 paper published in the Journal of American Statistical Association: *All models are wrong but some are useful*.[160]

REFERENCES

(1) Mani, S. V; Connell, D. W.; Braddock, R. D. Structure Activity Relationships for the Prediction of Biodegradability of Environmental Pollutants. *Crit. Rev. Environ. Control* **1991**, *21* (3–4), 217–236. https://doi.org/10.1080/10643389109388416.

(2) Romualdo Benigni. *Quantitaive Structure-Activity Relationship (QSAR) Models of Mutagens and Carcinogens*; CRC Press LLC, 2003.

(3) Sleight, R. K. G. and A. W. *Structure-Activity and Selectivity Relationships in Heterogeneous Catalysis*; Elsevier, 1990.

(4) Cavallito, C. J. Structure Activity Relationships. *Pergamon* **1973**, *1 (327 p.)* (1), 3–10. https://doi.org/10.1201/b14252-19.

(5) Devillers, J. *Juvenile Hormones and Juvenoids: Modeling Biological Effects and Environmental Fate*; 2013. https://doi.org/10.1201/b14899.

(6) Jensen, F. *Introduction to Computational Chemistry*; Wiley, 2017.

(7) Levine, I. N. *Quantum Chemistry Pearson Advanced Chemistry Series*; 2014.

(8) Holthausen, M. C. K. W. *A Chemist's Guide to Density Functional Theory*, 2nd ed.; Wiley-VCH: Weinheim, 2001; Vol. 123. https://doi.org/10.1021/ja004799q.

(9) Kohn, W. Electronic Structure of Matter - Wave Functions and Density Functionals. In *Noble Lecture*; 1999; pp 213–237.

(10) Kohn, W.; Sham, L. J. Self-Consistent Equations Including Exchange and Correlation Effects. *Phys. Rev.* **1965**, *140* (4A), 1133–1138.

(11) Baseden, K. A.; Tye, J. W. Introduction to Density Functional Theory: Calculations by Hand on the Helium Atom. *J. Chem. Educ.* **2014**, *91* (12), 2116–2123. https://doi.org/10.1021/ed5004788.

(12) Bader, R. F. W. The Quantum Mechanical Basis of Conceptual Chemistry. *Monatshefte fur Chemie* **2005**, *136* (6), 819–854. https://doi.org/10.1007/s00706-005-0307-x.

(13) Iranpour, M.; Fazaeli, R.; Sadjadi, M. S.; Yousefi, M. Natural Bond Orbital (NBO) and Quantum Theory of Atoms in Molecules (QTAIM) Analyses of Iron-Substituted Borirene and Boryl Isomers. *Russ. J. Inorg. Chem.* **2019**, *64* (4), 472–477. https://doi.org/10.1134/S0036023619040107.

(14) F. Weinhold, J. P. F. Natural Hybrid Orbitals. *J. Am. Chem. Soc.* **1980**, No. 102, 7211–7218.

(15) Reed, A. E.; Weinstock, R. B.; Weinhold, F. Natural Population Analysis. *J. Chem. Phys.* **1985**, *83* (2), 735–746. https://doi.org/10.1063/1.449486.

(16) Ryu, H.; Park, J.; Kim, H. K.; Park, J. Y.; Kim, S. T.; Baik, M. H. Pitfalls in Computational Modeling of Chemical Reactions and How to Avoid Them. *Organometallics* **2018**, *37* (19), 3228–3239. https://doi.org/10.1021/acs.organomet.8b00456.

(17) Lewis, N. S. Powering the Planet. *MRS Bull.* **2007**, *32*, 808–820.

(18) Lewis, N. S.; Nocera, D. G. Powering the Planet: Chemical Challenges in Solar Energy Utilization. *Proc. Natl. Acad. Sci.* **2006**, *103* (43), 15729–15735. https://doi.org/10.1073/pnas.0710559104.

(19) Ahmad, H.; Kamarudin, S. K.; Minggu, L. J.; Kassim, M. Hydrogen from Photo-Catalytic Water Splitting Process : A Review. *Renew. Sustain. Energy Rev.* **2015**, *43*, 599–610. https://doi.org/10.1016/j.rser.2014.10.101.

(20) Eisenberg, R.; Gray, H. B.; Crabtree, G. W. Addressing the Challenge of Carbon-Free Energy. *Proc. Natl. Acad. Sci.* **2019**, 1–7. https://doi.org/10.1073/pnas.1821674116.

(21) Eisenberg, R.; Gray, H. B. Preface on Making Oxygen. **2008**, *47* (6), 1697–1699.

(22) Gray, H. B. Powering the Planet with Solar Fuel. *Nat. Chem.* **2009**, *1* (1), 7. https://doi.org/10.1038/nchem.141.

(23) Wisniak, J. The History of Catalysis. From the Beginning to Nobel Prizes. *Educ. Quim.* **2010**, *21* (1), 60–69. https://doi.org/10.1016/S0187-893X(18)30074-0.

(24) Kato, S.; Jung, J.; Suenobu, T.; Fukuzumi, S. Production of Hydrogen Peroxide as a Sustainable Solar Fuel from Water and Dioxygen. *Energy Environ. Sci.* **2013**, *6* (12), 3756–3764. https://doi.org/10.1039/c3ee42815j.

(25) Fukuzumi, S. Artificial Photosynthesis for Production of Hydrogen Peroxide and Its

Fuel Cells. *Biochim. Biophys. Acta - Bioenerg.* **2016**, *1857* (5), 604–611. https://doi.org/10.1016/j.bbabio.2015.08.012.

(26) Fukuzumi, S.; Yamada, Y.; Karlin, K. D. Hydrogen Peroxide as a Sustainable Energy Carrier: Electrocatalytic Production of Hydrogen Peroxide and the Fuel Cell. *Electrochim. Acta* **2012**, *82*, 493–511. https://doi.org/10.1016/j.electacta.2012.03.132.

(27) Han, Z.; Eisenberg, R. Fuel from Water: The Photochemical Generation of Hydrogen from Water. *Acc. Chem. Res.* **2014**, *47* (8), 2537–2544. https://doi.org/10.1021/ar5001605.

(28) Han, Z.; Shen, L.; Brennessel, W. W.; Holland, P. L.; Eisenberg, R. Nickel Pyridinethiolate Complexes as Catalysts for the Light-Driven Production of Hydrogen from Aqueous Solutions in Noble-Metal-Free Systems. *J. Am. Chem. Soc.* **2013**, *135* (39), 14659–14669. https://doi.org/10.1021/ja405257s.

(29) Virca, C. N.; McCormick, T. M. DFT Analysis into the Intermediates of Nickel Pyridinethiolate Catalysed Proton Reduction. *Dalt. Trans.* **2015**, *44* (32), 14333–14340. https://doi.org/10.1039/C5DT02044A.

(30) Solis, B. H.; Hammes-Schiffer, S. Proton-Coupled Electron Transfer in Molecular Electrocatalysis: Theoretical Methods and Design Principles. *Inorg. Chem.* **2014**, *53* (13), 6427–6443. https://doi.org/10.1021/ic5002896.

(31) Rosenfield, S. G.; Berends, H. P.; Gelmini, L.; Stephan, D. W.; Mascharak, P. K.

New Octahedral Thiolato Complexes of Divalent Nickel: Syntheses, Structures, and Properties of (Et_4N) and (Ph_4P). CH_3CN. *Inorg. Chem.* **1987**, *26* (17), 2792–2797. https://doi.org/10.1021/ic00264a015.

(32) Virca, C. N.; Lohmolder, J. R.; Tsang, J. B.; Davis, M. M.; McCormick, T. M. Effect of Ligand Modification on the Mechanism of Electrocatalytic Hydrogen Production by Ni(Pyridinethiolate)$_3^-$ Derivatives. *J. Phys. Chem. A* **2018**, *122* (11), 3057–3065. https://doi.org/10.1021/acs.jpca.7b11912.

(33) Bäckvall, J. E. *Modern Oxidation Methods*; 2005. https://doi.org/10.1002/9783527632039.

(34) Melone, L.; Punta, C. Metal-Free Aerobic Oxidations Mediated by N-Hydroxyphthalimide. A Concise Review. *Beilstein J. Org. Chem.* **2013**, *9*, 1296–1310. https://doi.org/10.3762/bjoc.9.146.

(35) Recupero, F.; Punta, C. Free Radical Functionalization of Organic Compounds Catalyzed by N-Hydroxyphthalimide. *Chem. Rev.* **2007**, *107* (9), 3800–3842. https://doi.org/10.1021/cr040170k.

(36) Dobras, G.; Sitko, M.; Petroselli, M.; Caruso, M.; Cametti, M.; Punta, C.; Orlińska, B. Solvent-Free Aerobic Oxidation of Ethylbenzene Promoted by NHPI/Co(II) Catalytic System: The Key Role of Ionic Liquids. *ChemCatChem* **2020**, *12* (1), 259–266. https://doi.org/10.1002/cctc.201901737.

(37) Xia, C.; Back, S.; Ringe, S.; Jiang, K.; Chen, F.; Sun, X.; Siahrostami, S.; Chan, K.;

Wang, H. Confined Local Oxygen Gas Promotes Electrochemical Water Oxidation to Hydrogen Peroxide. *Nat. Catal.* **2020**, *3* (2), 125–134. https://doi.org/10.1038/s41929-019-0402-8.

(38) Campos-Martin, J. M.; Blanco-Brieva, G.; Fierro, J. L. G. Hydrogen Peroxide Synthesis: An Outlook beyond the Anthraquinone Process. *Angew. Chemie - Int. Ed.* **2006**, *45* (42), 6962–6984. https://doi.org/10.1002/anie.200503779.

(39) Iwahama, T.; Yoshino, Y.; Keitoku, T.; Sakaguchi, S.; Ishii, Y. Efficient Oxidation of Alcohols to Carbonyl Compounds with Molecular Oxygen Catalyzed by N-Hydroxyphthalimide Combined with a Co Species. *J. Org. Chem.* **2000**, *65* (20), 6502–6507. https://doi.org/10.1021/jo000760s.

(40) Iwahama, T.; Sakaguchi, S.; Ishii, Y. Production of Hydrogen Peroxide via Aerobic Oxidation of Alcohols Catalyzed by N-Hydroxyphthalimide. *Org. Process Res. Dev.* **2000**, *4* (2), 94–97. https://doi.org/10.1021/op990082f.

(41) Merritt, E. A.; Olofsson, B. Diaryliodonium Salts: A Journey from Obscurity to Fame. *Angew. Chemie - Int. Ed.* **2009**, *48* (48), 9052–9070. https://doi.org/10.1002/anie.200904689.

(42) Lanzi, M.; Dherbassy, Q.; Wencel-Delord, J. Cyclic Diaryl λ^3-Bromanes as Original Aryne Precursors. *Angew. Chemie - Int. Ed.* **2021**, *60* (27), 14852–14857. https://doi.org/10.1002/anie.202103625.

(43) Cavallo, G.; Murray, J. S.; Politzer, P.; Pilati, T.; Ursini, M.; Resnati, G. Halogen

Bonding in Hypervalent Iodine and Bromine Derivatives: Halonium Salts. *IUCrJ* **2017**, *4* (Group 17), 411–419. https://doi.org/10.1107/S2052252517004262.

(44) Rountree, E. S.; Mccarthy, B. D.; Dempsey, J. L. Decoding Proton-Coupled Electron Transfer with Potential-pK_a Diagrams: Applications to Catalysis. *Inorg. Chem.* **2019**, *58*, 6647–6658. https://doi.org/10.1021/acs.inorgchem.8b03368.

(45) Mccarthy, B. D.; Dempsey, J. L. Decoding Proton-Coupled Electron Transfer with Potential − pK_a Diagrams. *Inorg. Chem.* **2017**, *56*, 1225–1231. https://doi.org/10.1021/acs.inorgchem.6b02325.

(46) Zarkadoulas, A.; Field, M. J.; Artero, V.; Mitsopoulou, C. A. Proton-Reduction Reaction Catalyzed by Homoleptic Nickel – Bis-1 , 2-Dithiolate Complexes : Experimental and Theoretical Mechanistic Investigations. *ChemCatChem* **2017**, *9*, 2308–2317. https://doi.org/10.1002/cctc.201601399.

(47) Drosou, M.; Zarkadoulas, A.; Bethanis, K.; Mitsopoulou, C. A. Structural Modifications on Nickel Dithiolene Complexes Lead to Increased Metal Participation in the Electrocatalytic Hydrogen Evolution Mechanism. *J. Coord. Chem.* **2021**, *74* (9–10), 1425–1442. https://doi.org/doi.org/10.1080/00958972.2021.1918339.

(48) Drosou, M.; Kamatsos, F.; Mitsopoulou, C. A. Recent Advances in the Mechanisms of the Hydrogen Evolution Reaction by Non-Innocent Sulfur-Coordinating Metal Complexes. *Inorg. Chem. Front.* **2019**, *7* (1), 37–71.

https://doi.org/10.1039/c9qi01113g.

(49) Dai, S.; Funk, L.; Sautner, V.; Paulikat, M.; Uranga, J.; Mata, R.; Tittmann, K. Low-Barrier Hydrogen Bonds in Enzyme Cooperativity. *Nature* **2019**, *573*, 609–613. https://doi.org/10.1038/s41586-019-1581-9.

(50) Gilli, P.; Pretto, L.; Bertolasi, V.; Gilli, G. Predicting Hydrogen-Bond Strengths from Acid-Base Molecular Properties. The pK_a Slide Rule: Toward the Solution of a Long-Lasting Problem. *Acc. Chem. Res.* **2009**, *42* (1), 33–44. https://doi.org/10.1021/ar800001k.

(51) Warshel, A.; Papazyan, A.; Kollman, P. A. On Low-Barrier Hydrogen Bonds and Enzyme Catalysis. *Science (80-.).* **1995**, *269* (5220), 102–106.

(52) Forsyth, W. R.; Antosiewicz, J. M.; Robertson, A. D. Empirical Relationships Between Protein Structure and Carboxyl pK_a Values in Proteins. *Proteins Struct. Funct. Genet.* **2002**, *48*, 388–403. https://doi.org/10.1002/prot.10174.

(53) Cherdo, S.; Ghachtouli, S. El; Sircoglou, M.; Brisset, F.; Orio, M.; Aukauloo, A. A Nickel Dimethyl Glyoximato Complex to Form Nickel Based Nanoparticles for Electrocatalytic H2 Production. *Chem. Commun.* **2014**, *50* (88), 13514–13516. https://doi.org/10.1039/c4cc05355a.

(54) Mondal, B.; Sengupta, K.; Rana, A.; Mahammed, A.; Botoshansky, M.; Dey, S. G.; Gross, Z.; Dey, A. Cobalt Corrole Catalyst for Efficient Hydrogen Evolution Reaction from H_2O under Ambient Conditions : Reactivity, Spectroscopy, and

Density Functional Theory Calculations. *Inorg. Chem.* **2013**, *52*, 3381–3387.

(55) Cramer, C. J.; Truhlar, D. G. Density Functional Theory for Transition Metals and Transition Metal Chemistry. *Phys. Chem. Chem. Phys.* **2009**, *11* (46), 10757–10816. https://doi.org/10.1039/b907148b.

(56) Hammes-Schiffer, S. Catalysts by Design: The Power of Theory. *Acc. Chem. Res.* **2017**, *50* (3), 561–566. https://doi.org/10.1021/acs.accounts.6b00555.

(57) Anson, C. W.; Ghosh, S.; Hammes-Schiffer, S.; Stahl, S. S. Co(Salophen)-Catalyzed Aerobic Oxidation of p-Hydroquinone: Mechanism and Implications for Aerobic Oxidation Catalysis. *J. Am. Chem. Soc.* **2016**, *138* (12), 4186–4193. https://doi.org/10.1021/jacs.6b00254.

(58) Sun, D.; Karippara Harshan, A.; Pécaut, J.; Hammes-Schiffer, S.; Costentin, C.; Artero, V. Hydrogen Evolution Mediated by Cobalt Diimine-Dioxime Complexes: Insights into the Role of the Ligand Acid/Base Functionalities. *ChemElectroChem* **2021**, *8* (14), 2671–2679. https://doi.org/10.1002/celc.202100413.

(59) Guerra, W. D.; Odella, E.; Secor, M.; Goings, J. J.; Urrutia, M. N.; Wadsworth, B. L.; Gervaldo, M.; Sereno, L. E.; Moore, T. A.; Moore, G. F.; Hammes-Schiffer, S.; Moore, A. L. Role of Intact Hydrogen-Bond Networks in Multiproton-Coupled Electron Transfer. *J. Am. Chem. Soc.* **2020**, *142* (52), 21842–21851. https://doi.org/10.1021/jacs.0c10474.

(60) Du, P.; Eisenberg, R. Catalysts Made of Earth-Abundant Elements (Co, Ni, Fe) for

Water Splitting: Recent Progress and Future Challenges. *Energy Environ. Sci.* **2012**, *5* (3), 6012–6021. https://doi.org/10.1039/c2ee03250c.

(61) Hong, D.; Tsukakoshi, Y.; Kotani, H.; Ishizuka, T.; Ohkubo, K.; Shiota, Y.; Yoshizawa, K.; Fukuzumi, S.; Kojima, T. Mechanistic Insights into Homogeneous Electrocatalytic and Photocatalytic Hydrogen Evolution Catalyzed by High-Spin Ni(II) Complexes with S2N2-Type Tetradentate Ligands. *Inorg. Chem.* **2018**, *57* (12), 7180–7190. https://doi.org/10.1021/acs.inorgchem.8b00881.

(62) Inoue, S.; Mitsuhashi, M.; Ono, T.; Yan, Y. N.; Kataoka, Y.; Handa, M.; Kawamoto, T. Photo- and Electrocatalytic Hydrogen Production Using Valence Isomers of N2S2-Type Nickel Complexes. *Inorg. Chem.* **2017**, *56* (20), 12129–12138. https://doi.org/10.1021/acs.inorgchem.7b01244.

(63) Kamatsos, F.; Drosou, M.; Mitsopoulou, C. A. Heteroleptic Thiolate Diamine Nickel Complexes: Noble-Free-Metal Catalysts in Electrocatalytic and Light-Driven Hydrogen Evolution Reaction. *Int. J. Hydrogen Energy* **2021**, *46* (37), 19705–19716. https://doi.org/10.1016/j.ijhydene.2021.02.005.

(64) Race, N. A.; Zhang, W.; Screen, M. E.; Barden, B. A.; McNamara, W. R. Iron Polypyridyl Catalysts Assembled on Metal Oxide Semiconductors for Photocatalytic Hydrogen Generation. *Chem. Commun.* **2018**, *54* (26), 3290–3293. https://doi.org/10.1039/c8cc00453f.

(65) Das, A.; Han, Z.; Brennessel, W. W.; Holland, P. L.; Eisenberg, R. Nickel Complexes

for Robust Light-Driven and Electrocatalytic Hydrogen Production from Water. *ACS Catal.* **2015**, *5* (3), 1397–1406. https://doi.org/10.1021/acscatal.5b00045.

(66) James, T. L.; Cai, L.; Muetterties, M. C.; Holm, R. H. Dihydrogen Evolution by Protonation Reactions of Nickel(I). *Inorg. Chem.* **1996**, *35* (14), 4148–4161.

(67) Han, Z.; Qiu, F.; Eisenberg, R.; Holland, P. L.; Krauss, T. D. Robust Photogeneration of H_2 in Water Using Semiconductor Nanocrystals and a Nickel Catalyst. *Science (80-.).* **2012**, *338*, 1321–1324. https://doi.org/10.1126/science.1227775.

(68) McLaughlin, M. P.; McCormick, T. M.; Eisenberg, R.; Holland, P. L. A Stable Molecular Nickel Catalyst for the Homogeneous Photogeneration of Hydrogen in Aqueous Solution. *Chem. Commun.* **2011**, *47* (28), 7989–7991. https://doi.org/10.1039/c1cc12347e.

(69) Jacques, P. A.; Artero, V.; Pecaut, J.; Fontecave, M. Cobalt and Nickel Diimine-Dioxime Complexes as Molecular Electrocatalysts for Hydrogen Evolution with Low Overvoltages. *Proc. Natl. Acad. Sci.* **2009**, *106* (49), 20627–20632.

(70) Han, Z.; McNamara, W. R.; Eum, M. S.; Holland, P. L.; Eisenberg, R. A Nickel Thiolate Catalyst for the Long-Lived Photocatalytic Production of Hydrogen in a Noble-Metal-Free System. *Angew. Chemie - Int. Ed.* **2012**, *51* (7), 1667–1670. https://doi.org/10.1002/anie.201107329.

(71) McCrory, C. C. L.; Uyeda, C.; Peters, J. C. Electrocatalytic Hydrogen Evolution in Acidic Water with Molecular Cobalt Tetraazamacrocycles. *J. Am. Chem. Soc.* **2012**,

134 (6), 3164–3170. https://doi.org/10.1021/ja210661k.

(72) Clark, A. T.; Smith, K.; Muhandiram, R.; Edmondson, S. P.; Shriver, J. W. Carboxyl pK_a Values, Ion Pairs, Hydrogen Bonding, and the PH-Dependence of Folding the Hyperthermophile Proteins Sac7d and Sso7d. *J. Mol. Biol.* **2007**, *372* (4), 992–1008. https://doi.org/10.1016/j.jmb.2007.06.089.

(73) Bashford, D.; Karplus, M. PK_a of Ionizable Groups in Proteins: Atomic Detail from a Continuum Electrostatic Model. *Biochemistry* **1990**, *29* (44), 10219–10225. https://doi.org/10.1021/bi00496a010.

(74) Isom, D. G.; Castañeda, C. A.; Cannon, B. R.; García-moreno E, B. Large Shifts in pK_a Values of Lysine Residues Buried inside a Protein. *Proc. Natl. Acad. Sci.* **2011**, *108* (13), 5260–5265. https://doi.org/10.1073/pnas.1010750108/-/DCSupplemental.www.pnas.org/cgi/doi/10.1073/pnas.1010750108.

(75) Han, C.; Song, J.; Chan, T.; Pruett, C.; Han, S. Electrostatic Environment of Proteorhodopsin Affects the pK_a of Its Buried Primary Proton Acceptor. *Biophys. J.* **2020**, *118* (8), 1838–1849. https://doi.org/10.1016/j.bpj.2020.02.027.

(76) Shokri, A.; Abedin, A.; Fattahi, A.; Kass, S. R. Effect of Hydrogen Bonds on pK_a Values : Importance of Networking. *J. Am. Chem. Soc.* **2012**, *134*, 10646–10650. https://doi.org/10.1021/ja3037349.

(77) Shokri, A.; Wang, X.; Kass, S. R. Electron-Withdrawing Trifluoromethyl Groups in Combination with Hydrogen Bonds in Polyols: Brønsted Acids, Hydrogen-Bond

Catalysts, and Anion Receptors. *J. Am. Chem. Soc.* **2013**, *135*, 9525–9530. https://doi.org/10.1021/ja4036384.

(78) Kochem, A.; O'Hagan, M.; Wiedner, E. S.; Van Gastel, M. Combined Spectroscopic and Electrochemical Detection of a Ni(I)···H-N Bonding Interaction with Relevance to Electrocatalytic H_2 Production. *Chem. - A Eur. J.* **2015**, *21* (29), 10338–10347. https://doi.org/10.1002/chem.201500954.

(79) Jain, P.; Shukla, R. K.; Pal, S.; Avasare, V. Hydrogen Bonding and Non-Covalent Interaction Assisted Nickel(0) Catalysed Reversible Alkenyl Functional Group Swapping: A Computational Study. *Catal. Sci. Technol.* **2020**, *10* (6), 1747–1760. https://doi.org/10.1039/c9cy02486g.

(80) Frisch, M. J.; Trucks, G. W.; Schlegel, H. B.; Scuseria, G. E.; Robb, M. A.; Cheeseman, J. R.; Scalmani, G.; Barone, V.; Mennucci, B.; Petersson, G. A.; Nakatsuji, H.; Caricato, M.; Li, X.; Hratchian, H. P.; Izmaylov, A. F.; Bloino, J.; Zheng, G.; Sonnenb, D. J. *Gaussian 09*, Revision D.; Gaussian, Inc.: Wallingford CT, 2009.

(81) Marenich, A. V.; Ho, J.; Coote, M. L.; Cramer, C. J.; Truhlar, D. G. Computational Electrochemistry: Prediction of Liquid-Phase Reduction Potentials. *Phys. Chem. Chem. Phys.* **2014**, *16* (29), 15068–15106. https://doi.org/10.1039/c4cp01572j.

(82) Liao, R. Z.; Siegbahn, P. E. M. Quantum Chemical Modeling of Homogeneous Water Oxidation Catalysis. *ChemSusChem* **2017**, *10* (22), 4236–4263.

https://doi.org/10.1002/cssc.201701374.

(83) Himmel, D.; Radtke, V.; Butschke, B.; Krossing, I. Basic Remarks on Acidity. *Angew. Chemie - Int. Ed.* **2018**, *57* (16), 4386–4411. https://doi.org/10.1002/anie.201709057.

(84) Grzelak, I.; Grzelak, Izabela; Orwat, Botosz; Kownacki, Ireneusz; Hoffmann, M. Quantum-Chemical Studies of Homoleptic Iridium(III) Complexes in OLEDs: *Fac* versus *Mer* Isomers. *J. Mol. Model.* **2019**, *25* (154), 1–9.

(85) Bader, R. F. W. A Quantum Theory of Molecular Structure and Its Applications. *Chem. Rev.* **1991**, *91* (5), 893–928. https://doi.org/10.1021/cr00005a013.

(86) Bader, R. F. W. *Atoms in Molecules : A Quantum Theory*; Oxford University Press: USA, 1994.

(87) Lu, T.; Chen, F. Multiwfn: A Multifunctional Wavefunction Analyzer. *J. Comput. Chem.* **2012**, *33* (5), 580–592. https://doi.org/10.1002/jcc.22885.

(88) Espinosa, E.; Molins, E.; Lecomte, C. Hydrogen Bond Strengths Revealed by Topological Analyses of Experimentally Observed Electron Densities. *Chem. Phys. Lett.* **1998**, *285* (3–4), 170–173. https://doi.org/10.1016/S0009-2614(98)00036-0.

(89) Spackman, M. A. Hydrogen Bond Energetics from Topological Analysis of Experimental Electron Densities: Recognising the Importance of the Promolecule. *Chem. Phys. Lett.* **1999**, *301* (5–6), 425–429. https://doi.org/10.1016/S0009-

2614(99)00071-8.

(90) Emamian, S.; Lu, T.; Kruse, H.; Emamian, H. Exploring Nature and Predicting Strength of Hydrogen Bonds: A Correlation Analysis Between Atoms-in-Molecules Descriptors, Binding Energies, and Energy Components of Symmetry-Adapted Perturbation Theory. *J. Comput. Chem.* **2019**, *40* (32), 2868–2881. https://doi.org/10.1002/jcc.26068.

(91) Qi, X.; Liu, L.; Fu, Y.; Guo, Q. Ab Initio Calculations of pK_a Values of Transition-Metal Hydrides in Acetonitrile. *Organometallics* **2006**, *25* (25), 5879–5886.

(92) Addison, A. W.; Rao, T. N.; Reedijk, J.; van Rijn, J.; Verschoor, G. C. Synthesis, Structure, and Spectroscopic Properties of Copper(II) Compounds Containing Nitrogen-Sulphur Donor Ligands; the Crystal and Molecular Structure of Aqua[1,7-Bis(*N*-Methylbenzimidazol-2'-Yl)-2,6-Dithiaheptane]Copper(II). *J. Chem. Soc. Dalt. Trans.* **1984**, *3*, 1349–1356.

(93) Crans, D. C.; Tarlton, M. L.; Mclauchlan, C. C. Trigonal Bipyramidal or Square Pyramidal Coordination Geometry ? Investigating the Most Potent Geometry for Vanadium Phosphatase Inhibitors. *Eur. J. Inorg. Chem.* **2014**, 4450–4468. https://doi.org/10.1002/ejic.201402306.

(94) Peters, J. C.; Harkins, S. B.; Brown, S. D.; Day, M. W. Pincer-like Amido Complexes of Platinum , Palladium , and Nickel. *Inorg. Chem.* **2001**, *40* (11), 5083–5091.

(95) Takaoka, A.; Mankad, N. P.; Peters, J. C. Dinitrogen Complexes of Sulfur-Ligated

Iron. *J. Am. Chem. Soc.* **2011**, *133*, 8440–8443.

(96) Suess, D. L. M.; Peters, J. C. Late-Metal Diphosphinosulfinyl $S(O)P_2$ Pincer-Type Complexes. *Organometallics* **2012**, *31*, 5213–5222.

(97) Sellmann, D.; Gottschalk-Gaudig, T.; Heinemann, F. W. Transition Metal Complexes with Sulfur Ligands . Part CXXVII Azido, Halido and Nitrido Ruthenium Complexes with Sulfur-Rich Coordination Spheres. *Inorganica Chim. Acta* **1998**, *269*, 63–72.

(98) Li, C.; Baek, J. B. Recent Advances in Noble Metal (Pt, Ru, and Ir)-Based Electrocatalysts for Efficient Hydrogen Evolution Reaction. *ACS Omega*. American Chemical Society January 14, 2020, pp 31–40. https://doi.org/10.1021/acsomega.9b03550.

(99) Inoue, S.; Mitsuhashi, M.; Ono, T.; Yan, Y. N.; Kataoka, Y.; Handa, M.; Kawamoto, T. Photo- and Electrocatalytic Hydrogen Production Using Valence Isomers of $N_2S_2^-$ Type Nickel Complexes. *Inorg. Chem.* **2017**, *56* (20), 12129–12138. https://doi.org/10.1021/acs.inorgchem.7b01244.

(100) Bhattacharjee, A.; Brown, D. S. V.; Virca, C. N.; Ethridge, T. E.; Mendez Galue, O.; Pham, U. T.; McCormick, T. M. Computational Investigation into Intramolecular Hydrogen Bonding Controlling the Isomer Formation and p*Ka* of Octahedral Nickel(II) Proton Reduction Catalysts. *Dalt. Trans.* **2022**, *51* (9), 3676–3685. https://doi.org/10.1039/d2dt00043a.

(101) Grzelak, Izabela; Orwat, Botosz; Kownacki, Ireneusz; Hoffmann, M. Quantum-Chemical Studies of Homoleptic Iridium(III)Complexes in OLEDs: *Fac* versus *Mer* Isomers. *J. Mol. Model.* **2019**, *25* (154), 2–9.

(102) Hratchian, H. P.; Keith, T. A.; Millam, J. *Gaussian 05 User's Reference*; 2009.

(103) Kumar, P. S. V.; Raghavendra, V.; Subramanian, V. Bader ' s Theory of Atoms in Molecules (AIM) and Its Applications. **2016**, *128* (10), 1527–1536. https://doi.org/10.1007/s12039-016-1172-3.

(104) Kelly, C. P.; Cramer, C. J.; Truhlar, D. G. Single-Ion Solvation Free Energies and the Normal Hydrogen Electrode Potential in Methanol , Acetonitrile , and Dimethyl Sulfoxide. **2007**, 408–422.

(105) Zhan, C. G.; Dixon, D. A. The Nature and Absolute Hydration Free Energy of the Solvated Electron in Water. *J. Phys. Chem. B* **2003**, *107* (18), 4403–4417. https://doi.org/10.1021/jp022326v.

(106) Grills, D. C.; Lymar, S. V. Solvated Electron in Acetonitrile: Radiation Yield, Absorption Spectrum, and Equilibrium between Cavity- and Solvent-Localized States. *J. Phys. Chem. B* **2022**, *126* (1), 262–269. https://doi.org/10.1021/acs.jpcb.1c08946.

(107) Marković, Z.; Tošović, J.; Milenković, D.; Marković, S. Revisiting the Solvation Enthalpies and Free Energies of the Proton and Electron in Various Solvents. *Comput. Theor. Chem.* **2016**, *1077*, 11–17.

https://doi.org/10.1016/j.comptc.2015.09.007.

(108) McCann, S. D.; Stahl, S. S. Mechanism of Copper/Azodicarboxylate-Catalyzed Aerobic Alcohol Oxidation: Evidence for Uncooperative Catalysis. *J. Am. Chem. Soc.* **2016**, *138* (1), 199–206. https://doi.org/10.1021/jacs.5b09940.

(109) Zhang, W.; Gacs, J.; Arends, I. W. C. E.; Hollmann, F. Selective Photooxidation Reactions Using Water-Soluble Anthraquinone Photocatalysts. *ChemCatChem* **2017**, *9* (20), 3821–3826. https://doi.org/10.1002/cctc.201700779.

(110) Lin, R.; Chen, F.; Jiao, N. Metal-Free, NHPI Catalyzed Oxidative Cleavage of C-C Double Bond Using Molecular Oxygen as Oxidant. *Org. Lett.* **2012**, *14* (16), 4158–4161. https://doi.org/10.1021/ol3018215.

(111) Sterckx, H.; Morel, B.; Maes, B. U. W. Catalytic Aerobic Oxidation of C(Sp3)−H Bonds. *Angew. Chemie - Int. Ed.* **2019**, *58* (24), 7946–7970. https://doi.org/10.1002/anie.201804946.

(112) Liu, J.; Guðmundsson, A.; Bäckvall, J. E. Efficient Aerobic Oxidation of Organic Molecules by Multistep Electron Transfer. *Angew. Chemie - Int. Ed.* **2021**, *60* (29), 15686–15704. https://doi.org/10.1002/anie.202012707.

(113) Huang, Z.; Shanmugam, M.; Liu, Z.; Brook, A.; Bennett, E. L.; Guan, R.; Herrera, D. E. V.; Lopez-sanchez, J. A.; Slater, A. G.; Mcinnes, E. J. L. Chemical Recycling of Polystyrene to Valuable Chemicals via Selective Acid-Catalyzed Aerobic Oxidation under Visible Light. **2022**. https://doi.org/10.1021/jacs.2c01410.

(114) Fukuzumi, S.; Lee, Y. M.; Nam, W. Solar-Driven Production of Hydrogen Peroxide from Water and Dioxygen. *Chem. - A Eur. J.* **2018**, *24* (20), 5016–5031. https://doi.org/10.1002/chem.201704512.

(115) Chang, Q.; Zhang, P.; Mostaghimi, A. H. B.; Zhao, X.; Denny, S. R.; Lee, J. H.; Gao, H.; Zhang, Y.; Xin, H. L.; Siahrostami, S.; Chen, J. G.; Chen, Z. Promoting H_2O_2 Production via 2-Electron Oxygen Reduction by Coordinating Partially Oxidized Pd with Defect Carbon. *Nat. Commun.* **2020**, *11* (1), 1–9. https://doi.org/10.1038/s41467-020-15843-3.

(116) Kofuji, Y.; Ohkita, S.; Shiraishi, Y.; Sakamoto, H.; Tanaka, S.; Ichikawa, S.; Hirai, T. Graphitic Carbon Nitride Doped with Biphenyl Diimide: Efficient Photocatalyst for Hydrogen Peroxide Production from Water and Molecular Oxygen by Sunlight. *ACS Catal.* **2016**, *6* (10), 7021–7029. https://doi.org/10.1021/acscatal.6b02367.

(117) Kofuji, Y.; Isobe, Y.; Shiraishi, Y.; Sakamoto, H.; Tanaka, S.; Ichikawa, S.; Hirai, T. Carbon Nitride-Aromatic Diimide-Graphene Nanohybrids: Metal-Free Photocatalysts for Solar-to-Hydrogen Peroxide Energy Conversion with 0.2% Efficiency. *J. Am. Chem. Soc.* **2016**, *138* (31), 10019–10025. https://doi.org/10.1021/jacs.6b05806.

(118) Kofuji, Y.; Ohkita, S.; Shiraishi, Y.; Sakamoto, H.; Ichikawa, S.; Tanaka, S.; Hirai, T. Mellitic Triimide-Doped Carbon Nitride as Sunlight-Driven Photocatalysts for Hydrogen Peroxide Production. *ACS Sustain. Chem. Eng.* **2017**, *5* (8), 6478–6485. https://doi.org/10.1021/acssuschemeng.7b00575.

(119) Kofuji, Y.; Isobe, Y.; Shiraishi, Y.; Sakamoto, H.; Ichikawa, S.; Tanaka, S.; Hirai, T. Hydrogen Peroxide Production on a Carbon Nitride–Boron Nitride-Reduced Graphene Oxide Hybrid Photocatalyst under Visible Light. *ChemCatChem* **2018**, *10* (9), 2070–2077. https://doi.org/10.1002/cctc.201701683.

(120) Shiraishi, Y.; Kanazawa, S.; Kofuji, Y.; Sakamoto, H.; Ichikawa, S.; Tanaka, S.; Hirai, T. Sunlight-Driven Hydrogen Peroxide Production from Water and Molecular Oxygen by Metal-Free Photocatalysts. *Angew. Chemie - Int. Ed.* **2014**, *53* (49), 13454–13459. https://doi.org/10.1002/anie.201407938.

(121) Nikitas, N. F.; Tzaras, D. I.; Triandafillidi, I.; Kokotos, C. G. Photochemical Oxidation of Benzylic Primary and Secondary Alcohols Utilizing Air as the Oxidant. *Green Chem.* **2020**, *22* (2), 471–477. https://doi.org/10.1039/c9gc03000j.

(122) Amorati, R.; Lucarini, M.; Mugnaini, V.; Pedulli, G. F.; Minisci, F.; Recupero, F.; Fontana, F.; Astolfi, P.; Greci, L. Hydroxylamines as Oxidation Catalysts: Thermochemical and Kinetic Studies. *J. Org. Chem.* **2003**, *68* (5), 1747–1754. https://doi.org/10.1021/jo026660z.

(123) Yang, C.; Farmer, L. A.; Pratt, D. A.; Maldonado, S.; Stephenson, C. R. J. Mechanism of Electrochemical Generation and Decomposition of Phthalimide-N-Oxyl. *J. Am. Chem. Soc.* **2021**, *143* (27), 10324–10332. https://doi.org/10.1021/jacs.1c04181.

(124) Ingold, K. U.; Pratt, D. A. Advances in Radical-Trapping Antioxidant Chemistry in

the 21st Century: A Kinetics and Mechanisms Perspective. *Chem. Rev.* **2014**, *114* (18), 9022–9046. https://doi.org/10.1021/cr500226n.

(125) Zhao, G.; Hu, B.; Busser, G. W.; Peng, B.; Muhler, M. Photocatalytic Oxidation of α-C−H Bonds in Unsaturated Hydrocarbons through a Radical Pathway Induced by a Molecular Cocatalyst. *ChemSusChem* **2019**, *12* (12), 2795–2801. https://doi.org/10.1002/cssc.201900394.

(126) Li, F.; Tang, S.; Tang, Z.; Ye, L.; Li, H.; Niu, F.; Sun, X. Synergistic Catalytic Effect of N-Hydroxyphthalimide/Cobalt Tetraamide Phthalocyanine and Its Application for Aerobic Oxidation of Hydrocarbons and Alcohols. *Catal. Letters* **2021**, *151* (1), 17–26. https://doi.org/10.1007/s10562-020-03283-z.

(127) Zhang, M. Z.; Tian, J.; Yuan, M.; Peng, W. Q.; Wang, Y. Z.; Wang, P.; Liu, L.; Gou, Q.; Huang, H.; Chen, T. Visible Light-Induced Aerobic Dioxygenation of α,β-Unsaturated Amides/Alkenes toward Selective Synthesis of β-Oxy Alcohols Using Rose Bengal as a Photosensitizer. *Org. Chem. Front.* **2021**, *8* (10), 2215–2223. https://doi.org/10.1039/d1qo00149c.

(128) Fukuzumi, S.; Ohkubo, K. Selective Photocatalytic Reactions with Organic Photocatalysts. **2013**, 561–574. https://doi.org/10.1039/c2sc21449k.

(129) Ohzu, S.; Ishizuka, T.; Hirai, Y.; Fukuzumi, S.; Kojima, T. Photocatalytic Oxidation of Organic Compounds in Water by Using Ruthenium(II)-Pyridylamine Complexes as Catalysts with High Efficiency and Selectivity. *Chem. - A Eur. J.* **2013**, *19* (5),

1563–1567. https://doi.org/10.1002/chem.201203430.

(130) Matsubara, C.; Kawamoto, N.; Takamura, K. Oxo[5, 10, 15, 20-Tetra(4-Pyridyl)Porphyrinato]Titanium(IV): An Ultra-High Sensitivity Spectrophotometric Reagent for Hydrogen Peroxide. *Analyst* **1992**, *117* (11), 1781–1784. https://doi.org/10.1039/AN9921701781.

(131) Roderick, W. R.; Brown, W. G. Colorless and Yellow Forms of N-Hydroxyphthalimide. *J. Am. Chem. Soc.* **1957**, *79* (19), 5196–5198. https://doi.org/10.1021/ja01576a033.

(132) Kuriyama, M.; Hanazawa, N.; Abe, Y.; Katagiri, K.; Ono, S.; Yamamoto, K.; Onomura, O. N - And O -Arylation of Pyridin-2-Ones with Diaryliodonium Salts: Base-Dependent Orthogonal Selectivity under Metal-Free Conditions. *Chem. Sci.* **2020**, *11* (31), 8295–8300. https://doi.org/10.1039/d0sc02516j.

(133) Yoshida, Y.; Mino, T.; Sakamoto, M. Chiral Hypervalent Bromine(III) (Bromonium Salt): Hydrogen- And Halogen-Bonding Bifunctional Asymmetric Catalysis by Diaryl-λ^3-Bromanes. *ACS Catal.* **2021**, *11* (21), 13028–13033. https://doi.org/10.1021/acscatal.1c04070.

(134) Lanzi, M.; Ali Abdine, R. A.; De Abreu, M.; Wencel-Delord, J. Cyclic Diaryl Λ3-Bromanes: A Rapid Access to Molecular Complexity via Cycloaddition Reactions. *Org. Lett.* **2021**, *23* (23), 9047–9052. https://doi.org/10.1021/acs.orglett.1c03278.

(135) Nakajima, M.; Miyamoto, K.; Hirano, K.; Uchiyama, M. Diaryl-λ^3-Chloranes:

Versatile Synthesis and Unique Reactivity as Aryl Cation Equivalent. *J. Am. Chem. Soc.* **2019**, *141* (16), 6499–6503. https://doi.org/10.1021/jacs.9b02436.

(136) Miyamoto, K.; Uchiyama, M. Hypervalent Organo-λ^3-Chloranes. *Chem. Lett.* **2021**, *50* (4), 832–838. https://doi.org/10.1246/CL.200849.

(137) Wirth, T. *Topics in Current Chemistry: Hypervalent Iodine Chemistry*, 373rd ed.; Springer UK: Cardiff, 2016. https://doi.org/10.1002/9783527809080.cataz08689.

(138) Sundalam, S. K.; Nilova, A.; Seidl, T. L.; Stuart, D. R. A Selective C−H Deprotonation Strategy to Access Functionalized Arynes by Using Hypervalent Iodine. *Angew. Chemie - Int. Ed.* **2016**, *55* (29), 8431–8434. https://doi.org/10.1002/anie.201603222.

(139) Nilova, A.; Sibbald, P. A.; Valente, E. J.; González-Montiel, G. A.; Richardson, H. C.; Brown, K. S.; Cheong, P. H. Y.; Stuart, D. R. Regioselective Synthesis of 1,2,3,4-Tetrasubstituted Arenes by Vicinal Functionalization of Arynes Derived from Aryl(Mes)Iodonium Salts. *Chem. - A Eur. J.* **2021**, 7168–7175. https://doi.org/10.1002/chem.202100201.

(140) Nilova, A.; Metze, B.; Stuart, D. R. Aryl(TMP)Iodonium Tosylate Reagents as a Strategic Entry Point to Diverse Aryl Intermediates: Selective Access to Arynes. *Org. Lett.* **2021**, *23* (12), 4813–4817. https://doi.org/10.1021/acs.orglett.1c01534.

(141) Braida, B.; Ribeyre, T.; Hiberty, P. C. A Valence Bond Model for Electron-Rich Hypervalent Species: Application to SF_n (N=1, 2, 4), PF_5, and ClF_3. *Chem. - A Eur.*

J. **2014**, *20* (31), 9643–9649. https://doi.org/10.1002/chem.201402755.

(142) Rundle, R. E. Electron Deficient Compounds. *J. Phys. Chem.* **1957**, *61* (1), 45–50. https://doi.org/10.1021/j150547a010.

(143) Rundle, R. E. On the Probable Structure of XeF, and XeF_2. *J. Chem. Phys* **1951**, *19* (407), 446.

(144) Cleveland, T.; Landis, C. R. Valence Bond Concepts Applied to the Molecular Mechanics Description of Molecular Shapes: Application to Hypervalent Molecules of the P-Block. *J. Am. Chem. Soc.* **1996**, *118*, 6020–6030. https://doi.org/10.1021/ja002586v.

(145) Bauer, A.; Maulide, N. Recent Discoveries on the Structure of Iodine(III) Reagents and Their Use in Cross-Nucleophile Coupling. *Chem. Sci.* **2021**, *12* (3), 853–864. https://doi.org/10.1039/d0sc03266b.

(146) Bhandary, S.; Sirohiwal, A.; Kadu, R.; Kumar, S.; Chopra, D. Dispersion Stabilized Se/Te···π Double Chalcogen Bonding Synthons in in Situ Cryocrystallized Divalent Organochalcogen Liquids. *Cryst. Growth Des.* **2018**, *18* (7), 3734–3739. https://doi.org/10.1021/acs.cgd.8b00585.

(147) Dey, A.; Desiraju, G. R. Correlation between Molecular Dipole Moment and Centrosymmetry in Some Crystalline Diphenyl Ethers. *Chem. Commun.* **2005**, No. 19, 2486–2488. https://doi.org/10.1039/b502516h.

(148) Choudhury, A. R.; Islam, K.; Kirchner, M. T.; Mehta, G.; Row, T. N. G. In Situ Cryocrystallization of Diphenyl Ether: C-H···π Mediated Polymorphic Forms. *J. Am. Chem. Soc.* **2004**, *126* (39), 12274–12275. https://doi.org/10.1021/ja046134k.

(149) Cox, P. J.; Wardell, J. L. Studies of Polymorphism in Three Compounds by Single Crystal X-Ray Diffraction. *Int. J. Pharm.* **2000**, *194* (2), 147–153. https://doi.org/10.1016/S0378-5173(99)00364-6.

(150) Countryman, N. W. A. and R. M. Secondary Bonding. Part I. Crystal and Molecular Structures of $(C_6H_5)_2$ IX (X = Cl, Br, or I). *J. Chem. Soc. Dalt. Trans.* **1977**, 217–219.

(151) Pauling, L. The Nature of Chemical Bond. Application of Results Obtained From the Quantum Mechanics and From the Theory of Paramagnetic Susceptibility to the Structure of Molecules. *J. Am. Chem. Soc.* **1931**, *53*, 1367–1400.

(152) Sini, G.; Maitre, P.; Hiberty, P. C. Covalent, Ionic and Resonating Single Bonds. *J. Mol. Struct. (Theochem),* **1991**, *229*, 163–188.

(153) Bent, H. A. An Appraisal of Valence-Bond Structures and Hybridization in Compounds of the First-Row Elements. *Chem. Rev.* **1960**, *60*, 275–311.

(154) Becke, A. D. Density-Functional Exchange-Energy Approximation with Correct Asymptotic Behavior. *Phys. Rev. A* **1988**, *38* (6), 3098–3100.

(155) Miehlich, Burkhard; Savin, Andreas; Stoll, Hermann; Preuss, H. Results Obtained

with the Correlation Energy Density Functionals of Becke and Lee, Yang and Parr. *Chem. Phys. lett.* **1989**, *157* (3), 200–206.

(156) Marenich, A. V.; Jerome, S. V.; Cramer, C. J.; Truhlar, D. G. Charge Model 5: An Extension of Hirshfeld Population Analysis for the Accurate Description of Molecular Interactions in Gaseous and Condensed Phases. *J. Chem. Theory Comput.* **2012**, *8* (2), 527–541. https://doi.org/10.1021/ct200866d.

(157) R. M. Dreizler, E. K. U. G. *Density Functional Theory: An Approach to the Quantum Many-Body Problem*; Springer-Verlag, 1990.

(158) Siahrostami, S.; Villegas, S. J.; Bagherzadeh Mostaghimi, A. H.; Back, S.; Farimani, A. B.; Wang, H.; Persson, K. A.; Montoya, J. A Review on Challenges and Successes in Atomic-Scale Design of Catalysts for Electrochemical Synthesis of Hydrogen Peroxide. *ACS Catal.* **2020**, *10* (14), 7495–7511. https://doi.org/10.1021/acscatal.0c01641.

(159) Feynman, Richard P., Leighton, Robert B., Sands, M. *Feynman's Lectures on Physics*; Addison-Wesley, 1963.

(160) Box, G. E. P. Science and Statistics. *J. Am. Stat. Assoc.* **1976**, *71* (356), 791–799. https://doi.org/10.1080/01621459.1976.10480949.

APPENDIX Computationally derived structure parameters and topology maps

Appendix Table 1. Single point energies (in a.u.) of the starting catalysts at different spin states (singlet and triplet) using different functionals (B3LYP, B3P86, and M11-L) and 6-311+g(2df,2pd) basis sets in gas phase.

	Single point Energy (a.u.)					
	B3LYP		B3P86		M11-L	
	Singlet	Triplet	Singlet	Triplet	Singlet	Triplet
$[Ni(L1)_3]^-$	-3446.4713	-3446.4907	-3450.2148	-3450.2333	-3446.3773	-3446.3936
$[Ni(L2)_3]^-$	-4457.9704	-4457.9942	-4463.3839	-4463.4066	-4457.5641	-4457.5832
$[Ni(L3)_3]^-$	-4457.9881	-4458.0114	-4463.3998	-4463.4222	-4457.5753	-4457.5940
$[Ni(L4)_3]^-$	-4012.4289	-4012.4469	-4017.3341	-4017.3510	-4012.1822	-4012.1963
$[Ni(L5)_3]^-$	-4012.3832	-4012.4655	-4017.2892	-4017.3752	-4012.1388	-4012.2104
$[Ni(L6)_3]^-$	-4825.3524	-4825.3756	-4830.0155	-4830.0379	-4825.1749	-4825.1942
$[Ni(L7)_3]^-$ (*fac*)	-3564.4603	-3564.4799	-3568.6444	-3568.6565	-3564.3476	-3564.3700

Appendix Table 2. Gas phase single point energies (in a.u.) of the computationally modeled *fac* and *mer*- isomers of five substituted **[Ni(PyS)$_3$]$^-$** catalysts in both singlet and triplet spin states.

Single point Energy (a.u.)

	fac		*mer*	
	Singlet	Triplet	Singlet	Triplet
[Ni(L8)$_3$]$^-$	-4463.3715	-4463.3855	-4463.3614	-4463.3853
[Ni(L9)$_3$]$^-$	-4463.3909	-4463.4115	-4463.3956	-4463.4158
[Ni(L10)$_3$]$^-$	-3568.6441	-3568.6657	-3568.6501	-3568.6696
[Ni(L11)$_3$]$^-$	-3568.6362	-3568.6554	-3568.6424	-3568.6601
[Ni(L12)$_3$]$^-$	-3568.6418	-3568.6615	-3568.6479	-3568.6658

Appendix Table 3. Comparison of the different Ni-N and Ni-S bond lengths (in Å) between the X-ray structure and computationally modeled structures (in gas and water solvated phases) of tris(pyridinethiolato)nickel (II), (**[Ni(L1)$_3$]$^-$**).

	Bond length (Å)			**% Error**	
	B3P86/6-311+G(2df,2pd)		X-ray		
	Gas	Water		Gas	Water
Ni-N1	2.049	2.055	2.034 (4)	0.74	1.03
Ni-N2	2.054	2.051	2.041 (4)	0.64	0.49
Ni-N3	2.079	2.071	2.081 (4)	0.10	0.48
Ni-S1	2.540	2.534	2.541 (1)	0.04	0.28
Ni-S2	2.503	2.543	2.526 (1)	0.91	0.67
Ni-S3	2.537	2.533	2.518 (1)	0.75	0.60

Appendix Table 4. Ni-N and Ni-S bond distances (in Å) of the computationally modeled starting catalysts in water solvated phase.

	Ni-N bond length (Å)			**Ni-S bond length (Å)**		
	$Ni\text{-}N_C$	**$Ni\text{-}N_L$**	**$Ni\text{-}N_R$**	**$Ni\text{-}S_C$**	**$Ni\text{-}S_L$**	**$Ni\text{-}S_R$**
$[Ni(L1)_3]^-$	2.071	2.055	2.051	2.533	2.534	2.543
$[Ni(L2)_3]^-$	2.076	2.056	2.055	2.507	2.510	2.508
$[Ni(L3)_3]^-$	2.073	2.056	2.056	2.518	2.522	2.520
$[Ni(L4)_3]^-$	2.073	2.056	2.054	2.518	2.519	2.509
$[Ni(L5)_3]^-$	2.057	2.043	2.042	2.515	2.512	2.528
$[Ni(L6)_3]^-$	2.077	2.058	2.057	2.521	2.522	2.520
$[Ni(L7)_3]^-$ (*fac*)*	2.119	2.116	2.118	2.495	2.496	2.496
$[Ni(L8)_3]^-$ (*fac*)*	2.193	2.204	2.211	2.427	2.427	2.427
$[Ni(L9)_3]^-$	2.072	2.057	2.054	2.521	2.520	2.522
$[Ni(L10)_3]^-$	2.073	2.056	2.051	2.531	2.526	2.545
$[Ni(L11)_3]^-$	2.071	2.055	2.051	2.540	2.538	2.548
$[Ni(L12)_3]^-$	2.069	2.053	2.049	2.540	2.539	2.554

***For the *fac* complexes **$[Ni(L7)_3]^-$** and **$[Ni(L8)_3]^-$**, all three **Ni-N** bonds are equivalent.

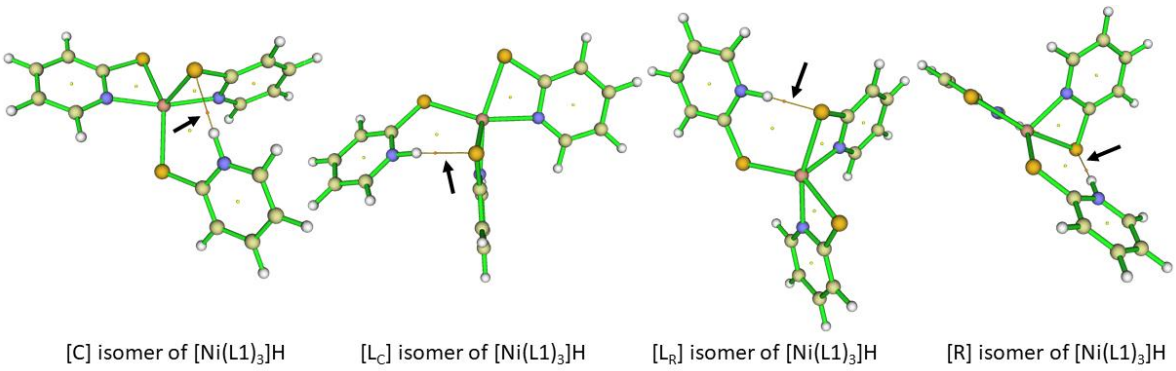

Appendix Figure 1. Topology maps of the computationally modeled protonated intermediates (1-H) for **[Ni(L1)$_3$]H** represented using ball-stick drawing method. Blue, White, Light Yellow, Dark Yellow, Pink, and cyan balls represent N, H, C, S, Ni, and F atoms, respectively. Yellow lines are the bond paths. Black arrows point toward the intramolecular H-bonding interaction stabilizing the structure.

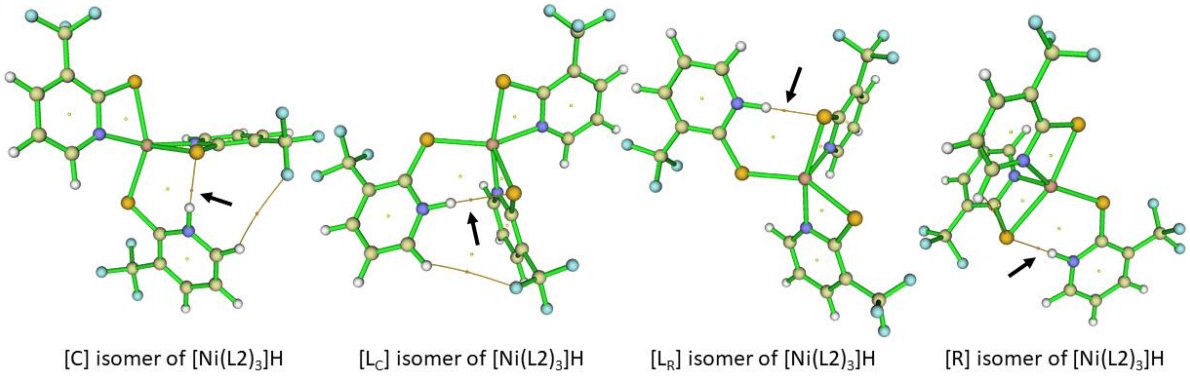

Appendix Figure 2. Topology maps of the computationally modeled protonated intermediates (1-H) for **[Ni(L2)$_3$]H** represented using ball-stick drawing method. Blue, White, Light Yellow, Dark Yellow, Pink, and cyan balls represent N, H, C, S, Ni, and F atoms respectively. Yellow lines are the bond paths. Black arrows point toward the intramolecular H-bonding interaction stabilizing the structure.

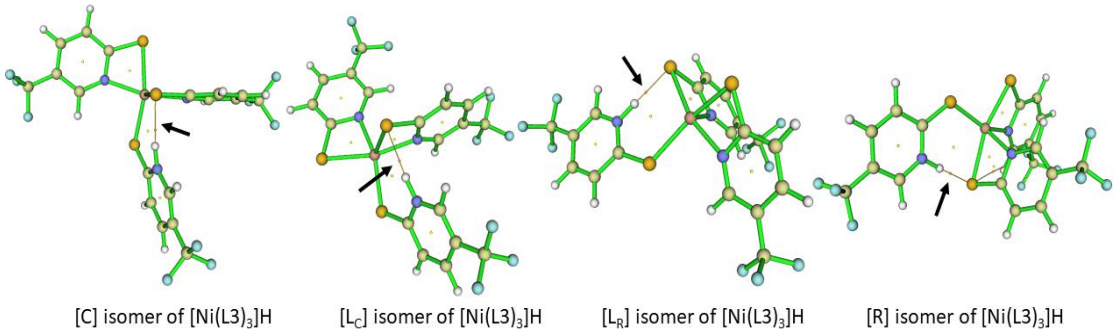

Appendix Figure 3. Topology maps of the computationally modeled protonated intermediates (1-H) for **[Ni(L3)$_3$]H** represented using ball-stick drawing method. Blue, White, Light Yellow, Dark Yellow, Pink, and cyan balls represent N, H, C, S, Ni, and F atoms, respectively. Yellow lines are the bond paths. Black arrows point toward the intramolecular H-bonding interaction stabilizing the structure.

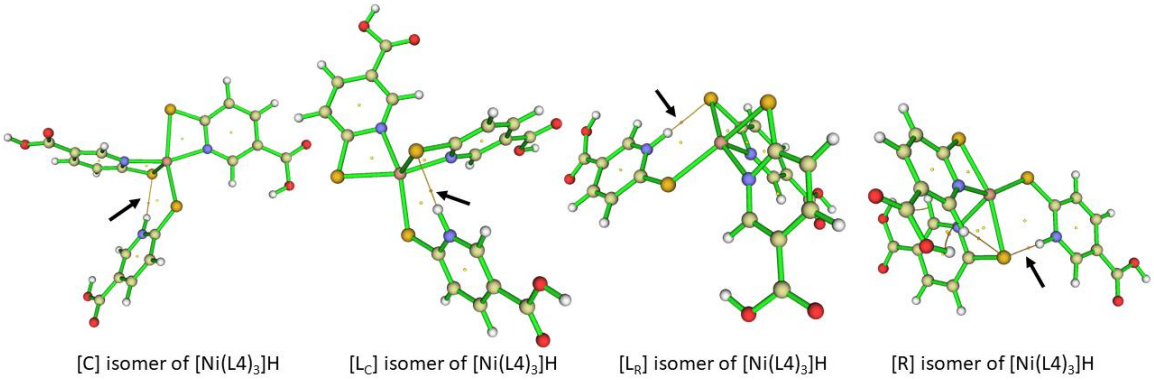

Appendix Figure 4. Topology maps of the computationally modeled protonated intermediates (1-H) for **[Ni(L4)$_3$]H** represented using ball-stick drawing method. Blue, White, Light Yellow, Dark Yellow, Pink, and Red balls represent N, H, C, S, Ni, and O atoms, respectively. Yellow lines are the bond paths. Black arrows point toward the intramolecular hydrogen bonding interaction stabilizing the structure.

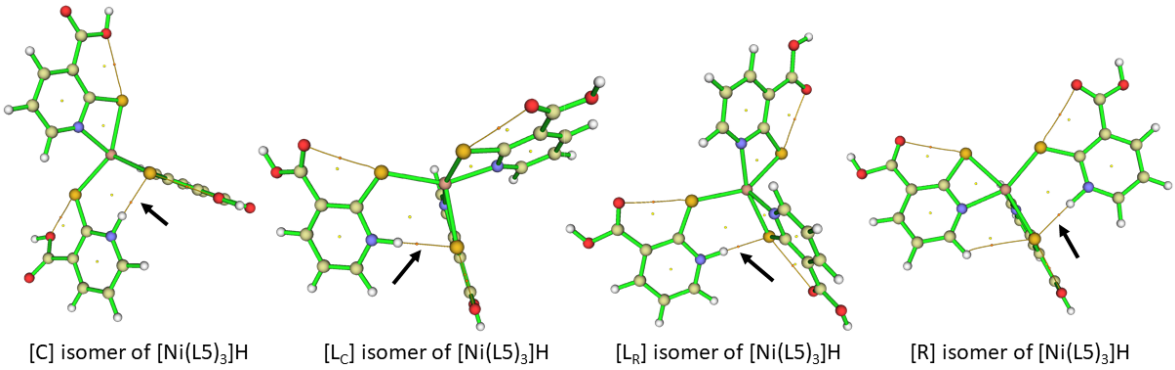

Appendix Figure 5. Topology maps of the computationally modeled protonated intermediates (1-H) for **[Ni(L5)$_3$]H** represented using ball-stick drawing method. Blue, White, Light Yellow, Dark Yellow, Pink, and Red balls represent N, H, C, S, Ni, and O atoms, respectively. Yellow lines are the bond paths. Black arrows point toward the intramolecular hydrogen bonding interaction stabilizing the structure.

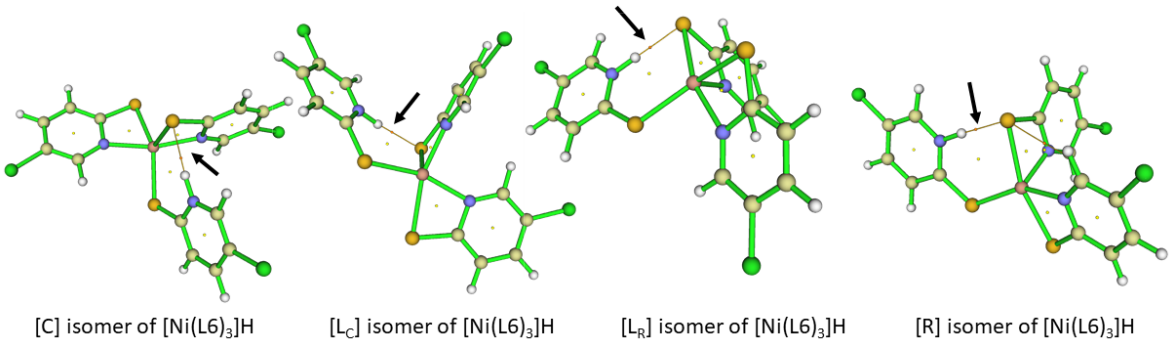

Appendix Figure 6. Topology maps of the computationally modeled protonated intermediates (1-H) for **[Ni(L6)$_3$]H** represented using ball-stick drawing method. Blue, White, Light Yellow, Dark Yellow, Pink, and Green balls represent N, H, C, S, Ni, and Cl atoms, respectively. Yellow lines are the bond paths. Black arrows point toward the intramolecular hydrogen bonding interaction stabilizing the structure.

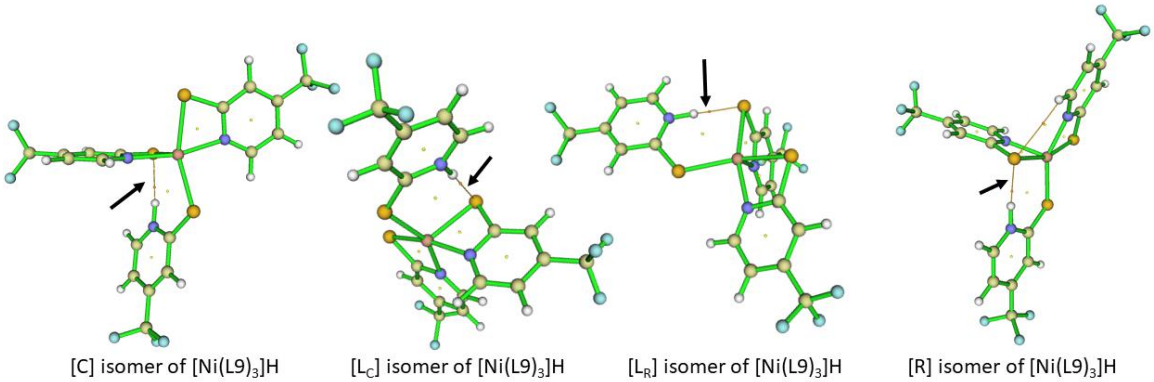

Appendix Figure 7. Topology maps of the computationally modeled protonated intermediates (1-H) for **[Ni(L9)$_3$]H** represented using ball-stick drawing method. Blue, White, Light Yellow, Dark Yellow, Pink, and cyan balls represent N, H, C, S, Ni, and F atoms, respectively. Yellow lines are the bond paths. Black arrows point toward the intramolecular hydrogen bonding interaction stabilizing the structure.

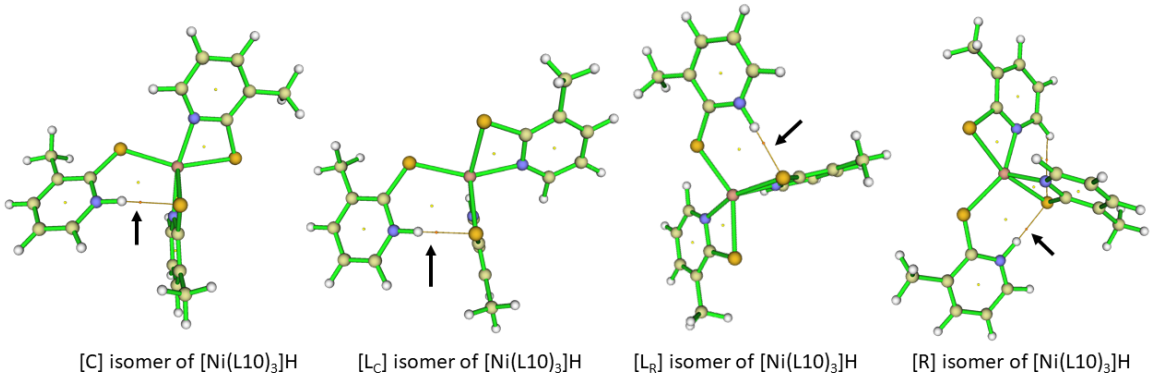

Appendix Figure 8. Topology maps of the computationally modeled protonated intermediates (1-H) for **[Ni(L10)$_3$]H** represented using ball-stick drawing method. Blue, White, Light Yellow, Dark Yellow, and Pink balls represent N, H, C, S, and Ni atoms, respectively. Yellow lines are the bond paths. Black arrows point toward the intramolecular hydrogen bonding interaction stabilizing the structure.

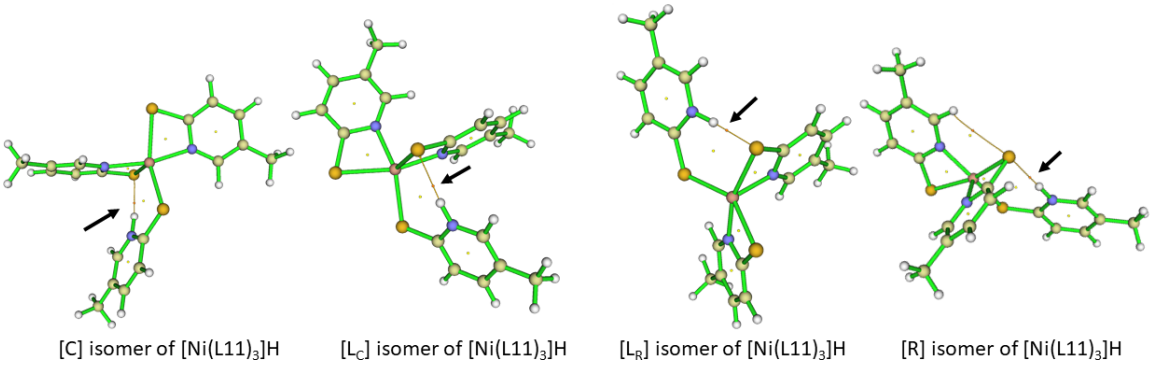

Appendix Figure 9. Topology maps of the computationally modeled protonated intermediates (1-H) for **[Ni(L11)$_3$]H** represented using ball-stick drawing method. Blue, White, Light Yellow, Dark Yellow, and Pink balls represent N, H, C, S, and Ni atoms, respectively. Yellow lines are the bond paths. Black arrows point toward the intramolecular hydrogen bonding interaction stabilizing the structure.

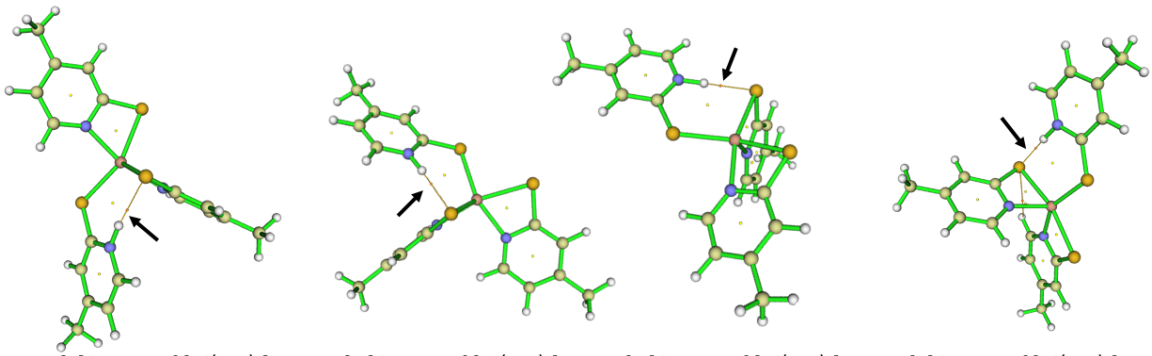

Appendix Figure 10. Topology maps of the computationally modeled protonated intermediates (1-H) for **[Ni(L12)$_3$]H** represented using ball-stick drawing method. Blue, White, Light Yellow, Dark Yellow, and Pink balls represent N, H, C, S, and Ni atoms, respectively. Yellow lines are the bond paths. Black arrows point toward the intramolecular hydrogen bonding interaction stabilizing the structure.

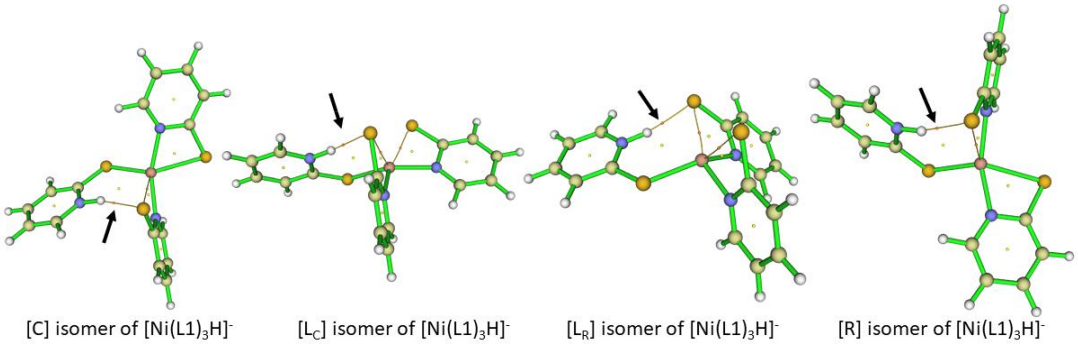

Appendix Figure 11. Topology maps of the computationally modeled reduced intermediates (1-H^-) for **$[Ni(L1)_3]H^-$** represented using ball-stick drawing method. Blue, White, Light Yellow, Dark Yellow, and Pink balls represent N, H, C, S, and Ni atoms, respectively. Yellow lines are the bond paths. Black arrows point toward the intramolecular hydrogen bonding interaction stabilizing the structure.

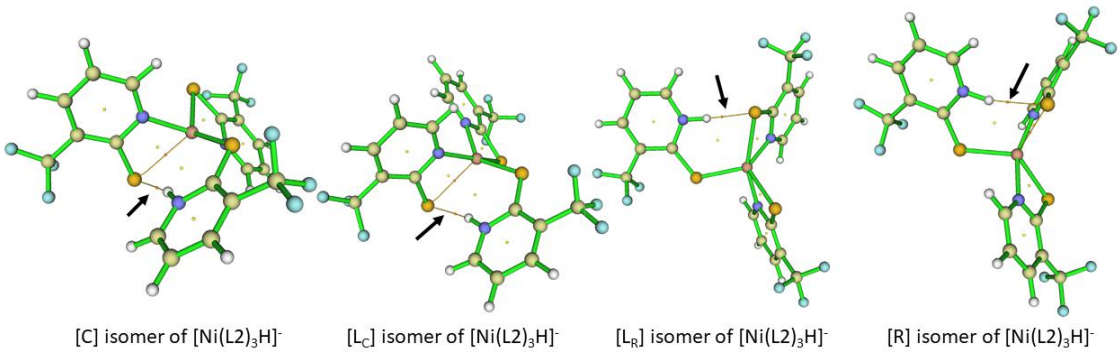

Appendix Figure 12. Topology maps of the computationally modeled reduced intermediates (1-H^-) for **$[Ni(L2)_3]H^-$** represented using ball-stick drawing method. Blue, White, Light Yellow, Dark Yellow, Pink, and cyan balls represent N, H, C, S, Ni, and F atoms, respectively. Yellow lines are the bond paths. Black arrows point toward the intramolecular hydrogen bonding interaction stabilizing the structure.

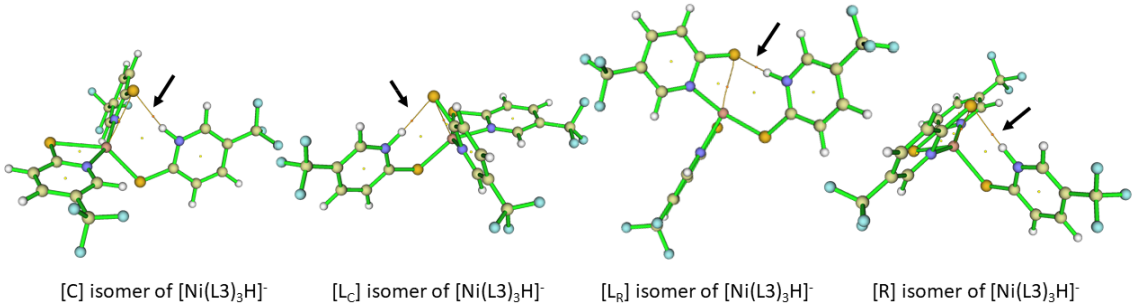

Appendix Figure 13. Topology maps of the computationally modeled reduced intermediates (1-H^-) for **$[Ni(L3)_3]H^-$** represented using ball-stick drawing method. Blue, White, Light Yellow, Dark Yellow, Pink, and cyan balls represent N, H, C, S, Ni, and F atoms, respectively. Yellow lines are the bond paths. Black arrows point toward the intramolecular hydrogen bonding interaction stabilizing the structure.

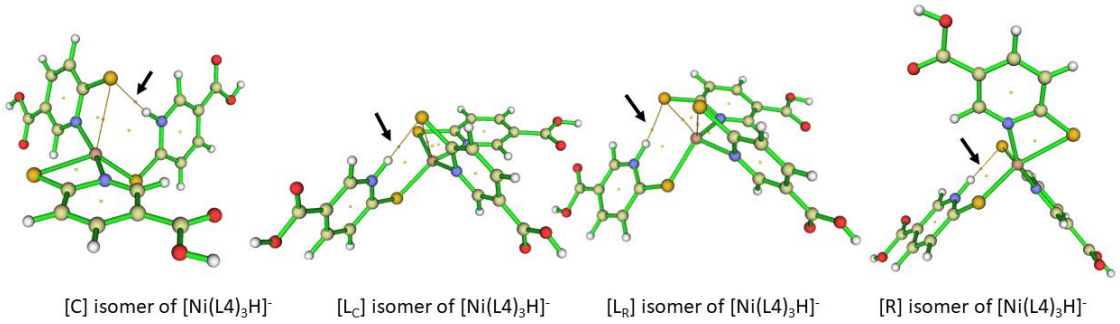

Appendix Figure 14. Topology maps of the computationally modeled protonated intermediates (1-H$^-$) for **[Ni(L4)$_3$]H$^-$** represented using ball-stick drawing method. Blue, White, Light Yellow, Dark Yellow, Pink, and Red balls represent N, H, C, S, Ni, and O atoms, respectively. Yellow lines are the bond paths. Black arrows point toward the intramolecular hydrogen bonding interaction stabilizing the structure.

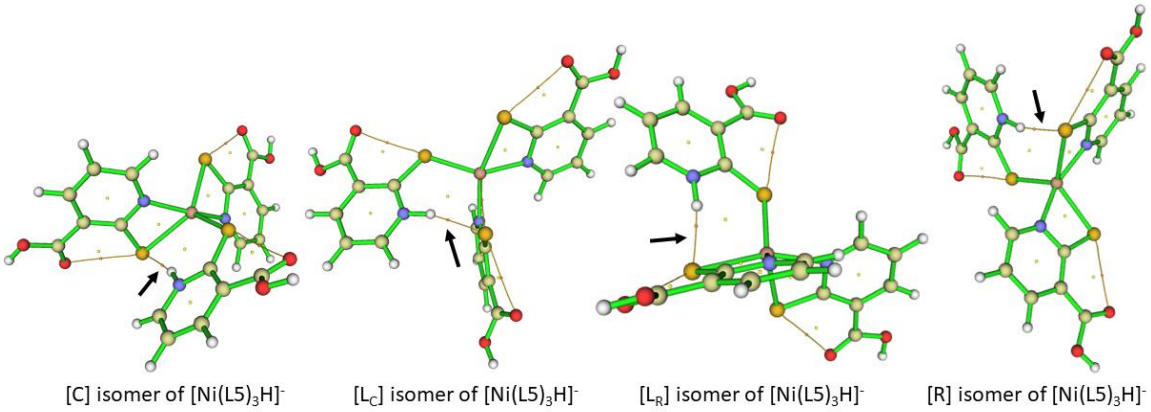

Appendix Figure 15. Topology maps of the computationally modeled protonated intermediates (1-H^-) for **[Ni(L5)$_3$]H$^-$** represented using ball-stick drawing method. Blue, White, Light Yellow, Dark Yellow, Pink, and Red balls represent N, H, C, S, Ni, and O atoms, respectively. Yellow lines are the bond paths. Black arrows point toward the intramolecular hydrogen bonding interaction stabilizing the structure.

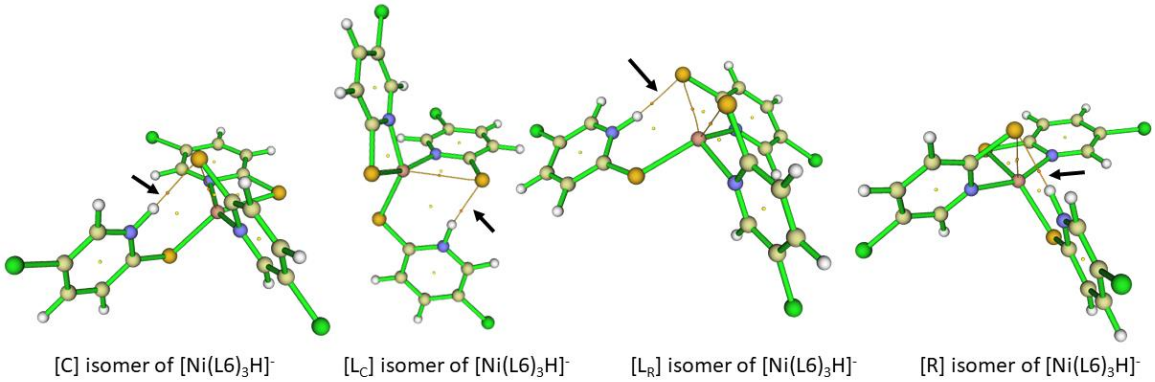

Appendix Figure 16. Topology maps of the computationally modeled protonated intermediates (1-H^-) for **$[Ni(L6)_3]H^-$** represented using ball-stick drawing method. Blue, White, Light Yellow, Dark Yellow, Pink, and Green balls represent N, H, C, S, Ni, and Cl atoms, respectively. Yellow lines are the bond paths. Black arrows point toward the intramolecular hydrogen bonding interaction stabilizing the structure.

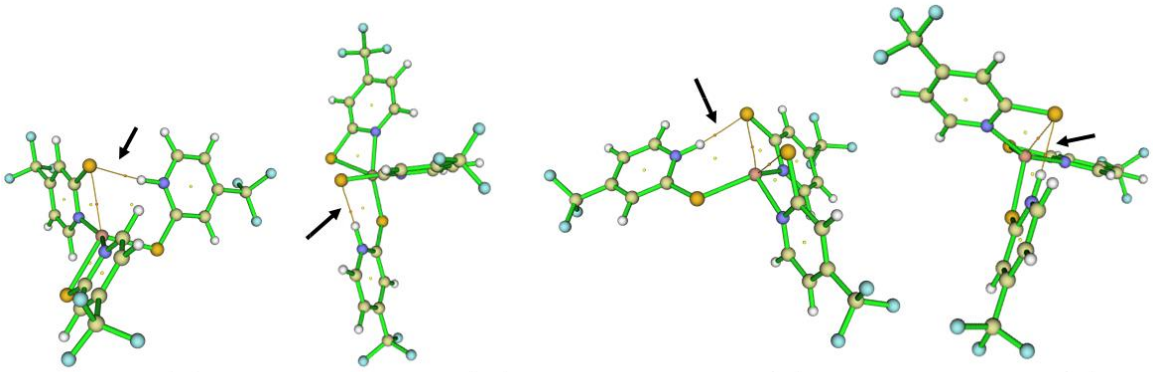

Appendix Figure 17. Topology maps of the computationally modeled reduced intermediates (1-H^-) for **$[Ni(L9)_3]H^-$** represented using ball-stick drawing method. Blue, White, Light Yellow, Dark Yellow, Pink, and cyan balls represent N, H, C, S, Ni, and F atoms, respectively. Yellow lines are the bond paths. Black arrows point toward the intramolecular hydrogen bonding interaction stabilizing the structure.

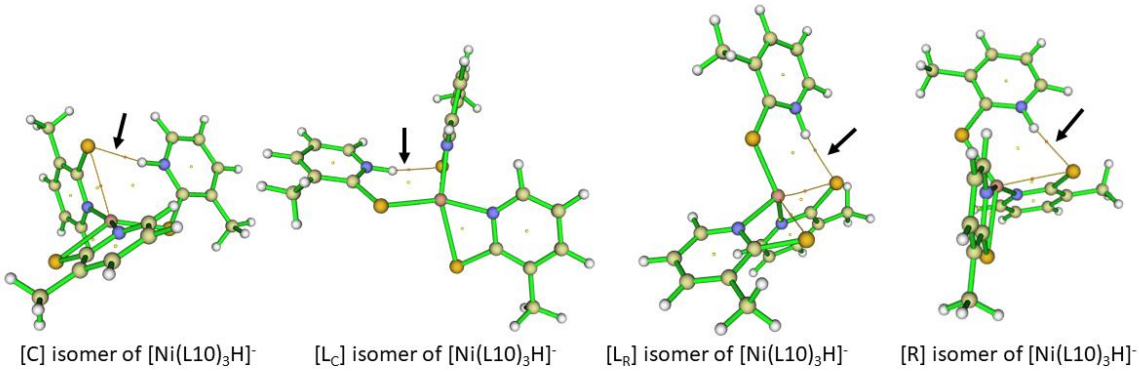

Appendix Figure 18. Topology maps of the computationally modeled reduced intermediates (1-H^-) for **$[Ni(L10)_3]H^-$** represented using ball-stick drawing method. Blue, White, Light Yellow, Dark Yellow, and Pink balls represent N, H, C, S, and Ni atoms, respectively. Yellow lines are the bond paths. Black arrows point toward the intramolecular hydrogen bonding interaction stabilizing the structure.

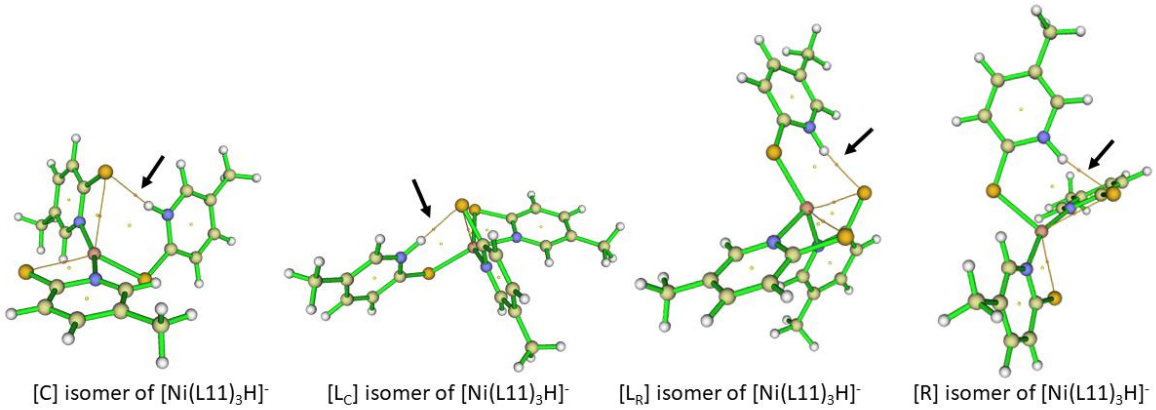

Appendix Figure 19. Topology maps of the computationally modeled reduced intermediates (1-H^-) for **$[Ni(L11)_3]H^-$** represented using ball-stick drawing method. Blue, White, Light Yellow, Dark Yellow, and Pink balls represent N, H, C, S, and Ni atoms, respectively. Yellow lines are the bond paths. Black arrows point toward the intramolecular hydrogen bonding interaction stabilizing the structure.

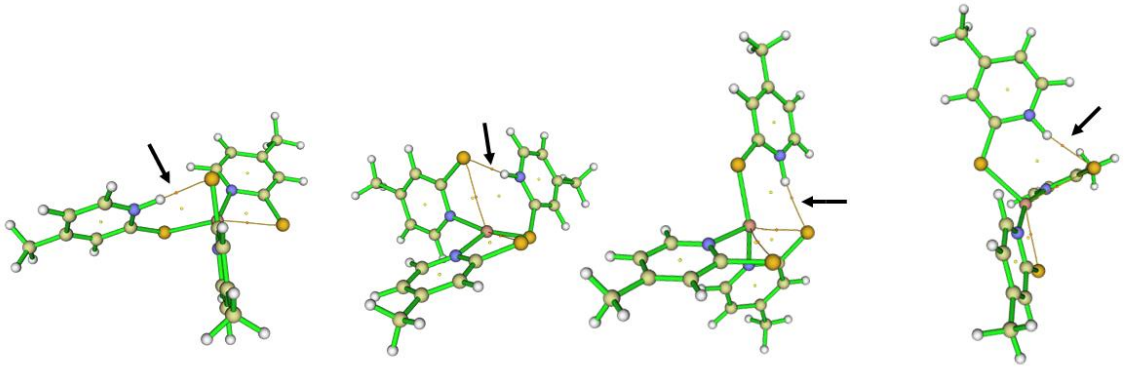

Appendix Figure 20. Topology maps of the computationally modeled reduced intermediates (1-H^-) for **$[Ni(L12)_3]H^-$** represented using ball-stick drawing method. Blue, White, Light Yellow, Dark Yellow, and Pink balls represent N, H, C, S, and Ni atoms, respectively. Yellow lines are the bond paths. Black arrows point toward the intramolecular hydrogen bonding interaction stabilizing the structure.

Appendix Table 5. Relative population of the protonated **NiDHW$_2$** complexes calculated based on the most stable **[R]** isomer when protonation of both W and D ligands are considered.

Protonated isomer	Identity of protonated ligands	Boltzmann Population (*% x*)
[CRC]	W	0.6
[LRC]	W	0.2
[R]	D	99.2

Appendix Table 6. Relative population of the protonated **NiD$_2$HW** complexes calculated based on the most stable **[CRL]** isomer when protonation of both W and D ligands are considered.

Protonated isomer	Identity of protonated ligands	Boltzmann Population (*% x*)
[CRC]	D	23.3
[LRC]	D	76.5
[RRL]	W	0.2

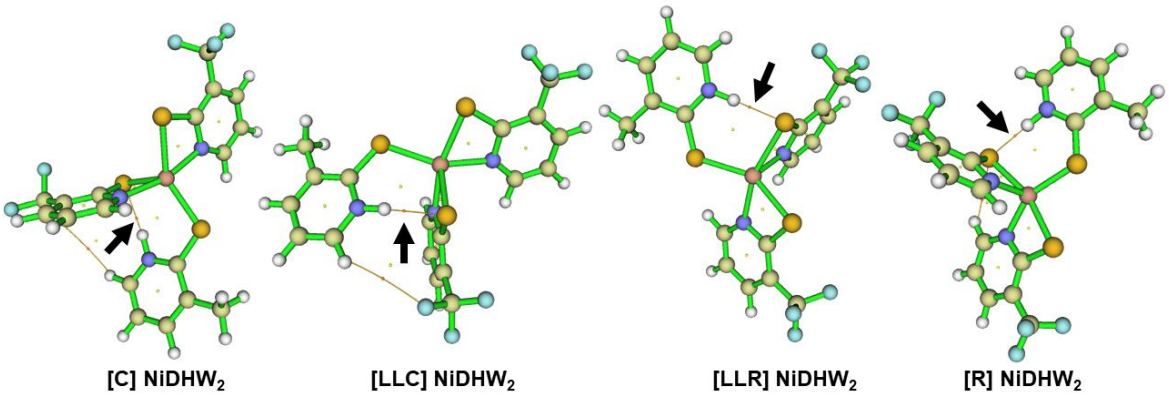

Appendix Figure 21. Topology maps of the isomers of protonated **NiDHW$_2$** complexes. The orange, blue, white, yellow, pink, and cyan balls represent S, N, H, C, Ni, and F atoms, respectively. The intramolecular H-bonds between the protonated pyridyl N atoms and the adjacent thiopyridyl S atoms (N-H…S) are marked with black arrows.

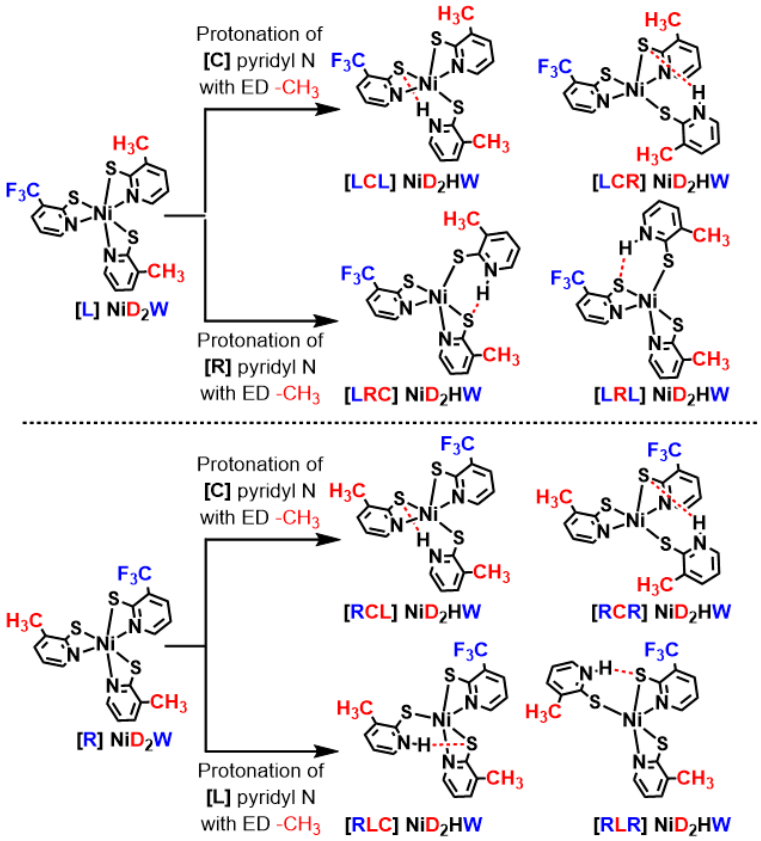

Appendix Figure 22. Protonation of D ligands of **[L]**, and **[R]** isomers of the **NiD₂W** starting catalysts to generate eight possible protonated isomers. The intramolecular H-bonding interactions between pyridyl N-H and one of the adjacent thiopyridyl S atoms are shown using red dashed bonds.

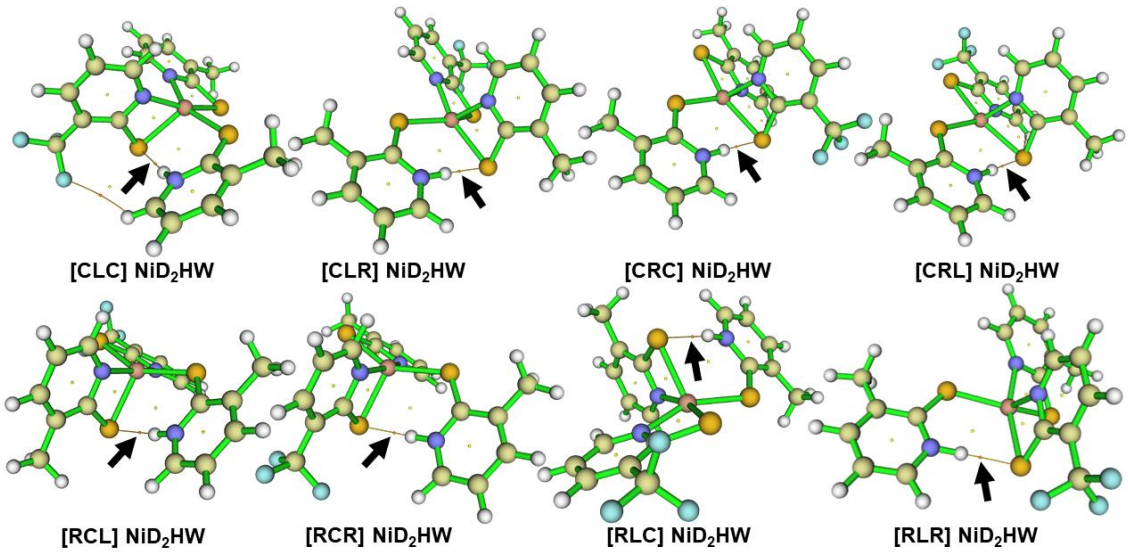

Appendix Figure 23. Topology maps of the isomers of protonated **NiD2HW** complexes. The orange, blue, white, yellow, pink, and cyan balls represent S, N, H, C, Ni, and F atoms, respectively. The intramolecular H-bonds between the protonated pyridyl N atoms and the adjacent thiopyridyl S atoms (N-H…S) are marked with black arrows.

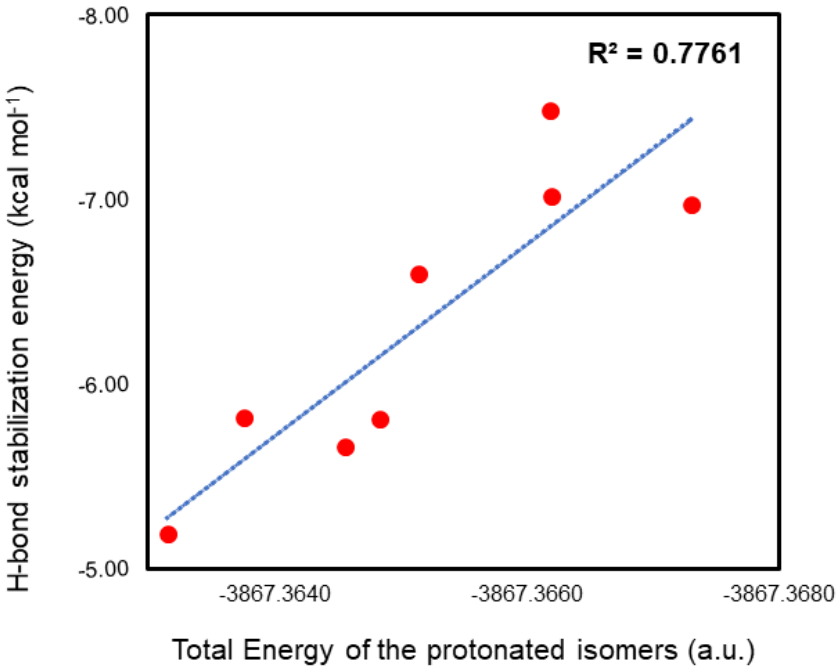

Appendix Figure 24. Graph depicting the correlation between the total energy (in a.u.) of the protonated isomers of **NiD_2HW** heteroleptic complexes and the intramolecular H-bond strength (kcal mol^{-1}) of the N-H...S interactions observed in the corresponding isomers.

Appendix Table 7. Calculated pK_a values of all possible isomers of the protonated heteroleptic **$NiDW_2$** and **NiD_2W** complexes in polarized continuum water solvation model at 298 K.

Protonated complex	Isomer	Calculated pK_a values in water
$NiDHW_2$	[C]	8.2
	[LLC]	8.6
	[LLR]	9.3
	[R]	9.5
	[CLC]	9.7
	[CLR]	7.1
NiD_2HW	[CRC]	10.7
	[CRL]	11.1
	[RCL]	10.1
	[RCR]	9.0
	[RLC]	9.5
	[RLR]	10.0

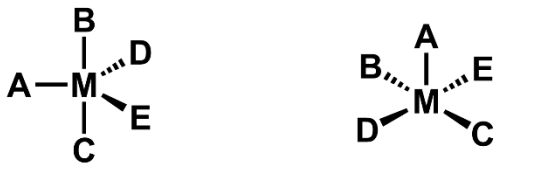

$\beta \equiv \angle BMC = 180^0$ $\alpha \equiv \angle DME = 120^0$ $\beta \equiv \angle BMC = 90^0$ $\alpha \equiv \angle DME = 90^0$

Appendix Figure 25. Structure index parameter (τ) for the penta-coordinated metal-ligand complexes: trigonal bipyramid (left), and square pyramid (right) as introduced by Addison *et* al. where τ is the ratio of the difference of the two largest basal angles (α, and β) and 60. For an ideal trigonal bipyramid τ is 1; while that for an ideal square pyramid is 0.

Appendix Table 8. Calculation of the structure index parameter (τ) for the reduced intermediates **$NiDHW_2^-$**, and **NiD_2HW^-** of heteroleptic **$NiDW_2^-$**, and **NiD_2W^-** complexes, respectively.

	β in degrees	**α in degrees**	**τ**
$NiDHW_2^-$	157.25	115.42	0.70
NiD_2HW^-	159.26	113.62	0.76